Searching for the Magnetic Interactions in the Rare Earth Pyrochlore Oxide $Yb_2Ti_2O_7$

by

Jordan Thompson

A thesis
presented to the University of Waterloo
in fulfillment of the
thesis requirement for the degree of
Master of Science
in
Physics

Waterloo, Ontario, Canada, 2011

I hereby declare that I am the sole author of this thesis. This is a true copy of the thesis, including any required final revisions, as accepted by my examiners.

I understand that my thesis may be made electronically available to the public.

Abstract

Various experiments on $Yb_2Ti_2O_7$ have shown evidence of strange magnetic behaviour at low temperatures. Specific heat measurements on powder samples of $Yb_2Ti_2O_7$ show evidence of a sharp peak, indicating the occurence of a first order phase transition. Meanwhile, neutron scattering, Mössbauer absorption, and μSR measurements find no evidence of long range order below the temperature of this phase transition, leaving the nature of the low temperature phase a mystery. Quantifying the magnetic interactions in this material should allow us to better understand the low temperature behaviour of this material. In this study, we fit a symmetry allowed nearest-neighbour bilinear exchange model to quasi-elastic neutron scattering data collected well above the temperature of the experimentally observed phase transition. This neutron scattering data shows evidence of rods of scattering intensity along the $\langle 111 \rangle$ crystallographic directions. Neutron scattering probes the correlations between magnetic moments in a material, so fitting an interaction model to the neutron scattering is equivalent to fitting the interactions to the magnetic correlations. These correlations are driven by the interactions between the magnetic moments, so the neutron scattering should give us direct access to the form of these interactions. Using this method we successfully identify an anisotropic nearest-neighbour bilinear exchange model that reproduces the experimentally observed quasi-elastic neutron scattering. With this model we then proceed to compute real space correlation functions, finding that the rods of neutron scattering arise from the presence of strong correlations along nearest-neighbour chains. We also compute the bulk susceptibility and local susceptibility, obtaining very good fits to experiment with no variation of the model determined from the neutron scattering. The success of these calculations provides a further independent confirmation of the success of our interaction model in describing the magnetic interactions in $Yb_2Ti_2O_7$. Finally, we present a brief summary of ongoing work based on our anisotropic exchange model, including mean field calculations to determine the low temperature ground state of this model and classical Monte Carlo simulations to study the phase transition present in this model. We also discuss potential further studies of this and other models.

Acknowledgements

First, I would like to acknowledge the persistence, patience, and encouragement of my supervisor, Dr. Michel Gingras. I have learned a great deal from my time studying with him, and will be forever grateful for this experience. I would also like to thank Dr. Paul McClarty for his large contributions to this work, including the development of the RPA neutron scattering code, mean field calculations of the local susceptibility, and diagonalization of crystal field parameterizations. I would also like to thank him for his many explanations of physical concepts and theoretical methods.

I would like to thank: Dr. Pawel Stasiak, for the use of his parallel tempering classical Monte Carlo code, and his assistance in understanding its use, Behnam Javanparast, for his assistance with finding the ground state of our models of $Yb_2Ti_2O_7$, Anson Wong for many useful discussions on spin-waves and the Ewald summation technique for treating the long-range magnetic dipolar interaction, and the rest of the Condensed Matter Theory group/Quantum Matters group at the University of Waterloo for many interesting and enlightening discussions and assistance with various aspects of my work.

I would like to thank Prof. Henrik Ronnow and Dr. Louis-Pierre Regnault for the experimental neutron scattering data that made most of this work possible.

Finally I would like to dedicate this work to my family, especially my parents, for their support and encouragement during my studies. I would also like to thank my sister for her assistance in editing this work.

Table of Contents

List of Tables

List of Figures

Chapter 1

Introduction - An Experimental Overview of $Yb_2Ti_2O_7$

Magnetic materials currently attract a great deal of interest in the field of condensed matter theory as they provide an excellent sand box in which to explore the physics of many bodied systems. Such many bodied systems display a wide variety of behaviours that would not be seen if the constituent elements of the system were studied in isolation. The most widely known collective magnetic phenomenon is simple ferromagnetism, where the quantum mechanical magnetic moments of the ions in a material align to produce a net magnetic moment. In the last decade considerable interest has been centred on one particular group of magnetic materials, those which display frustration of the interactions between the magnetic moments in the system. Frustrated materials are of great interest due to the new and exotic states of matter they exhibit. These exotic states, such as the spin ice state which is currently attracting a great deal of attention [1, 2, 3], are made possible by the presence of frustration.

1.1 Frustration

Frustration is defined as the inability of a system of interacting elements to simultaneously energetically minimize all of the interactions between the elements of the system. In magnetic systems, frustration can have two sources. The first is competition between different interactions present in the system and the second is the geometry of the system. In this work we will focus on the second source, so called geometric frustration.

Geometric frustration arises in magnetic systems with fixed element geometries, such as crystal lattices, where the geometry of the system prevents the simultaneous energetic minimization of all of the interactions. This can lead to the presence of a highly degenerate ground state manifold and the existence of strange magnetic phases. The classic example of geometric frustration is the case of the global Ising antiferromagnet on a triangle. The Hamiltonian of this system is given by

$$H = \mathcal{J} \sum_{\langle i,j \rangle} S_i S_j, \tag{1.1}$$

where $\mathcal{J}$ is the strength of the exchange interaction between the spins in the system, with $\mathcal{J} < 0$ being ferromagnetic exchange, and $\mathcal{J} > 0$ being antiferromagnetic exchange. S_i and S_j are Ising spins of value ± 1, at crystal lattice sites i, j, and the angle brackets in the sum indicate that only nearest-neighbour pairs of spins are to be summed over and double counting is to be avoided. It can be clearly seen that for a single pair of spins $i, j = 1, 2$ with $\mathcal{J} > 0$, the energy of the pair is minimized when $S_1 = +1$ and $S_2 = -1$. If we consider three spins $i, j = 1, 2, 3$ on a triangle, see Fig. 1.1, we can see frustration at work. If we start at site 1, setting $S_1 = +1$ (an up arrow in Fig. 1.1), then proceeding around the triangle, to satisfy the interaction between S_1 and S_2, we must impose that $S_2 = -1$ (a down arrow in Fig. 1.1). Proceeding around the triangle, to satisfy the pairwise interactions between S_2 and S_3 we must impose that $S_3 = +1$. After this we are left only with the pairwise interactions between S_3 and S_1. If we then examine S_3 and S_1, we can see that they are both $+1$, so the interaction between them is not energetically minimized. If we were to set either S_1 or S_3 to -1 in order to satisfy this interaction, one of the other two pairwise interactions would not be in its minimum energy state. This means that the system can never energetically minimize all of the pairwise interactions on the triangle, thus it is frustrated.

In this case the frustration of the interactions leads to a ground state with six-fold degeneracy, which can be seen by going through the process just described, starting at all three sites on the triangle with both up and down spins. This is an example of a degenerate manifold of ground states. If we were to extend the single triangle to a triangular lattice (Fig. 1.2(a)), or some other lattice containing the triangular motif, such as the kagome (Fig. 1.2(b)) or pyrochlore lattice (Fig. 1.2(c)), the degeneracy of the ground state grows massively.

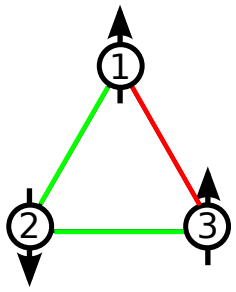

Figure 1.1: Ising spins on a triangle with antiferromagnetic interactions described by Eqn. (1.1). Green bonds are those where the pairwise antiferromagnetic interaction between nearest-neighbours are energetically satisfied, the red bond shows the presence of a pairwise interaction that is not in its energetic ground state. Up arrows are equivalent to $S_i = +1$, down arrows are equivalent to $S_i = -1$, where $i = 1, 2, 3$.

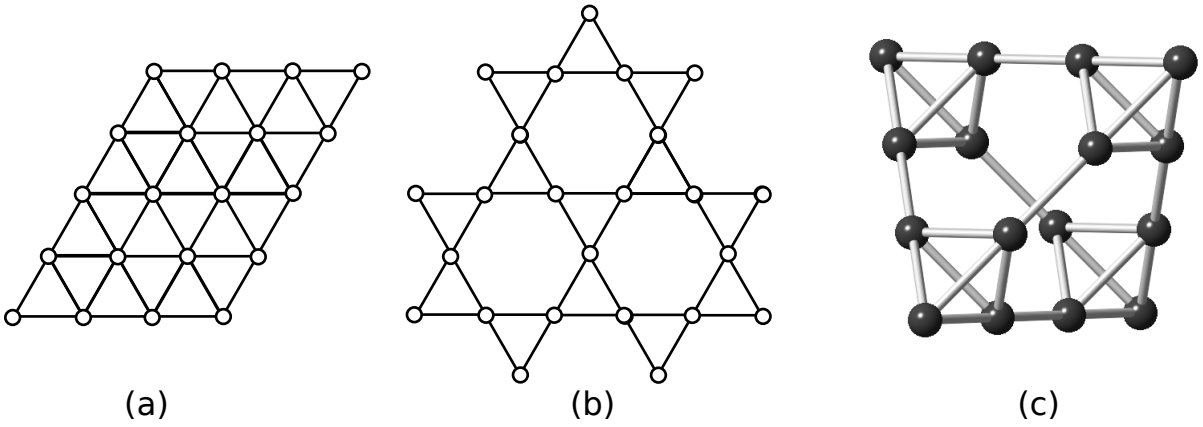

Figure 1.2: The triangular lattice (a), the kagome lattice (b), and the pyrochlore lattice (c). These are all lattices that have the capacity for geometric frustration due to the presence of the triangular motif.

1.2 The Pyrochlore Lattice

The pyrochlore lattice is a crystal lattice that lends itself to geometrical frustration of magnetic interactions because it is constructed of many triangular motifs assembled into a lattice of corner sharing tetrahedra. For example, antiferromagnetic interactions between both classical [4] and quantum [5] Heisenberg spins on the pyrochlore lattice have been shown not to order down to the lowest temperatures.

The pyrochlore lattice is a non-Bravais lattice made up of corner sharing tetrahedra, as shown in Fig. 1.2(c). It can be thought of as an FCC lattice with a four ion, tetrahedral basis at each lattice site. The vectors that describe the FCC lattice sites $\mathbf{R}_i$ are defined in Table 1.1, along with the vectors that describe the positions of the four sublattice sites with respect to the FCC lattice sites, $\mathbf{r}_a$. Using this notation, we can index any site on the pyrochlore lattice using the vector $\mathbf{R}_i^a = \mathbf{R}_i + \mathbf{r}_a$, and define the vector joining two pyrochlore lattice sites as

$$\mathbf{R}_{ij}^{ab} = \mathbf{R}_i + \mathbf{r}_a - \mathbf{R}_j - \mathbf{r}_b \tag{1.2}$$

The nearest-neighbour distance for the pyrochlore lattice is $\sqrt{2}r_c/4$, where $r_c = 10.026$ Å is the cubic unit cell dimension for $Yb_2Ti_2O_7$ [6].

Table 1.1: FCC lattice vectors and tetrahedral sublattice vectors for the pyrochlore lattice. $r_c = 10.026$ Å is the cubic unit cell dimension [6].

FCC Lattice Vectors	Tetrahedral Sublattice Vectors
$\mathbf{R}_1 = \frac{r_c}{2}(0,0,0)$	$\mathbf{r}_1 = \frac{r_c}{4}(0,0,0)$
$\mathbf{R}_2 = \frac{r_c}{2}(0,1,1)$	$\mathbf{r}_2 = \frac{r_c}{4}(0,1,1)$
$\mathbf{R}_3 = \frac{r_c}{2}(1,0,1)$	$\mathbf{r}_3 = \frac{r_c}{4}(1,0,1)$
$\mathbf{R}_4 = \frac{r_c}{2}(1,1,0)$	$\mathbf{r}_4 = \frac{r_c}{4}(1,1,0)$

The reciprocal lattice vectors $\mathbf{G}_\alpha$ for the FCC lattice are given in Table 1.2. This allows us to break any reciprocal space vector $\mathbf{Q}$ into two components $\mathbf{Q} = \mathbf{q} + \mathbf{G}$, where $\mathbf{G}$ is a linear combination of vectors $\mathbf{G}_\alpha$, and $\mathbf{q}$ is a vector inside the first Brillouin zone of the FCC lattice. The first Brillouin zone is a reciprocal space nearest-neighbour Wigner-Seitz cell constructed about the origin, or any other reciprocal lattice point. The reciprocal lattice vectors $\mathbf{G}_\alpha$ are constructed using the formula $\mathbf{G}_{k-1} = \frac{2\pi \cdot \mathbf{R}_i \times \mathbf{R}_j}{\mathbf{R}_i \cdot (\mathbf{R}_j \times \mathbf{R}_k)}$, for $i, j, k = 2, 3, 4$.

Table 1.2: FCC reciprocal lattice vectors $\mathbf{G}_\alpha$. Once again, $r_c = 10.026$ Å is the cubic unit cell dimension [6].

FCC Reciprocal Lattice Vectors
$\mathbf{G}_1 = \frac{2\pi}{r_c}(-1,1,1)$
$\mathbf{G}_2 = \frac{2\pi}{r_c}(1,-1,1)$
$\mathbf{G}_3 = \frac{2\pi}{r_c}(1,1,-1)$

1.3 Rare Earth Pyrochlores

One particular family of frustrated magnetic materials that has been the subject of a great deal of interest is the rare earth pyrochlore oxides. These are materials with the chemical formula $A_2B_2O_7$, where A is a rare earth ion (Ho,Dy,Tb,Gd, or Yb) or yttrium (Yt), and B is a tetravalent transition metal ion (Ti, Sn, Mo, or Mn). These materials are described by the $Fd\bar{3}m$ space group [7], with the A ions occupying the 16c sites, and the B ions occupying the 16d sites of this space group, forming interpenetrating pyrochlore lattices as seen in Fig. 1.3.

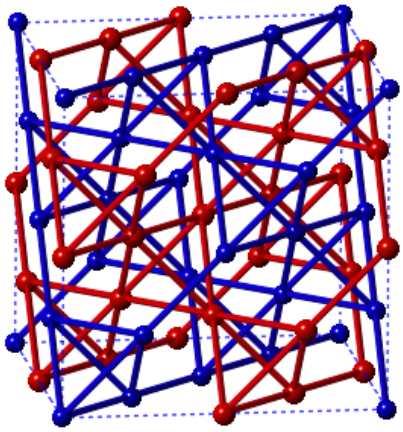

Figure 1.3: The interpenetrating pyrochlore lattices of the A ions (blue) and B ions (red) of an $A_2B_2O_7$ material [8].

Members of the rare earth pyrochlore oxide family of materials have been found to exhibit exotic phenomena at low temperature such as spin liquid behaviour in $Tb_2Ti_2O_7$ [9], and other exotic phenomena that arise due to material specific effects [10]. These include spin glass behaviour in $Y_2Mo_2O_7$ [11], spin ice in $Ho_2Ti_2O_7$, $Dy_2Ti_2O_7$, $Dy_2Ti_2O_7$,and $Ho_2Sn_2O_7$ [1, 10], and long-range order (LRO) with persistent low-temperature spin dynamics in $Gd_2Sn_2O_7$ and $Er_2Ti_2O_7$ [12, 13].

1.4 Ytterbium Titanate - $Yb_2Ti_2O_7$

Ytterbium Titanate ($Yb_2Ti_2O_7$) is another member of the rare earth pyrochlore family of materials that displays exotic behaviour at low temperatures. In this material various experimental measurements have found evidence of a magnetic phase transition at low temperatures [14, 15, 16, 17]. Interestingly, no evidence of magnetic LRO [6] has been found below this transition. We will discuss these experiment in greater detail later in this study, but first we must establish some of the basic properties of $Yb_2Ti_2O_7$.

In $Yb_2Ti_2O_7$ the Yb^{3+} ions are the only magnetic ions, and as previously discussed, they reside on a pyrochlore lattice of corner sharing tetrahedra. The electronic configuration of the Yb^{3+} ions in this material is $4f^{13}$, ${}^2F_{7/2}$. This state has a high contribution from orbital angular momentum, so the good quantum number is $J = 7/2$. The paramagnetic moment of the Yb^{3+} ions is then given by $\mu = g_J\sqrt{J\left(J+1\right)}\mu_B \approx 4.54\mu_B$. This is consistent with experiments which find that the effective magnetic moment of the Yb^{3+} ions in $\sim 4\mu_B$ at room temperatures, decreasing to $\sim 3\mu_B$ at liquid helium temperatures [18]. The ground state of the crystal field (CEF) of $Yb_2Ti_2O_7$ is a Kramers doublet [14]. This doublet structure is imposed by the fact that the Yb^{3+} ion has an odd number of electrons in the valence shell. The findings of various experimental studies on the CEF of $Yb_2Ti_2O_7$ are that the ground state Kramers doublet of the Yb^{3+} ions is locally planar [19, 20], meaning that the magnetic moments prefer to lie in planes perpendicular to the local [111] directions (defined in Table 1.3) at each corner of the tetrahedral sublattice, as shown in Fig. 1.4. If we treat the ground state doublet as an effective spin-1/2 state, this planar nature of the ground state doublet can be described by a $\mathbf{g}$ tensor, with two components $g_\parallel$ and $g_\perp$ that describe the preference of the effective spin to lie along the local z axis ($g_\parallel$), or in the local $x-y$ plane ($g_\perp$). The $\mathbf{g}$ tensor and other properties of the CEF experienced by these ions are discussed in Appendix A.

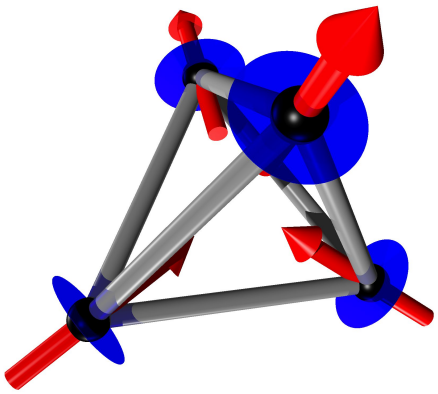

Figure 1.4: The local Ising axes (red) and easy planes (blue) of the four tetrahedral sublattice sites of the pyrochlore lattice [21].

Table 1.3: Local coordinates for the four sublattice sites of the pyrochlore lattice.

Sublattice	$a = 1$	$a = 2$	$a = 3$	$a = 4$
$\hat{\mathbf{x}}^a$	$\frac{1}{\sqrt{6}}(-1,-1,2)$	$\frac{1}{\sqrt{6}}(1,1,2)$	$\frac{1}{\sqrt{6}}(1,-1,-2)$	$\frac{1}{\sqrt{6}}(-1,1,-2)$
$\hat{\mathbf{y}}^a$	$\frac{1}{\sqrt{2}}(1,-1,0)$	$\frac{1}{\sqrt{2}}(-1,1,0)$	$\frac{1}{\sqrt{2}}(-1,-1,0)$	$\frac{1}{\sqrt{2}}(1,1,0)$
$\hat{\mathbf{z}}^a$	$\frac{1}{\sqrt{3}}(1,1,1)$	$\frac{1}{\sqrt{3}}(-1,-1,1)$	$\frac{1}{\sqrt{3}}(-1,1,-1)$	$\frac{1}{\sqrt{3}}(1,-1,-1)$

1.5 Previous Work on $Yb_2Ti_2O_7$

The first published experiments on $Yb_2Ti_2O_7$ were magnetic susceptibility measurements collected between $T = 2$ K and $T = 1400$ K on a powdered sample of $Yb_2Ti_2O_7$, published in 1968 by Townsend *et al.* [22]. These measurements were used to attempt a parameterization of the CEF experienced by the Yb^{3+} ion. This work admitted that the parameterization produced from the analysis of these measurements should be treated with caution. Recent (at the time) measurements on powdered samples of the material ytterbium gallium garnet showed similar results in terms of the crystal field structure to that of $Yb_2Ti_2O_7$ determined in this work, and the ytterbium gallium garnet results were contradicted by spectroscopic measurements on said material [22].

The next published measurements of interest to this work were specific heat measurements performed by Bløte *et al.* in 1969 [16], these measurements are shown in Fig. 1.5(a). The most interesting feature of these measurements is the peak in the specific heat at $T \sim 214$ mK [16], indicating the presence of a first order phase transition. In addition to specific heat (C_v) measurements, Ref. [16] also contains measurements of the bulk susceptibility χ as shown in Fig. 1.5(b). From these measurements the Curie-Weiss temperature $\theta_{\rm CW}$ is determined to be $\theta_{\rm CW} = 0.4 \pm 0.1$ K. $\theta_{\rm CW}$ is defined as the temperature axis intercept of a linear fit to the inverse susceptibility and is an indication of strength and type of magnetic interactions in a material. A positive $\theta_{\rm CW}$ indicates that the magnetic interactions in a material are mainly ferromagnetic. From C_v, values of the magnetic energy gain $|\Delta E/R|$, and the Heisenberg exchange energy $|J/k|$ were computed, obtaining values of $|\Delta E/R| = 1.8$ K and $|J/k| = 1.3 \pm 0.1$ K. It is noted that these are much larger than the transition temperature. J/k can also be computed from the susceptibility data, yielding $J/k = 0.13$ K. The fact that this is so different from the value extracted from C_v is taken as evidence that the exchange interaction in this material may be highly anisotropic. A constraint on the $\mathbf{g}$ tensor is also provided, $g_\parallel^2 + 2g_\perp^2 = 17$ [16]. The contradictions between the observed temperature of the phase transition and estimated values of the exchange energy and magnetic energy provide the first hint that something interesting may be going on in this material beyond a simple first order phase transition to a state with long-range order (LRO), and serve as the starting point for this work.

After these measurements, ^{170}Yb Mössbauer absorption measurements were performed by Dunlap *et al.* in 1978 [23], in an effort to better understand the CEF experienced by the Yb^{3+} ions in $Yb_2Ti_2O_7$. The analysis of these measurements concluded that the CEF states of the Yb^{3+} ion consist of two low energy doublets, separated by a gap of $\Delta E \sim 20$ K, with higher energy states lying at $\Delta E \sim 130$ K, and $\Delta E \sim 750$ K [23]. This analysis used four parameters to describe the the CEF experienced by the Yb^{3+} ions, B_2^0,B_4^0,B_6^0,

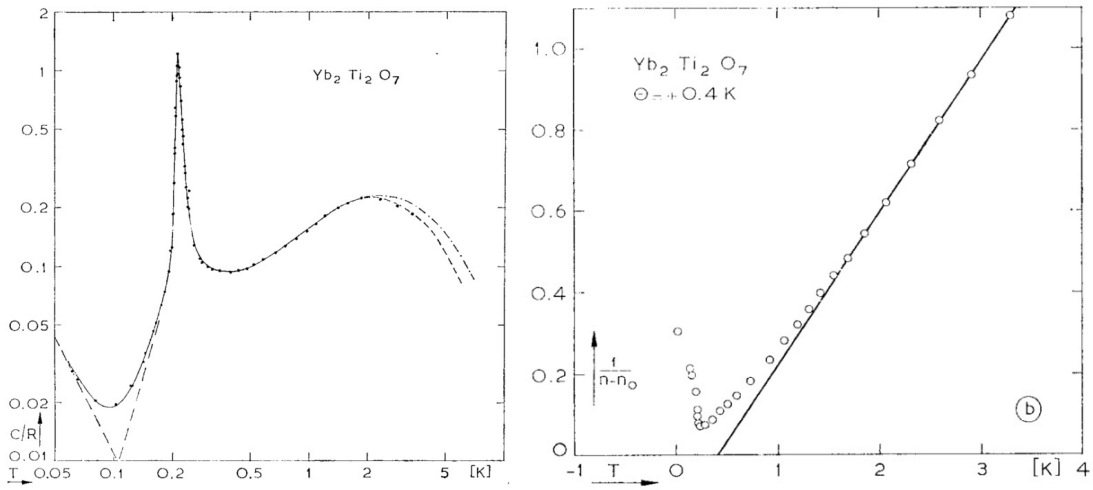

Figure 1.5: Figures reproduced from Ref. [16]. (a) is a plot of the specific heat (C/R), and (b) is a plot of the inverse susceptibility ($1/\chi$) of $Yb_2Ti_2O_7$ in arbitrary units. The dashed line in (a) on the right side below 0.2 K represents the hyperfine splitting contribution to C_v and the remaining heat capacity after the removal of the hyperfine splitting contribution. On the left side of the graph the dashed line represents an extrapolation of the behaviour, as does the dash-dotted line. The two extrapolations correspond to different values of the entropy, with integration along the dashed line yielding $S = 0.671R$, and integration along the dash-dotted line yielding $S = R \ln 2$. The solid line in (b) represents the high temperature fit between $T = 2$ K and $T = 3.5$ K, used to determine $\theta_{\rm CW} = 0.4 \pm 0.1$ K.

and B_6^6, which are used to define a linear combination of Stevens-operator equivalents [24] to describe the crystal field [23]. The work of Sengupta, published in 1999 [25], explains that four Stevens-operator equivalents are insufficient to describe the CEF of $Yb_2Ti_2O_7$, given the D_{3d} symmetry of the oxygen ions surrounding the Yb^{3+} ion [25]. Ref. [25] goes on to explain that a CEF parameterization based on six Stevens-operator equivalents is required, and attempts to extract the coefficients of these terms, A_2^0, A_4^0, A_4^3, A_6^0, A_6^3, and A_6^6, from the magnetic susceptibility data of Ref. [22], and the Mössbauer absorption data of Ref. [23]. The conclusions of these works with respect to the form of the CEF in $Yb_2Ti_2O_7$ have subsequently been shown to be incorrect by more recent work [19, 20, 26], which will be discussed later.

The next work on $Yb_2Ti_2O_7$, is that of Siddharthan *et al.*, also published in 1999 [27],

who performed magnetic susceptibility and specific heat measurements on $Yb_2Ti_2O_7$ and other rare earth pyrochlores. They then used Monte Carlo simulations based on an Ising model with super-exchange and long-range magnetic dipolar interactions to attempt to explain the observed behaviours of the specific heat of $Yb_2Ti_2O_7$. This was done despite citing evidence from CEF calculations [28] that the ground state doublet of the Yb^{3+} CEF should be local XY planar in nature, not local Ising-like [27]. For the case of $Yb_2Ti_2O_7$, they assume only long-range dipolar interactions are at play, and obtain reasonable agreement with experiment on the position of the peak in the specific heat [27]. Their final comment on $Yb_2Ti_2O_7$ is that further calculations are in progress, but if they were ever published, we have not been able to locate them.

After the work by Siddharthan [27], Bramwell *et al.* [18] published in 2000 measurements of the magnetic susceptibility and bulk magnetization, M, of several rare earth pyrochlores including $Yb_2Ti_2O_7$. From these measurements, they computed various quantities, including the free ion moment at various temperatures, and $\theta_{CW} = 0.7$ K. An attempt was made to fit the observed field dependence of the magnetization at various temperatures to a model of an effective spin-1/2 doublet with an effective g value (the diagonal elements of the **g** tensor are assumed to be identical). Performing this fit is shown to result in a different value of g at each temperature, with an optimal value over all the temperatures of $g = 7.2$ [18]. This variation of g with temperature is taken to indicate a failure in the model and as an indication that $g_\perp$ may be significantly different from $g_\parallel$ in this material.

The next set of publications on $Yb_2Ti_2O_7$ were research by Hodges *et al.*, Refs. [14, 15, 20]. These works present a very comprehensive set of measurements on $Yb_2Ti_2O_7$, including ^{170}Yb mössbauer absorption, magnetic susceptibility, magnetization, ^{172}Yb perturbed angular correlation (PAC), and neutron scattering measurements.

The first work, Ref. [20] published in 2001, presents ^{170}Yb Mössbauer absorption, ^{172}Yb perturbed angular correlation (PAC) measurements, magnetic susceptibility, and specific heat measurements performed on polycrystalline samples of $(Y_{0.99}Yb_{0.01})Ti_2O_7$ and $Yb_2Ti_2O_7$ in an effort to quantify the CEF structure and magnetic interaction strength in $Yb_2Ti_2O_7$. The first measurements presented in this work are ^{170}Yb Mössbauer absorption measurements on $(Y_{0.99}Yb_{0.01})Ti_2O_7$, which are used to determine the **g** tensor for isolated Yb^{3+} moments, finding $g_\parallel = 1.79$, $g_\perp = 4.27$. The next experiments presented are bulk DC susceptibility and magnetization measurements in $Yb_2Ti_2O_7$. The susceptibility was measured from $T = 2.5$ K to $T = 10$ K, finding $\theta_{CW} = 0.75$ K, indicating that the interactions between the Yb^{3+} moments are ferromagnetic in nature. Fits to the magnetization at several temperatures, using the previously determined planar **g** tensor, show that adding ferromagnetic interactions between the Yb^{3+} moments fits the data quite well. This provides further evidence for net ferromagnetic interactions in this material. A

suggestion that these interactions should be anisotropic in nature is made, but introducing this anisotropy does not improve the fit, so the authors abandon the idea. The interaction term used to perform these fits is expressed as $\vec{H} \rightarrow \vec{H} + \lambda\vec{\mu}$, with $\lambda = 0.31(4)$ T/μ_B, so that it encompasses both exchange and long-range dipolar interactions. In addition to measurements on polycrystalline samples, magnetization measurements on a single crystal of $Yb_2Ti_2O_7$ are discussed, with the conclusion that they do not yield any new information. Finally ^{172}Yb PAC measurements are reported. These measurements are used to quantify the thermal dependence of the quadrupole hyperfine interaction of the ^{172}Yb nucleus, which was found by the Mössbauer absorption measurements to be quite small. In addition, the PAC measurements are fitted using six free parameters, B_2^0, B_4^0, B_4^3, B_6^0, B_6^3, and B_6^6, corresponding to the inclusion of six different Stevens-operator equivalent in the CEF parameterization, as required by the D_{3d} symmetry of the Yb^{3+} ion site. Starting from an unpublished set of CEF parameters in Ref. [29], the authors obtain a good fit to the PAC measurements, obtaining a CEF parameterization that is discussed in detail in Appendix A. This CEF parameterization yields $g_{\parallel} = 1.77$, $g_{\perp} = 4.18$ for the ground state doublet, with a gap between the ground state and first excited state of $\Delta E = 620$ K. The authors conclude by stating that previously published CEF parameterizations [22, 23, 25] are not compatible with the experimental observations presented in this work and this is the reason we do not consider the work of Refs. [22, 23, 25] any further in this study.

The second work in this set of publications, Ref. [14] also published in 2001, presents ^{170}Yb Mössbauer absorption and ^{172}Yb PAC measurements. Mössbauer absorption spectroscopy data for both $(Y_{0.99}Yb_{0.01})Ti_2O_7$ and $Yb_2Ti_2O_7$ is presented, with the work on $(Y_{0.99}Yb_{0.01})Ti_2O_7$ being the same as that in Ref. [20]. The Mössbauer absorption spectra for $Yb_2Ti_2O_7$ are new to this work, previous works reported only Mössbauer absorption spectra for $(Y_{0.99}Yb_{0.01})Ti_2O_7$, with absorption spectra for polycrystalline samples of $Yb_2Ti_2O_7$ at various temperatures from $T = 4.2$ K down to $T = 0.036$ K being reported, as shown in Fig. 1.6. A marked change in the Mössbauer absorption spectra is reported at $T \sim 0.3$ K. Above this temperature, the spectrum is characterized by a single narrow line, whose width increases as the temperature decreases, while below $T \sim 0.26$ K a five line hyperfine-field sub-spectrum appears, completely replacing the single line spectrum by $T \sim 0.2$ K. The broadening of the single line spectrum for $T > 0.3$ K is attributed to fluctuations of the Yb^{3+} moments and the fluctuation rate is extracted from the width of these lines. The five line spectrum observed for $T < 0.2$ K is indicative of a hyperfine-field that is static on the time scale of Mössbauer spectroscopy so the fluctuation rate of the Yb^{3+} moments cannot be measured below this temperature. The strength of the hyperfine-field leading to this five line spectrum is extracted, yielding a Yb^{3+} moment size in the low temperature phase of $1.15\mu_B$. The temperature dependence of the size of the

moment is determined, finding that the moment goes from zero to $\sim 1.15\mu_B$ very sharply at $T = 0.26$ K, consistent with the observed peak in the specific heat in Ref. [16]. Finally, using the size of the ground state moment and the **g** tensor determined in Ref. [20] the direction of the moment with respect to the local [111] z axis is determined via the equation $M = 0.5\left[g_{\parallel}^2 \cos^2\alpha + 2g_{\perp}\sin^2\alpha\right]^{1/2}$, where α, the angle between the moment and the local z axis, is found to be $22^\circ \pm 3^\circ$.

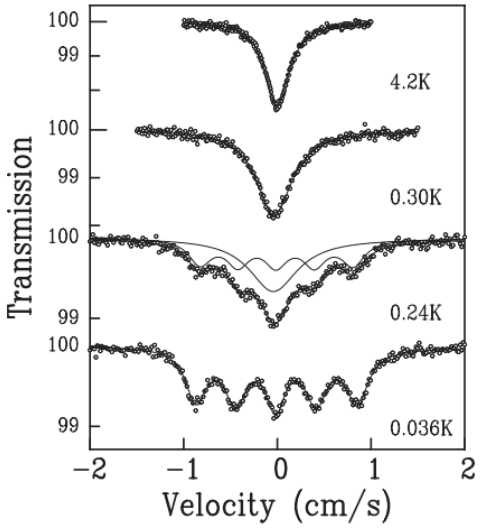

Figure 1.6: Figure reproduced from Ref. [14]. The Mössbauer absorption spectra of $Yb_2Ti_2O_7$ at various temperatures. The solid lines show the combination of single line and five line spectra that make up the data at $T = 0.30$ K.

The third work of this set, Ref. [15] published in 2002, presents the previously discussed ^{170}Yb Mössbauer absorption, along with new neutron scattering, and muon spin resonance (μSR) measurements, in an effort to better understand the nature of the phase transition and low temperature phase of $Yb_2Ti_2O_7$. The neutron scattering measurements presented were performed on a powder sample of $Yb_2Ti_2O_7$. Neutron scattering measures the correlation between magnetic moments in materials, as such it is admirably suited to detecting the presence of magnetic correlations or LRO in materials. If magnetic LRO exists in a material, it is typically evidenced by magnetic Bragg peaks in the elastic neutron scattering cross section, the component of the neutron scattering cross section where the energy of the neutrons is conserved. These peaks are either superimposed on nuclear Bragg peaks, which arise from the nuclear magnetic moments in the material, or at new positions in

reciprocal space. The nuclear Bragg peaks are indicative of the crystalline order of the material. Analysis of the positions of these magnetic Bragg peaks can reveal the type of magnetic order that is present in the material. The neutron scattering measurements of Ref. [15] reveal that the crystal structure of $Yb_2Ti_2O_7$ does not change with temperature, and that no magnetic Bragg peaks are found to appear below $T = 0.2$ K, indicating that no magnetic LRO is present in the low temperature phase. This means that the static hyperfine field observed by Mössbauer absorption in Ref. [14] is not due to LRO, but to slowing of the fluctuation rate of the Yb^{3+} moments to level a below that detectable via Mössbauer absorption. In addition to this neutron scattering data, μSR measurements are presented and used to determine the fluctuation rate of the Yb^{3+} moments below $T = 0.2$ K in the range where Mössbauer absorption is incapable of distinguishing the fluctuation rate. These μSR measurements find a non-zero, temperature independent Yb^{3+} moment fluctuation rate of ~ 1000 MHz, as shown in Fig. 1.7. This temperature independent fluctuation rate below $T = 0.24$ K is a further indication that something very strange is going on in the low temperature phase of $Yb_2Ti_2O_7$. Ref. [17] published in 2006 contains additional work on μSR data in various magnetic fields at $T \approx 0.07$ K. This work was done to determine if the persistent spin dynamics observed in Ref. [15] were due to a large density of states at low energies. The work finds that a gaussian-broadened gaussian (GBG) model, rather than the traditional Kubo-Toyabe model associated with an ensemble of slowly fluctuating moments, fits the experimental data quite well below the temperature of the peak in the specific heat reported in Ref. [16]. The GBG model assumes that each muon sees a different environment, described by a dynamic Kubo-Toyabe function, and that fields in these environments are characterized by a gaussian distribution. The most interesting finding of this work is that the GBG model only works if a magnetic field strength less than that of the actual applied field is used in the model, but no interpretation of this effect is provided.

In 2003 Bonville *et al.* published a review article, Ref. [30], discussing experiments on both $Yb_2Ti_2O_7$ and $Gd_2Ti_2O_7$. This work provides an excellent summary and discussion of the results of most of the previous work on $Yb_2Ti_2O_7$. This review does contain some new work, such as zero-field and field-cooled measurements of the bulk DC susceptibility, showing irreversibilities similar to those shown in glassy materials [30], and neutron scattering measurements on a single crystal of $Yb_2Ti_2O_7$, which find no evidence of Bragg peaks down the lowest temperatures measured ($T = 0.04$ K). The neutron scattering measurements include quasi-elastic neutron scattering data in the paramagnetic phase of $Yb_2Ti_2O_7$ ($T > 0.3$ K). Quasi-elastic neutron scattering is neutron scattering where the difference in energy of the of the incident and scattered neutrons is very small. This quantity is what is detected in many elastic scattering experiments due to the finite energy resolution of

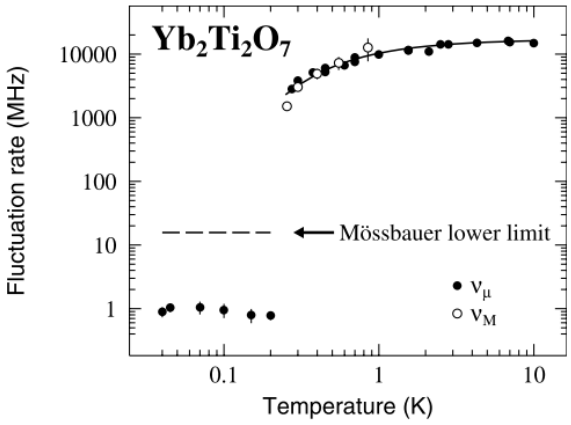

Figure 1.7: Figure reproduced from Ref. [15]. The fluctuation rate of the Yb^{3+} moment determined from Mössbauer absorption, $\nu_{\rm M}$, and from μSR, ν_μ. A sudden change is seen to take place at $T \sim 0.24$ K, consistent with the peak in the specific heat observed in Ref. [16]. Below $T \sim 0.24$ K, the fluctuation rate falls below the minimum value detectable by Mössbauer absorption, indicated by the dashed line.

the detectors. The single crystal paramagnetic neutron scattering presented in this work is the same data, but at much lower resolution, that is presented in our published work, Ref. [31], and which forms a key part of this study. The most interesting feature of this neutron scattering data, shown in Fig. 1.10, is the [111] rod of scattering intensity, seen to develop at $T = 25$ K, which increases in intensity as T decreases, as seen in Fig. 1.11. The rod-like feature is taken as evidence of bi-dimensional real space correlations between Yb^{3+} moments, an idea that will be tested in this study. Reference [32] is essentially the same document, but with significantly less neutron scattering data being presented. This data is discussed further in the next section.

Also in 2003, Yasui *et al.* published neutron scattering, magnetization, and susceptibility measurements on a single crystal of $Yb_2Ti_2O_7$ in Ref. [33]. This somewhat controversial work claims to detect ferromagnetic order in the low temperature phase of $Yb_2Ti_2O_7$ via the existence of magnetic Bragg peaks in low temperature neutron scattering data. Bulk DC susceptibility measurements presented in this work yield $\theta_{\rm CW} = 0.59$ K, and the real part of the AC susceptibility shows an anomaly at $T = 0.24$ K that, along with magnetization measurements, is taken as evidence for a ferromagnetic phase transition at $T = 0.24$ K. The magnetization is also used to determine the strength of the inter-ionic exchange in $Yb_2Ti_2O_7$ in combination with the values of $g_\parallel$ and $g_\perp$ for the ground state doublet

of the CEF. A value for the interaction term λ is found, $\lambda = 0.64 \pm 0.1\ \mu_B$/T, which is approximately double the value found in Ref. [20], and the components of the $\mathbf{g}$ tensor are found to be $g_{\parallel} = 2.6 \pm 0.4$ and $g_{\perp} = 3.9 \pm 0.2$. This is a much less anisotropic form of the $\mathbf{g}$ tensor than was found in Ref. [20]. The neutron scattering measurements below $T = 0.03$ K show no Bragg peaks other than nuclear Bragg peaks, but analysis of the temperature dependence of the intensity of these peaks reveals magnetic intensity at several of the nuclear Bragg peaks. The distribution of the magnetic intensity at the nuclear Bragg peaks is consistent with $\mathbf{q} = 0$ ferromagnetic order. It is interesting to note that the peaks were detected after letting the sample equilibrate at $T = 0.03$ K for 10h, a very long time scale seemingly not taken into account in other experiments involving the low temperature phase of $Yb_2Ti_2O_7$. This long time scale of the magnetic neutron scattering intensity leads to hysteresis in the magnetic scattering intensities on cooling and warming. Finally, typical time scales for changes of the neutron scattering intensity are reported for two temperatures, $T = 0.03$ K and $T = 1$ K, where time scales of 120 min and 30 min are found respectively. This is interpreted as evidence that the motion of the Yb^{3+} moments slows as temperature decreases [33]. No information on how these time scales were determined in given.

The work of Gardner *et al.*, Ref. [6] published in 2004, presents neutron spin echo (NSE) and polarized neutron scattering measurements designed to refute the findings of Ref. [33]. NSE measures $S(\mathbf{Q}, t)$, which contains information about the temporal and spatial correlations between magnetic moments. The presented NSE measurements reveal that $S(\mathbf{Q})$ increases with decreasing $|\mathbf{Q}|$, consistent with ferromagnetic interactions, as found in Ref. [20]. The presented NSE measurements also reveal signal relaxation times of less than 4 ps at both $T = 180$ mK and $T = 1$ K, inconsistent with the presence of ferromagnetic LRO in the low temperature phase. Polarization analysis of the neutron beam is also inconsistent with ferromagnetic LRO in the low temperature phase, as no loss of polarization is found, which would occur in the case of a polycrystalline ferromagnet. Polarized neutron scattering does find evidence of a magnetic contribution to the Bragg scattering at $\mathbf{q} = (1, 1, 1)$ at $T = 90$ mK, consistent with Ref. [33], but not at any other Bragg peaks. In order to explain all of these findings, two scenarios are proposed: that the system consists of small domains of ordered (but not ferromagnetically ordered) moments surrounded by fluctuating moments, or that the observed magnetic contribution to the Bragg scattering is due to nuclear ordering, and not electronic moment ordering[1].

[1] Important: When taken in combination, the results of Ref. [6] and Ref. [33] present a very muddy picture of whether there in fact exists any magnetic LRO in the low temperature phase of $Yb_2Ti_2O_7$. Ref. [33] appears to present clear evidence of ferromagnetic LRO in the low temperature phase of $Yb_2Ti_2O_7$. Ref. [6] on the other hand reports quite clear evidence, in the form of neutron spin echo (NSE) and

In 2004, Malkin *et al.* published an article on $Yb_2Ti_2O_7$ reporting the use of optical spectroscopy to determine the CEF energy levels of $Yb_2Ti_2O_7$, Ref. [26]. This study was inspired by marked differences between the CEF structure of $Yb_2Ti_2O_7$ found in Ref. [20], and the structure that would be expected based on those of other rare earth pyrochlore materials. These differences cannot be explained on the basis of the effect of changes in lattice parameters between compounds on the positions of the other ions in the material surrounding the rare earth ions. IR absorption spectroscopy was performed on $Yb_2Ti_2O_7$ and IR fluorescence spectroscopy was performed on $Y_2Ti_2O_7$(1% Yb). Beginning from a CEF parameterization of $Ho_2Ti_2O_7$, a set of CEF parameters, B_2^0, B_4^0, B_4^3, B_6^0, B_6^3, and B_6^6, that respect the D_{3d} symmetry of the Yb^{3+} site are refined to fit the fluorescence spectroscopy data. The ground state doublet of the refined CEF parameterization is described by $g_\parallel = 1.836$ and $g_\perp = 4.282$, similar to the **g** tensor parameters found in Ref. [20], but the parameters B_2^0, B_4^0, B_4^3, B_6^0, B_6^3, and B_6^6 are quite different from those found in Ref. [20]. The differences between the CEF parameterization of this work and that of Ref. [20] provide the impetus for the second CEF parameterization of $Yb_2Ti_2O_7$ used in this study. This second CEF parameterization, discussed in Appendix A is refined from ^{170}Yb PAC measurements and the CEF parameterization of $Ho_2Ti_2O_7$ in Ref. [34].

The next set of publications on $Yb_2Ti_2O_7$ are a pair of publications on local susceptibility (χ_a) measurements by Cao *et al.*, Refs. [19, 34]. χ_a is defined as the coupling between a single magnetic moment at a sublattice site a and the external field **H**, by the equation $\mathbf{M}_a = \overline{\chi}_a \mathbf{H}$, where $a = 1, 2, 3, 4$ is the tetrahedral sublattice label. It is extracted from polarized neutron scattering measurements via the method of Ref. [35], and is explained further in Chapter 6.1.

The first work of Cao *et al.*, Ref. [19] published in 2009, reports χ_a measurements on several rare earth pyrochlore oxide materials including $Yb_2Ti_2O_7$. The reported measurements of χ_a for $Yb_2Ti_2O_7$ are shown in Fig. 1.8. This work presents a new CEF parameterization for $Yb_2Ti_2O_7$ that respects the D_{3d} symmetry of the Yb^{3+} lattice site. This parameterization is similar to that of Ref. [26], and is determined in a similar manner, starting from a CEF parameterization of $Ho_2Ti_2O_7$ and adjusting the CEF parameters for that material to fit PAC measurements reported in Ref. [20]. The details of this CEF parameterization are discussed in detail in Appendix A. The ground state doublet of this CEF parametrization is described by a **g** tensor that is planar in nature, as found in other CEF

beam polarization measurements, that no ferromagnetic LRO is present in the low temperature phase of $Yb_2Ti_2O_7$. While Ref. [6] does not appear to collect data on the same time scales as Ref. [33], and does find some evidence of magnetic ordering of an unknown type, we consider the NSE and beam polarization results of Ref. [6] to be a sufficient contradiction of the results of Ref. [33] to conclude that no clear experimental evidence of magnetic LRO in the low temperature of $Yb_2Ti_2O_7$ has been found.

parameterizations [20], with $g_{\|} = 2.24$ and $g_{\|} = 3.98$. If this CEF parameterization is used to compute the local susceptibility via mean field theory, it can be seen in Fig. 1.8 that the fit fails at low temperatures. The authors attempt to eliminate this disagreement between experiment by adding a term to the magnetic field, similar to the method of Refs. [20, 33], but incorporating anisotropic exchange, to yield $\mathbf{H}_i^{\text{eff}} = \mathbf{H} + \overleftrightarrow{\lambda} \cdot \mathbf{m}_i$, where $\mathbf{H}$ is the applied magnetic field, $\mathbf{m}_i$ is the magnetic moment at lattice site i, and $\overleftrightarrow{\lambda}$ is a 3×3 tensor which describes the exchange field at that lattice site. In the local sublattice coordinate system, $\overleftrightarrow{\lambda}$ has two components $\lambda_{\|}$ and $\lambda_{\perp}$. It is found that $\lambda_{\|} = 2.5$ T/μ_{B} and $\lambda_{\perp} = -0.05$ T/μ_{B} yields a good fit to the experimental data, as seen in Fig. 1.8. This is claimed by the authors to be the first concrete evidence of anisotropic exchange interactions in $Yb_2Ti_2O_7$. However, it is important to note that this model of the interactions does not properly take into account the tetrahedral sublattice structure of the pyrochlore lattice. This sublattice structure is very important to the physics of this material, due to the different CEF easy planes at each corner of the tetrahedral sublattice, so any model that does not include this structure does not correctly describe $Yb_2Ti_2O_7$.

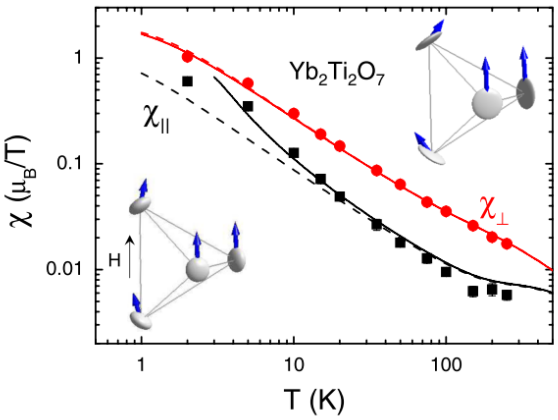

Figure 1.8: Figure reproduced from Ref. [19]. The measured values of the two independent components of χ_a for $Yb_2Ti_2O_7$, $\chi_{\perp}$ and $\chi_{\|}$ (symbols), along with fits to $\chi_{\perp}$ and $\chi_{\|}$ based on models including only the CEF parameterization presented in Ref. [19] (dashed lines), and a form of anisotropic exchange presented in Ref. [19] (solid lines). The insets are magnetization ellipsoids, whose shape is determined by the form of χ_a, at 5 K (bottom) and 250 K (top). The arrows represent the field induced moment directions.

The second work of Cao *et al.*, Ref. [34] also published in 2009, concentrates on $Yb_2Ti_2O_7$, and reports the χ_a measurements of Ref. [19] along with measurements of the DC bulk

susceptibility of powder samples of $Yb_2Ti_2O_7$. The main component of this work is the computation of the powder susceptibility from the anisotropic exchange model proposed in Ref. [19]. They find that this model fits the experimental data better than either ferromagnetic or antiferromagnetic Heisenberg exchange, but they restrict themselves to Heisenberg models of unit strength (i.e. $\lambda_\parallel = \lambda_\perp = \pm 1$ T$/\mu_B$) making the failure of these models somewhat artificial, as the strength of the exchange is not allowed to vary to fit the data. Based on the fact that the local Ising term of the anisotropic exchange model they utilize ($\lambda_\parallel$) is so much larger that the local planar term ($\lambda_\perp$), they propose that $Yb_2Ti_2O_7$ may be something called an 'exchange spin ice'. Such a material would be one where the interactions lead to local Ising behaviour, rather than the CEF leading to this behaviour as occurs in canonical spin ice materials [36]. It is argued that, given the magnitude of the magnetic moments in the low temperature phase of $Yb_2Ti_2O_7$ found in other works [20], the different anisotropy of the ground state $\mathbf{g}$ tensor found in Ref. [19] allows for the Yb^{3+} moments to lie along the $\langle 111 \rangle$ axis at each corner of a tetrahedron, as occurs in the spin ice materials. Finally, a discussion of the implications of this model for the low temperature spin dynamics of $Yb_2Ti_2O_7$ is presented. It is argued that the large easy plane terms of the $\mathbf{g}$ tensor will allow rapid fluctuations between spin up and spin down local Ising states that cannot occur in conventional spin ices, perhaps explaining the low temperature fluctuations observed in μSR experiments [15]. As we discussed earlier, the exchange model of this work is based on does not respect the sublattice structure of the pyrochlore lattice, so any discussion relying on the importance of the Ising component of the anisotropic exchange model they present should be considered suspect because it does not account for the presence of multiple sublattices in the pyrochlore lattice.

The work of Malkin *et al.*, Ref. [37] published in 2010, takes the local susceptibility measurements of Ref. [19] for several of the rare earth pyrochlore oxide materials, and performs an improved fit to the data based on an anisotropic exchange model that does account for the sublattice structure of the pyrochlore lattice. The form of the anisotropic exchange used in this model is also constructed to obey the symmetry of the space group $Fd\bar{3}m$, which describes the pyrochlore lattice. This symmetry consideration is incomplete though, as the authors impose an artificial symmetry on two of the four symmetry allowed bilinear exchange terms. They also fail to include a fourth symmetry allowed interaction all together. In order to understand this imposed symmetry, and why it is artificial, we observe that Ref. [37] defines three different exchange couplings $\lambda_{\perp,1}$, $\lambda_{\perp,2}$, and $\lambda_\parallel$. If we relate these to the symmetry allowed nearest-neighbour bilinear exchange interactions on

the pyrochlore lattice defined in Appendix C we find that (Eqns. A.1-A.3 in Ref. [38])

$$\lambda_{\perp,1} = \frac{1}{3}\mathcal{J}_{\text{Ising}} + \mathcal{J}_{\text{iso}} + \mathcal{J}_{\text{pd}}, \tag{1.3}$$

$$\lambda_{\perp,2} = \mathcal{J}_{\text{iso}} + \frac{1}{2}\mathcal{J}_{\text{pd}}, \tag{1.4}$$

$$\lambda_{\parallel} = -\frac{2}{3}\mathcal{J}_{\text{Ising}} + \mathcal{J}_{\text{iso}} - 2\mathcal{J}_{\text{pd}}, \tag{1.5}$$

where $\mathcal{J}_{\text{Ising}}$, $\mathcal{J}_{\text{iso}}$, and $\mathcal{J}_{\text{pd}}$ are the strengths of three different symmetry allowed exchange terms defined in Appendix C. Reference [37] imposes the constraint $\lambda_{\perp,1} = \lambda_{\perp,2}$, which artificially breaks the symmetry of the pyrochlore lattice and reduces the number of free coupling variables by one. For the case of $Yb_2Ti_2O_7$, the authors state that they have determined exchange couplings that are much larger than those reported for the other rare earth pyrochlore oxides, but they do not report the actual values of these couplings.

Finally we come to specific heat measurements on powder and single crystal samples of $Yb_2Ti_2O_7$ presented in the Ph.D. thesis of J. Quilliam, Ref. [39] published in 2010, and reproduced in Fig. 1.9. The most interesting feature of this data is that instead of the sharp peak in C_v observed in both sets of powder data, the C_v measurements on a single crystal of $Yb_2Ti_2O_7$ show a broad peak around $T = 180$ mK. The single crystal used in these measurements is part of the same crystal used to perform neutron scattering measurements by Ross *et al.* in Ref. [40]. These measurements find a change in the form of the diffuse neutron scattering, from rods indicative of 2-dimension correlations, to 3-dimension correlations, but not long-range order, at a temperature consistent with the feature observed in the single crystal specific heat data. The powder sample specific heat reported in this work was measured using the powdered $Yb_2Ti_2O_7$ used to produce the single crystal, and shows a sharp peak at $T = 270$ mK. This marked difference between the powder and single crystal measurements is quite interesting, and in combination with the variations in the temperature at which the phase transition occurs between different samples of $Yb_2Ti_2O_7$ [16, 33] perhaps indicates issues with the quality of $Yb_2Ti_2O_7$ powder and single crystal samples.

1.6 Paramagnetic Neutron Scattering

We now come to the experiments of greatest interest to this study, quasi-elastic neutron scattering measurements performed on single crystals of $Yb_2Ti_2O_7$ at temperatures above that of the phase transition observed in the specific heat.

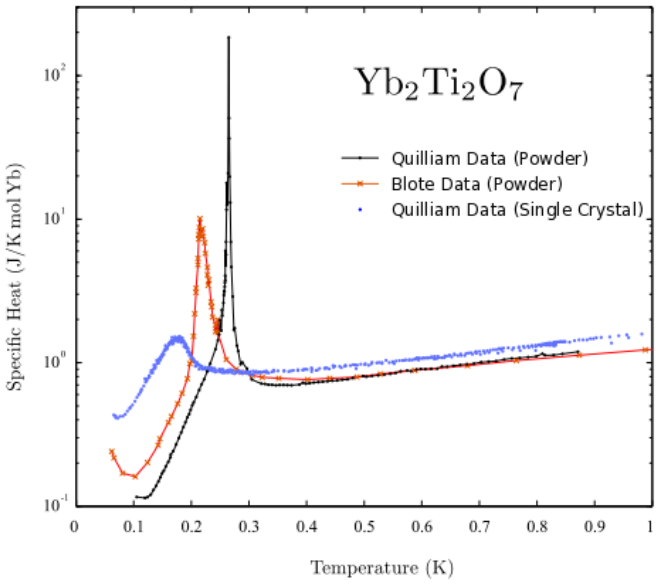

Figure 1.9: Figure reproduced from Ref. [39]. Specific heat measurements performed on powder and single crystal samples of $Yb_2Ti_2O_7$. The specific heat measurements of Ref. [16], shown in Fig. 1.5, are also included for comparison. The figure has been modified to clarify the labels of the various measurements presented.

As briefly discussed earlier on pg. 13, neutron scattering measures correlations between magnetic moments. More specifically, it measures the correlations between the components of magnetic moments perpendicular to the scattering wave-vector $\mathbf{Q}$. Neutron scattering experiments are performed by placing a material sample into a beam of neutrons, either from a nuclear reactor, or from a spallation source. These neutrons posses magnetic moments (spins), μ_n, that interact with the magnetic fields in the sample and are scattered. These scattered neutrons are then detected in ways that allow the momentum and energy of the scattered neutrons to be determined, such as triple axis diffractometers as in Ref. [31] or time-of-flight detectors as in Ref. [40].

The neutron scattering experiments considered in this work are quasi-elastic neutron scattering, neutron scattering with very small but not completely zero energy transfer from the neutron to the sample. The quantity measured in experiment is the differential neutron scattering cross section $\frac{d^2\sigma}{d\Omega dE}$. In terms of experiment, this quantity is the number of neutrons counted over a solid angle range $d\Omega$ and energy range dE, divided by the

incident neutron flux, or [41]

$$\left(\frac{d^2\sigma}{d\Omega dE}\right) = \frac{\delta N}{|\mathbf{j}\left(\mathbf{k},\mathbf{s}_n\right)|d\Omega dE} W_{\mathbf{k}\mathbf{s}_n,\mathbf{k}'\mathbf{s}'_n}. \tag{1.6}$$

δN is the number of neutrons incident on a detector in the ranges $d\Omega$ and dE, $\mathbf{j}\left(\mathbf{k}\mathbf{s}_n\right)$ is the incident flux of neutrons with energy $\hbar\mathbf{k}$ and spin $\mathbf{s}_n$, and $W_{\mathbf{k}\mathbf{s}_n,\mathbf{k}'\mathbf{s}'_n}$ is the probability of the neutron undergoing a transition from the state $|\mathbf{k}\mathbf{s}_n\rangle$ to the state $|\mathbf{k}'\mathbf{s}'_n\rangle$, which describe the incident and scattered spin and momentum states of the neutrons respectively. The microscopic physics behind this formulation of the neutron scattering cross section will be covered in the next chapter.

Quasi-elastic neutron scattering measurements performed on single crystals of $Yb_2Ti_2O_7$ were first presented in Ref. [30], as discussed in in the previous section. These measurements were performed on a single crystal sample at the Institute Laue Langevin (ILL), in Grenoble, France. These measurements reveal a very interesting feature; a rod of scattering in the (h,k,k) plane along the [111] direction. This rod is found to develop at $T \approx 25$ K, and increases in intensity as the temperature decreases, even though its width does not change significantly [30]. It is also stated that the intensity of the rods peaks at $T = 2-3$ K, the same temperature as a broad feature in the specific heat observed in Ref. [16]. The scattering in the (h,k,k) plane reported in Ref. [30] is shown in Fig. 1.10. The temperature dependence of the intensity of the rods is reported in Ref. [30] for two points in $\mathbf{Q}$ space, $\mathbf{Q} = (1.5, 1.5, 1.5)$ and $\mathbf{Q} = (1.9, 1.9, 1.9)$, and these results are shown in Fig. 1.11.

The next reported set of neutron scattering measurements on the paramagnetic phase of $Yb_2Ti_2O_7$ is the work of Ross *et al.*, Ref. [40] published in 2009. In this work, many different neutron scattering measurements are reported, not only quasi-elastic neutron scattering, but also inelastic neutron scattering for temperatures from 4 K, all the way down to 30 mK. These measurements were performed both in zero magnetic field, and in an external magnetic field applied along the [110] direction. These measurements were performed using the disk chopper spectrometer at the NIST Center for Neutron Research on a single crystal of $Yb_2Ti_2O_7$ grown at McMaster University [40]. The first measurements reported in Ref. [40] are zero field measurements of the quasi-elastic neutron scattering in the (h,h,l) plane (symmetry equivalent to (h,k,k)). These measurements are shown in Fig. 1.13, along with one set of data collected in a magnetic field. It can be seen that for the zero field data, as the temperature decreases from 4 K to 200 mK, rod-like features develop in the neutron scattering. These rods increase in intensity with decreasing temperature, but, as the temperature decreases to 30 mK in zero field, the rods begin to break up, bunching up around the nuclear Bragg peaks, as seen in Fig. 1.13. Rod-like features in neutron scattering

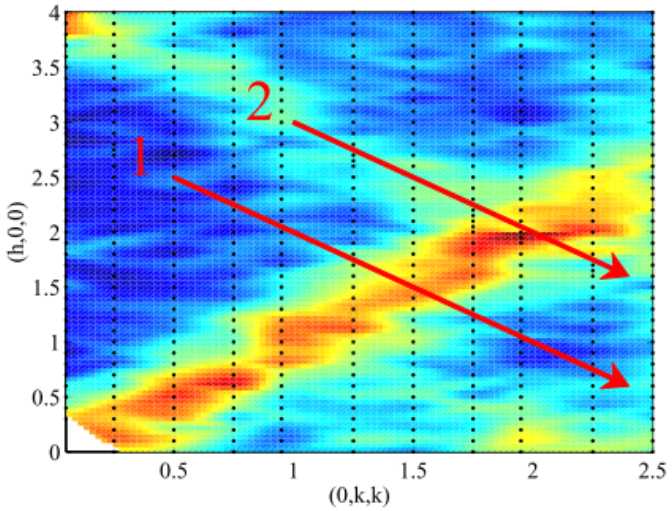

Figure 1.10: Figure reproduced from Ref. [30]. Quasi-elastic neutron scattering in the (h, k, k) plane at $T = 1.4$ K. The most interesting feature of this data is the [111] rod of neutron scattering intensity. The red lines are the directions along which **Q** scans were performed to determine the temperature dependence of the results.

typically indicate the presence of the two dimensional correlations in planes perpendicular to the direction of the rods of scattering. In the case of the pyrochlore lattice, the planes perpendicular to [111] are alternating triangular and kagome planes, as shown in Fig. 1.12. Broad peaks in the scattering on the other hand indicate three dimensional correlations. The observed bunching up of the intensity is taken as an indication of a crossover from two dimensional correlations to three dimensional correlations. The transition is not one to LRO, as this would cause the formation of magnetic Bragg peaks and not the broad features seen in the data. Fig. 1.13 also shows data taken at 30 mK in a 2 T field. This data shows distinct Bragg peaks and no rod-like features whatsoever, indicating that the field has induced the system in a magnetically well-ordered state.

In addition to quasi-elastic neutron scattering, Ref. [40] reports inelastic neutron scattering along the $[hhh]$ direction in reciprocal space, shown in Fig. 1.14. This data confirms the existence of magnetic LRO in the low temperature ($T = 30$ mK), high field region of the phase diagram of $Yb_2Ti_2O_7$, through the existence of sharp dispersive spin wave excitations that develop at a field of 0.5 T. The lack of these excitations in the low temperature phase in zero magnetic field is consistent with a lack of magnetic LRO in this phase.

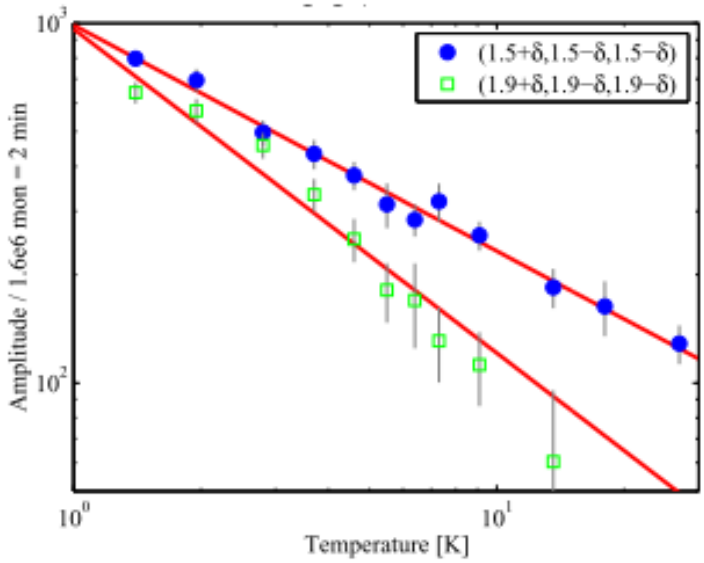

Figure 1.11: Figure reproduced from Ref. [30]. The temperature dependence of the rods of neutron scattering at selected points in $\mathbf{Q}$ space, $\mathbf{Q} = (1.5, 1.5, 1.5)$ and $\mathbf{Q} = (1.9, 1.9, 1.9)$.

Ref. [40] also presents a phase diagram for $Yb_2Ti_2O_7$ based on neutron scattering and magnetization measurements consisting of three distinct phases, the high temperature, small field paramagnetic phase (including the region where rods of scattering appear), the low temperature, small field $3D$ correlated phase, and the high field ordered phase. A statement is made that the high field ordered phase and the low field paramagnetic phase are distinct phases, and that the high field ordered phase is not simply a field polarized paramagnet, based on a minimum that appears in the magnetization as a function of the field strength. Finally, Ref. [40] makes a comment on the scattering intensity of the Bragg peaks as a function of magnetic field. The intensities of some of the peaks, particularly $(2, 2, 2)$, are found to decrease as the magnetic field is ramped up to values below that of the zero field intensity. This seems to suggest some kind of field driven structural phase transition.

Finally we come to the neutron scattering measurements used in this work. These measurements were collected on the D23 diffractometer at the ILL in Grenoble, France by Henrik Rønnow and Louis-Pierre Regnault on a single crystal of $Yb_2Ti_2O_7$. This data is a more detailed version of the neutron scattering data reported in Ref. [30], and has been

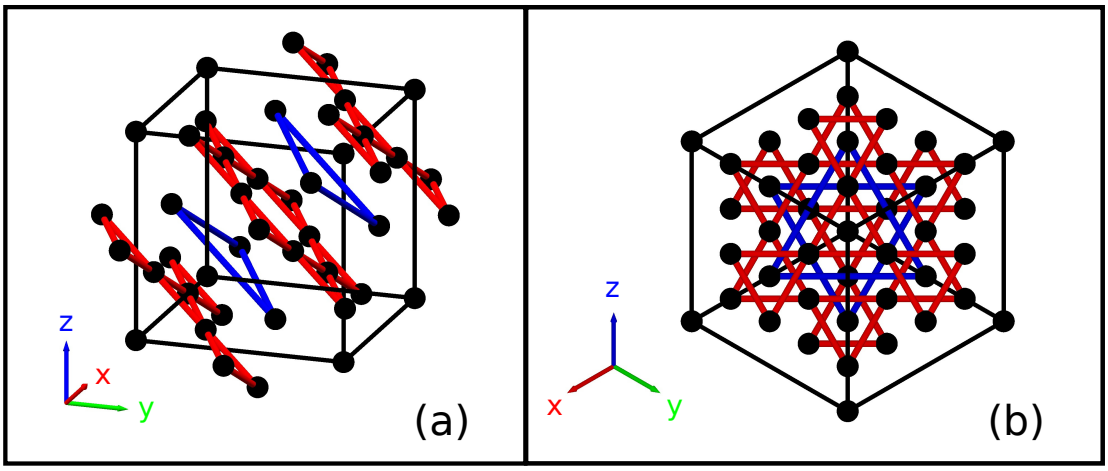

Figure 1.12: (a) The cubic unit cell of the pyrochlore lattice showing the alternating kagome (red) and triangular (blue) planes perpendicular to the [111] cubic body diagonal direction. (b) A view of the same lattice along the [111] direction [21].

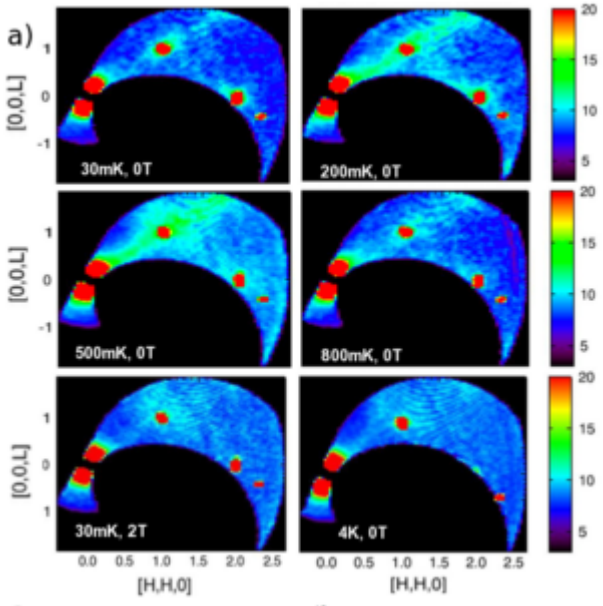

Figure 1.13: Figure reproduced from Ref. [40]. Diffuse quasi-elastic neutron scattering intensity in the (h, h, l) plane. Bright red dots indicate nuclear Bragg peaks.

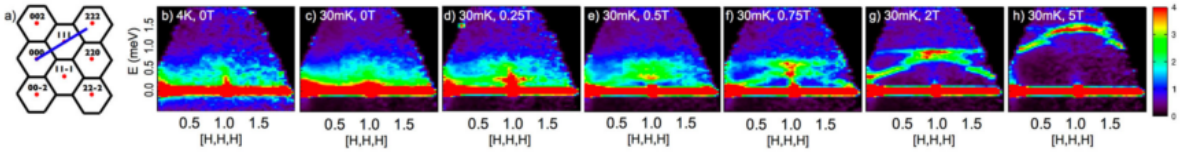

Figure 1.14: Figure reproduced from Ref. [40]. Inelastic neutron scattering along the $[hhh]$ direction in reciprocal space, for various strengths of the magnetic field along $[1\bar{1}0]$. Panel a shows how the (h, h, l) planes is tiled by first Brillouin zones, while Panels b-h show the inelastic neutron scattering. Panels b and c show the scattering in zero field for $T = 4$ K and $T = 30$ mK, while panels d-h show the scattering for $T = 30$ mK for various field strengths. It can be seen that for field strengths of greater than 0.5 T, sharp spin waves appear, clear evidence of magnetic LRO.

reported in Ref. [31], the contents of which makes up part of this study. Two sets of data are presented in Ref. [31], data at $T = 1.4$ K, and data at $T = 9.1$ K, shown in Fig. 1.15. As can be clearly seen in panels (a) and (b) of Fig. 1.15, a rod of scattering is present in the data, as was found in Refs. [30, 40] though it is quite weak at $T = 9.1$ K. Fig. 1.15(c) shows a cut through the (h, k, k) plane along $[h, 2.25, 2.25]$ for both $T = 1.4$ K and $T = 9.1$ K. This cut shows that the intensity of the scattering feature in the top right corner of panels (a) and (b) of Fig. 1.15 is not magnetic in nature as it does not evolve with temperature.

The rods of scattering intensity that appear in the neutron scattering collected by Henrik Rønnow are directly related to the correlations between the magnetic moments of the Yb^{3+} ions in $Yb_2Ti_2O_7$, as discussed in Ref. [40]. These correlations are connected to the magnetic interactions present in this material. These relationships should make it possible to determine the form of the magnetic interactions present in $Yb_2Ti_2O_7$ from the quasi-elastic neutron scattering of Fig. 1.15, specifically the data collected at $T = 1.4$ K. A knowledge of the magnetic interactions present in this material is the first step towards understanding the low temperature behaviour of $Yb_2Ti_2O_7$, particularly the observed zero field phase transition and low temperature phase. As we saw in the previous section, previous researchers [16, 19, 20, 33, 34, 37] have attempted to understand the interactions in this material, starting with simple Heisenberg models [16, 20, 33] and progressing to anisotropic exchange [19, 34, 37]. Each of these attempts have had shortfalls, either assuming an overly simplistic form for the exchange exchange interaction as in Refs. [16, 20, 33], or when considering the presence of anisotropic exchange interactions, failing to consider the sublattice structure or full symmetry of the the material [19, 34, 37]. The work of this study will

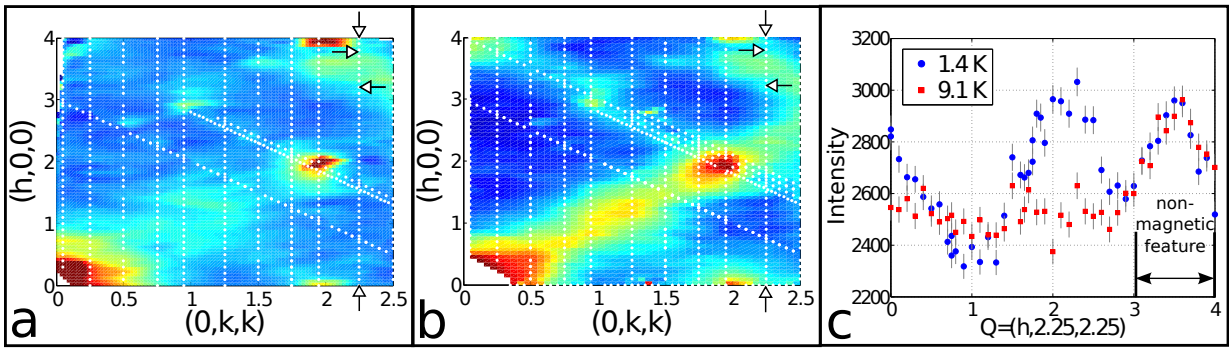

Figure 1.15: Neutron Scattering in the (h, k, k) plane of reciprocal space in zero external field at (a) $T = 1.4$ K and (b) $T = 9.1$ K. Panel (c) shows the neutron scattering along the line $[h, 2.25, 2.25]$ at $T = 1.4$ K and $T = 9.1$ K. The important feature to note is that the scattering intensity between $h = 3$ and $h = 4$, revealing that the feature in the top right corner of panels (a) and (b) near $\mathbf{q} = (3.5, 2.25, 2.25)$ is not magnetic in origin. The white arrows in (a) and (b) show the range $h \in [3, 4]$ along the direction $[h, 2.25, 2.25]$.

be to determine the form of the magnetic interactions in $Yb_2Ti_2O_7$ from the quasi-elastic neutron scattering data of Fig. 1.15. Once the form of the magnetic interactions has been determined, we will set out to determine the form of the magnetic correlations driven by these interactions that lead to the rod-like features in the neutron scattering. We will also compute other quantities that have been measured in experiment, such as the bulk and local susceptibilities. Finally we will explore the low temperature behaviour of the system described by our model Hamiltonian.

Chapter 2

The Model Hamiltonian for $Yb_2Ti_2O_7$

The first step in determining the form of the magnetic interactions in $Yb_2Ti_2O_7$ is to define a model magnetic Hamiltonian for this material. This Hamiltonian, H, will describe the local crystal field environment inhabited by the Yb^{3+} ions in $Yb_2Ti_2O_7$ and the exchange and long-range magnetic dipolar interactions between the magnetic moments of the Yb^{3+} ions. We define this Hamiltonian as

$$H = H_{\text{int}} + H_{\text{CF}}, \tag{2.1}$$

where H_{CF} describes the crystal field environment that the Yb^{3+} ions inhabit, and H_{int} describes all of the interactions between the moments of the Yb^{3+} ions.

2.1 The Crystal Field of $Yb_2Ti_2O_7$

Yb^{3+} ions have a $4f^{13}$, $^2F_{7/2}$ electronic configuration. As there are an odd number of electrons in the valence shell, Yb^{3+} is a Kramers ion, and thus the crystal field must have an even number of states. The crystal field of $Yb_2Ti_2O_7$ splits the $^2F_{7/2}$ energy level into four Kramers doublets [20]. As discussed in the previous chapter, the crystal field of $Yb_2Ti_2O_7$ has been probed experimentally by various groups as far back as 1968 [22]. The early studies of this material [22, 23] failed to use the correct crystal field parameters required by symmetry in their descriptions of the crystal field. The site symmetry of the pyrochlore lattice site that the Yb^{3+} ions inhabit is D_{3d} [20]. For this type of symmetry, the crystal field must be described by six independent crystal field parameters, so that H_{CF} can be written as:

$$H_{\text{CF}} = B_2^0 O_2^0 + B_4^0 O_4^0 + B_4^3 O_4^3 + B_6^0 O_6^0 + B_6^3 O_6^3 + B_6^6 O_6^6, \tag{2.2}$$

where O_n^m are Steven's operators, which are defined in Appendix B. The oldest work on the crystal field of $Yb_2Ti_2O_7$, Ref. [22] considered only three of the six symmetry required terms (B_2^0,B_4^0, and B_6^0), while the next work, Ref. [23], considered only two of the symmetry allowed terms (B_2^0 and B_4^0). Reference [25] considered all independent crystal field terms, and based on magnetic susceptibility measurements and Mössbauer spectra, proposed a set set of crystal field levels where the ground state is purely $|J_x = \pm 3/2\rangle$, and the energy gap between the ground state and first excited state is $\Delta E \sim 138$ K. This crystal field parameterization is inconsistent with the findings of more recent experiments in Refs. [19, 20]. These two works propose similar crystal field schemes that disagree with the findings of Ref. [25].

We will use two different crystal field (CEF) parameterizations for $Yb_2Ti_2O_7$ in our attempts to extract the form of the magnetic interactions in this material, that of Hodges *et al.* [20], discussed in Appendix A.1, and that of Cao *et al.* [19], discussed in Appendix A.2. Both of these CEF parameterizations yield a set of CEF states where the ground state doublet is well separated from the excited states and has a local easy plane anisotropy.

2.2 Magnetic Interactions

To describe the magnetic interactions between the magnetic moments of the Yb^{3+} ions we propose an interaction Hamiltonian

$$H_{\text{int}} = H_{\text{ex}} + H_{\text{dip}}, \tag{2.3}$$

where H_{ex} describes all of the symmetry allowed nearest-neighbour bilinear exchange interactions for the pyrochlore lattice, and H_{dip} describes the long-range magnetic dipolar interaction. We choose to restrict the exchange interactions in this model Hamiltonian to bilinear exchange based on the fact that the energy gap between the ground state doublet and the lowest excited state doublet of the CEF, $\Delta \sim 650 \pm 40$ K, [20, 19] is much larger than the temperature at which the quasi-elastic neutron scattering data was collected, 1.4 K. Also the strength of the magnetic dipolar and exchange interactions in this material, an indication of which is given by $\theta_{\text{CW}} = 0.70 \pm 0.05$ [18, 20], is much less than that of the CEF splitting. Because both the interaction energy and temperature are much less than the CEF splitting, we can safely project the microscopic interaction Hamiltonian, H_{mic}, which may contains higher order multipolar terms because Yb^{3+} is a $J = 7/2$ ion, onto a low energy Hilbert space spanned only by the direct product of the states in the ground state doublet of the CEF [31]. This will allow us to consider only an effective Hamiltonian H_{eff} that describes bilinear exchange interaction between effective spin-1/2 doublets, where

the bilinear interactions between these spin-1/2 operators represent the "down-projection" of higher order multipolar magnetic interactions between the full **J** angular momentum operators.

2.2.1 Symmetry Allowed Bilinear Exchange Interactions

The symmetry allowed nearest-neighbour exchange interactions for the pyrochlore lattice are derived and discussed in Appendix C. There are four such interactions $\{\mathcal{X}_n\} = \mathcal{X}_1, \mathcal{X}_2, \mathcal{X}_3, \mathcal{X}_4$. $\mathcal{X}_1$ and $\mathcal{X}_2$ contain the components of the conventional $\mathbf{J}_a \cdot \mathbf{J}_b = J_a^x J_b^x + J_a^y J_b^y + J_a^z J_b^z$ Heisenberg exchange interaction, split into two terms. $\mathcal{X}_1$ contains two of the three terms that make up the Heisenberg exchange interaction, and $\mathcal{X}_2$ contains the third term. The specific bilinear exchange terms contained in $\mathcal{X}_1$ and $\mathcal{X}_2$ vary depending on the sublattices as shown in Eqns. (C.7) and (C.8). $\mathcal{X}_4$ (Eqn. (C.10)) contains all of the anti-symmetric symmetry allowed bilinear exchange terms, and $\mathcal{X}_3$ (Eqn. (C.9)) contains all of the remaining bilinear exchange terms not contained in $\mathcal{X}_1$, $\mathcal{X}_2$, and $\mathcal{X}_4$. Together these four terms span all of the possible bilinear exchange terms for a pyrochlore material. The energy associated with each of the symmetry allowed exchange interactions $\{\mathcal{J}_n\} = \{\mathcal{J}_1, \mathcal{J}_2, \mathcal{J}_3, \mathcal{J}_4\}$ will be determined by fitting to the neutron scattering data provided by Prof. Rønnow and collaborators. The method used to accomplish this will be discussed later in Chapter 4. H_{ex} is defined as

$$H_{\text{ex}} = \sum_{\langle i,a;j,b \rangle} (\mathbf{J}_i^a)^T \ \overline{\overline{\mathcal{J}}}^{a,b}(i,j)\, \mathbf{J}_j^b \tag{2.4}$$

where $\mathbf{J}_i^a$ and $\mathbf{J}_j^b$ are the classical angular momentum three-vectors at the i and j FCC lattice sites, and the a and b tetrahedral sublattice sites defined in Chapter 1.2. $\overline{\overline{\mathcal{J}^{a,b}}}(i,j) = \overline{\overline{\mathcal{J}^{a,b}}}\delta^{\text{NN}}_{i,a;j,b}$ is a 3×3 matrix that describes the interactions between $\mathbf{J}_i^a$ and $\mathbf{J}_j^b$, where $\delta^{\text{NN}}_{i,a;j,b}$ imposes that the pyrochlore lattice sites indexed by the FCC lattice labels i, j and sublattice labels a, b are nearest-neighbours. The angular momentum vectors $\mathbf{J}_i^a$ and $\mathbf{J}_j^b$ are written in cartesian coordinates. We have chosen to use the full **J** angular momentum operators so that the RPA method of calculating the neutron scattering, described in Ref. [42] and discussed in Chapter 3.3 can be utilized. This means that the values of $\{\mathcal{J}_n\}$ that are determined from fitting to experiment will be effective "unprojected" couplings, whose projection on to the ground state doublet of the CEF correctly describes the low energy physics of $Yb_2Ti_2O_7$. They are likely not microscopic couplings that correctly describe the physics of this material at energy scales on the order of the CEF splitting [31]. This makes

our model effectively an "un-projected" form of spin-1/2 Hamiltonian [31]. The relationship between our model and effective spin-1/2 models is discussed further in Appendix H.

To aid in understanding, the matrices $\overline{\overline{\mathcal{J}}}^{a,b}$ are most easily thought of as component matrices of a larger 12×12 matrix, $\overline{\overline{\mathcal{J}}}$, where a and b index the positions of the 3×3 submatrices within $\overline{\overline{\mathcal{J}}}$. That is,

$$\overline{\overline{\mathcal{J}}} = \begin{pmatrix} \overline{\overline{0}} & \overline{\overline{\mathcal{J}}}^{1,2} & \overline{\overline{\mathcal{J}}}^{1,3} & \overline{\overline{\mathcal{J}}}^{1,4} \\ \overline{\overline{\mathcal{J}}}^{2,1} & \overline{\overline{0}} & \overline{\overline{\mathcal{J}}}^{2,3} & \overline{\overline{\mathcal{J}}}^{2,4} \\ \overline{\overline{\mathcal{J}}}^{3,1} & \overline{\overline{\mathcal{J}}}^{3,2} & \overline{\overline{0}} & \overline{\overline{\mathcal{J}}}^{3,4} \\ \overline{\overline{\mathcal{J}}}^{4,1} & \overline{\overline{\mathcal{J}}}^{4,2} & \overline{\overline{\mathcal{J}}}^{4,3} & \overline{\overline{0}} \end{pmatrix}. \tag{2.5}$$

The nearest-neighbour condition on the interactions adds the constraints that the submatrices where $a = b$ must be zero. This is illustrated in Fig. 2.1, where it can be seen that for the pyrochlore lattice, there are no same-sublattice nearest-neighbours. Symmetry imposes the condition that $\overline{\overline{\mathcal{J}}}^{b,a} = \left(\overline{\overline{\mathcal{J}}}^{a,b}\right)^T$.

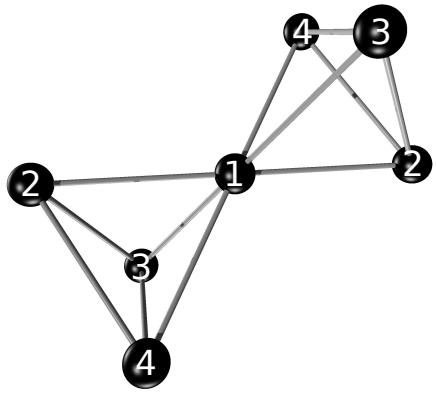

Figure 2.1: An illustration of the nearest-neighbours of sublattice site $a = 1$ of the pyrochlore lattice. Here we have chosen sublattice $a = 1$ as the origin to illustrate that none of the nearest-neighbours of this sublattice site are also $a = 1$ sites. This applies equally for all of the other sublattice sites $a = 2, 3, 4$.

For our model of symmetry allowed nearest-neighbour bilinear exchange, $\overline{\overline{\mathcal{J}}}$ consists of a linear combination of the matrix forms of the symmetry allowed nearest-neighbour

bilinear exchange interactions as defined in Eqn. (C.15)

$$\overline{\overline{\mathcal{J}}} = -\mathcal{J}_1\overline{\overline{\mathcal{X}_1}} - \mathcal{J}_2\overline{\overline{\mathcal{X}_2}} - \mathcal{J}_3\overline{\overline{\mathcal{X}_3}} - \mathcal{J}_4\overline{\overline{\mathcal{X}_4}}. \tag{2.6}$$

The chosen sign convention for the Hamiltonian means that if $\mathcal{J}_1$ and $\mathcal{J}_2$ are positive, the interaction associated with these two terms will be ferromagnetic in nature.

2.2.2 Alternative Representations of the Symmetry Allowed Bilinear Exchange Interactions

In order to perhaps ascribe a simpler and seemingly more physical meaning to the couplings $\{\mathcal{J}_n\}$, it is useful to define a more physically motivated representation of the bilinear exchange interactions. This is done by taking a linear combination of the symmetry allowed exchange terms $\mathcal{X}_n$, as explained in Appendix C.2. This allows us to write the component of the Hamiltonian containing the bilinear exchange terms, H_{ex}, as

$$H_{\text{ex}} = H_{\text{Ising}} + H_{\text{iso}} + H_{\text{pd}} + H_{\text{DM}}. \tag{2.7}$$

$$H_{\text{Ising}} = -\mathcal{J}_{\text{Ising}} \sum_{<i,a;j,b>} (\mathbf{J}_i^a \cdot \hat{\mathbf{z}}^a) \left(\mathbf{J}_j^b \cdot \hat{\mathbf{z}}^b\right) \tag{2.8}$$

is the nearest-neighbour local Ising exchange, which couples the local $\hat{z}$ components of $\mathbf{J}_i^a$ on neighbouring sublattice sites.

$$H_{\text{iso}} = -\mathcal{J}_{\text{iso}} \sum_{<i,a;j,b>} \mathbf{J}_i^a \cdot \mathbf{J}_j^b \tag{2.9}$$

is nearest-neighbour Heisenberg exchange, and

$$H_{\text{pd}} = -\mathcal{J}_{\text{pd}} \sum_{<i,a;j,b>} (\mathbf{J}_i^a \cdot \mathbf{J}_j^b - 3(\mathbf{J}_i^a \cdot \hat{\mathbf{R}}_{ij}^{ab})(\mathbf{J}_j^b \cdot \hat{\mathbf{R}}_{ij}^{ab})) \tag{2.10}$$

is the nearest-neighbour pseudo-dipolar exchange, an exchange interaction of the same form, but not related to H_{dip}.

$$H_{\text{DM}} = -\mathcal{J}_{\text{DM}} \sum_{<i,a;j,b>} \mathbf{\Omega}_{\text{DM}}^{a,b} \cdot \left(\mathbf{J}_i^a \times \mathbf{J}_j^b\right) \tag{2.11}$$

is the Dzyaloshinskii-Moriya (DM) exchange on the pyrochlore lattice (See Chapter C.2 for details). We denote the set of four exchange energies associated with this representation of the symmetry allowed bilinear exchange interactions $\{\mathcal{J}_e\} = \{\mathcal{J}_{\text{Ising}}, \mathcal{J}_{\text{iso}}, \mathcal{J}_{\text{pd}}, \mathcal{J}_{\text{DM}}\}$. This representation of the symmetry allowed bilinear exchange interactions will be used in the interpretation of the couplings $\{\mathcal{J}_n\}$ determined from fits to the experimental quasi-elastic neutron scattering in Chapter 4.

2.2.3 The Long-Range Magnetic Dipolar Interaction

The final term in H_{int} is H_{dip}, which describes the long-range magnetic dipolar interactions. H_{dip} is defined as

$$H_{\text{dip}} = D \sum_{i>j;a,b} \frac{r_{\text{nn}}^3}{|\mathbf{R}_{ij}^{ab}|^3} (\mathbf{J}_i^a \cdot \mathbf{J}_j^b - 3(\mathbf{J}_i^a \cdot \hat{\mathbf{R}}_{ij}^{ab})(\mathbf{J}_j^b \cdot \hat{\mathbf{R}}_{ij}^{ab})), \tag{2.12}$$

where $D = \frac{\mu_0 (g_J \mu_B)^2}{4\pi {r_{\text{nn}}}^3} \approx 0.01848$ K, $\mathbf{R}_{ij}^{ab}$ is defined in Eqn. (1.2), and $r_{\text{nn}} = \sqrt{2} r_c/4$, where r_c is the cubic unit cell dimension, defined in Chapter 1.2. μ_0 is the permeability of free space, μ_B is the Bohr magneton, and $g_J = 8/7$ is the Landé factor for Yb^{3+}. This term describes the interaction between the dipole moments of the Yb^{3+} ions via magnetic fields rather than exchange. Computing the sum over all of the magnetic moments $\mathbf{J}_i^a$ is done using the Ewald sum, which is discussed in detail in Appendix E.

2.3 Summary

In this chapter we have defined the magnetic Hamiltonian that we will use to describe $Yb_2Ti_2O_7$ in this study. This model consists of the local crystal field environment inhabited by the Yb^{3+} ions as well as interactions between the magnetic moments of the Yb^{3+} ions. To describe the interactions between the magnetic moments, we have proposed a combination of all of the symmetry allowed nearest-neighbour bilinear exchange interactions on the pyrochlore lattice combined with long-range magnetic dipolar interactions. This model does not specify the strengths of the various bilinear exchange terms, so a method is required to determine the strengths of the various interactions. Such a method will be discussed in Chapter 4.

Chapter 3

Magnetic Neutron Scattering

In this chapter we will explore the microscopic origins of magnetic neutron scattering in order to understand how neutrons probe the magnetic properties of a material. We will also derive the relationship between the quasi-elastic neutron scattering cross-section and the wave-vector dependent magnetic susceptibility, $\chi(\mathbf{q})$, and describe the random phase approximation method of calculating $\chi(\mathbf{q})$. These will be important tools for determining the strengths of the symmetry allowed bilinear exchange terms in our model of $Yb_2Ti_2O_7$ discussed in Chapter 2.

3.1 The Microscopic Origin of Neutron Scattering

In this section we derive the equation for the neutron scattering cross section starting from the microscopic neutron-scatterer interaction Hamiltonian. The scatterer is the material upon which the neutrons are incident, and which is responsible for the scattering of the neutrons through various interactions, hence its name. Our derivation of the microscopic origin of the neutron scattering cross section will follow that of Jensen and Mackintosh, Ref. [41]. This formulation for the scattering cross section is based on the dipole approximation. The resulting form of the neutron scattering will be used in combination with the random phase approximation discussed in the next section to compute neutron scattering from our model magnetic interactions Hamiltonian for $Yb_2Ti_2O_7$ for comparison to experiment.

In a neutron scattering experiment a beam of neutrons interacts with the material sample (the scatterer) via two mechanisms, the nuclear force, and interaction between

the neutron's magnetic moment with the magnetic field of the electrons in the sample. In materials with unpaired electrons such as $Yb_2Ti_2O_7$, these two terms yield contributions of roughly equal magnitude to the neutron scattering cross section [41]. We are not interested in the crystalline structure of $Yb_2Ti_2O_7$, so we will neglect the nuclear force as it leads only to structural Bragg peaks and does not tell us anything about the magnetic interactions in the sample. The derivation in Ref. [41] that we follow in this section considers the magnetic field from the electrons in the scatterer using a multipole expansion. The first term of this expansion, the dipolar term, provides the dominant contribution to the scattering at small scattering wave-vectors.

The neutron scattering process begins with a collimated monochromatic beam of neutrons with equal energy. We define the plane wave initial ("pre-scattering") state of the neutrons as [41]

$$|\mathbf{k}\mathbf{s}_n\rangle = V^{-1/2} \exp\left(i\mathbf{k}\cdot\mathbf{r}_n\right)|\mathbf{s}_n\rangle, \tag{3.1}$$

where $\mathbf{k}$ is the wave-vector of the neutron, $|\mathbf{s}_n\rangle$ is the spin state of the spin-1/2 neutron, and V is the volume of the system. The energy of the neutron beam is given by $\frac{\hbar\mathbf{k}^2}{2M}$ where M is the mass of the neutron. Using Fermi's golden rule, we can determine the probability that the neutron undergoes a transition from its initial state $|\mathbf{k}\mathbf{s}_n\rangle$ to the state $|\mathbf{k}'\mathbf{s}'_n\rangle$, which is given by (Eqn. 4.1.1 in Ref. [41])

$$W\left(\mathbf{k}\mathbf{s}_n, \mathbf{k}'\mathbf{s}'_n\right) = \frac{2\pi}{\hbar}\sum_{i,f} P_i|\langle\mathbf{k}\mathbf{s}_n; i|V_{\text{int}}|\mathbf{k}'\mathbf{s}'_n; f\rangle|^2\delta\left(E_{\mathbf{k}} - E_{\mathbf{k}'} + E_i - E_f\right), \tag{3.2}$$

where P_i is the probability that the scatterer is initially in a state $|i\rangle$, V_{int} is the interaction potential that describes the interaction between the neutron and the scatterer, and $|f\rangle$ is the final state of the scatterer. $E_{\mathbf{k}}$ and $E_{\mathbf{k}'}$ are the initial and final energies of the neutron, such that $E_{\mathbf{k}} - E_{\mathbf{k}'} = \hbar\omega$, and E_i and E_f are the energies of the initial and final states of the Hamiltonian of the scatterer, that is $\mathcal{H}|i\rangle = E_i|i\rangle$ and $\mathcal{H}|f\rangle = E_i|f\rangle$. The sum is over all final and initial states. Information about the scatterer is extracted by measuring the energy transfer $\hbar\omega$ and momentum transfer $\hbar\mathbf{Q}$ of the neutron, where $\mathbf{Q} = \mathbf{k} - \mathbf{k}'$ is the scattering wave-vector [41].

The basic formulation of the neutron scattering cross section in terms of experimentally controllable or measurable parameters is defined in Eqn. (1.6). In terms of the microscopic interaction of the neutron with the scatterer [41]

$$\delta N = \frac{V}{(2\pi)^3}\left(\mathbf{k}'\right)^2 d|\mathbf{k}'|d\Omega = \frac{V}{(2\pi)^3}\frac{M|\mathbf{k}'|}{\hbar^2}dEd\Omega, \tag{3.3}$$

is the number of neutrons within the energy range dE, directly related to the wave-vector of the neutrons, and solid angle range (corresponding to a range of $\mathbf{k}'/|\mathbf{k}'|$) $d\Omega$. The flux,

$\mathbf{j}(\mathbf{k}, \mathbf{s}_n)$ of inbound neutrons with wave-vector $\mathbf{k}$ and spin $\mathbf{s}_n$ is given by $\hbar\mathbf{k}/(VM)$. Using these definitions, Eqn. (1.6) yields (Eqn. 4.1.4a in Ref. [41])

$$\frac{d^2\sigma}{d\Omega dE} = \frac{|\mathbf{k}'|}{|\mathbf{k}|}\left(\frac{M}{2\pi\hbar^2}\right)^2 \sum_{i,f} P_i |\langle \mathbf{s}_n; i|V_{\text{int}}(\mathbf{Q})|\mathbf{s}'_n; f\rangle|^2 \delta\left(E_{\mathbf{k}} - E_{\mathbf{k}'} + E_i - E_f\right), \tag{3.4}$$

where $V_{\text{int}}(\mathbf{Q})$ is the Fourier transform of the neutron-scatterer interaction potential (Eqn. 4.1.4b in Ref. [41])

$$V_{\text{int}}(\mathbf{Q}) = \int V_{\text{int}} \exp(i\mathbf{Q}\cdot\mathbf{r}_n)\, d\mathbf{r}_n, \tag{3.5}$$

where $\mathbf{r}_n$ is the position of the neutron.

Now we can move on to defining the neutron-scatterer interaction potential V_{int}. The magnetic interaction between the magnetic moment of a neutron and the magnetic field due to a single electron with momentum $\mathbf{p}$ is is described by the potential, in CGS-Gaussian units, (Eqn. 4.1.5 in Ref. [41])

$$\begin{aligned} V_{\text{int}}(\mathbf{r}_e, \mathbf{r}_n) &= \frac{1}{2m}\left(\mathbf{p} + \frac{e}{c}(\mathbf{A}_n + \mathbf{A}_e)\right)^2 - \frac{1}{2m}\left(\mathbf{p} + \frac{e}{c}\mathbf{A}_e\right)^2 + 2\mu_{\text{B}}\mathbf{s}\cdot\mathbf{B}_n \\ &= 2\mu_B\left(\frac{1}{\hbar}\mathbf{A}_n\cdot\mathbf{p}' + \mathbf{s}\cdot(\nabla\times\mathbf{A}_n)\right), \end{aligned} \tag{3.6}$$

where $\mathbf{r}_e$ and $\mathbf{r}_n$ are the position of the electron and neutron respectively, $\mathbf{p}$ is the momentum of the electron, and $\mathbf{A}_n$ is the magnetic vector potential due to the magnetic moment of the neutron $\boldsymbol{\mu}_n$, such that $\mathbf{B}_n = \nabla\times\mathbf{A}_n = \nabla\times\left(-\boldsymbol{\mu}_n\times\nabla\left(\frac{1}{r}\right)\right)$. $\mathbf{A}_e$ is the additional contribution to the total magnetic vector potential from the surrounding electrons in the scatterer or an external field. $\mathbf{s}$ is the spin of the electron, $\mu_B = 9.274\times10^{-24}$ J/T is the Bohr magneton, e is the absolute value of the charge on an electron, and c is the speed of light. $\mathbf{p}' = \mathbf{p} + \frac{e}{c}\mathbf{A}_e$ is the adjusted electron momentum. The Fourier transform of $\mathbf{A}_n$, with respect to the neutron coordinate is given by [41]

$$\int \mathbf{A}_n(\mathbf{r}_e - \mathbf{r}_n)\exp(i\mathbf{Q}\cdot\mathbf{r}_n)\, d\mathbf{r}_n = -\exp(-i\mathbf{Q}\cdot\mathbf{r}_e)\frac{4\pi}{i|\mathbf{q}|}\boldsymbol{\mu}_n\times\hat{\mathbf{Q}}, \tag{3.7}$$

where $\boldsymbol{\mu}_n$ is the magnetic moment of the neutron, and $\hat{\mathbf{Q}}$ is a unit vector in the direction of $\mathbf{Q}$. The Fourier transform of $\nabla\times\mathbf{A}_n$ is given by [41]

$$\int \nabla\times\mathbf{A}_n(\mathbf{x})\exp(i\mathbf{Q}\cdot\mathbf{x})\, d\mathbf{x} = 4\pi\hat{\mathbf{Q}}\times\boldsymbol{\mu}_n\times\hat{\mathbf{Q}}. \tag{3.8}$$

Combining the results of Eqn. (3.7) and Eqn. (3.8) with Eqn. (3.6), we obtain (Eqn. 4.1.6 in Ref. [41])

$$\begin{aligned} V_{\text{int}}(\mathbf{Q}) &= \int V_{\text{int}}(\mathbf{r}_e - \mathbf{r}_n) \exp(i\mathbf{Q}\cdot\mathbf{r}_n)\, d\mathbf{r}_n \\ &= 8\pi\mu_B \boldsymbol{\mu}_n \cdot \left(\frac{i}{\hbar|\mathbf{Q}|}\hat{\mathbf{Q}}\times\mathbf{p}' + \hat{\mathbf{Q}}\times\mathbf{s}\times\hat{\mathbf{Q}} \right) \exp(-i\mathbf{Q}\cdot\mathbf{r}_e) \end{aligned} \tag{3.9}$$

In the case of rare earth ions, such as $Yb_2Ti_2O_7$, we can impose a further restriction on the interaction between the neutron and electron: that the electrons are localized around the Yb^{3+} lattice sites, thus $\mathbf{r}_e = \mathbf{R}_i^a + \mathbf{r}$. This allows us to rewrite Eqn. (3.9) as (Eqn. 4.1.7a in Ref. [41])

$$V_{\text{int}}(\mathbf{Q}) = 8\pi\mu_B \boldsymbol{\mu}_n \cdot (\mathbf{Z}_p + \mathbf{Z}_s) \exp(-i\mathbf{Q}\cdot\mathbf{R}_i^a), \tag{3.10}$$

where (Eqn. 4.1.7b in Ref. [41])

$$\mathbf{Z}_p = \frac{i}{\hbar|\mathbf{Q}|}\hat{\mathbf{Q}}\times\mathbf{p}'\exp(-i\mathbf{Q}\cdot\mathbf{r}) \tag{3.11}$$

and

$$\mathbf{Z}_s = \hat{\mathbf{Q}}\times\mathbf{s}\times\hat{\mathbf{Q}}\exp(-i\mathbf{Q}\cdot\mathbf{r}). \tag{3.12}$$

In order to compute the matrix elements $\langle i|\mathbf{Z}_{p,s}|f\rangle$, it is explained in Ref. [41], that we must expand the the factor $\exp(-i\mathbf{Q}\cdot\mathbf{r})$ in $\mathbf{Z}_p$ and $\mathbf{Z}_s$ in terms of Bessel functions $j_n(\rho)$, where $\rho = |\mathbf{Q}||\mathbf{r}|$, and $\cos(\theta) = \mathbf{Q}\cdot\mathbf{r}/\rho$. This expansion has the form (Eqn. 4.1.8 in Ref. [41])

$$\exp(-i\mathbf{Q}\cdot\mathbf{r}) = \sum_{n=0}^{\infty}(2n+1)(-i)^n j_n(\rho)P_n(\cos(\theta)), \tag{3.13}$$

where P_n is n^{th} Legendre polynomial. If we perform this expansion for $\mathbf{Z}_p$, we obtain the result [41]:

$$\mathbf{Z}_p = \mathbf{Q}\times\left(\frac{i}{\hbar|\mathbf{Q}|}j_0(\rho)\mathbf{p}' + \frac{1}{\hbar}\{j_0(\rho)+j_2(\rho)\}\left(\hat{\mathbf{Q}}\cdot\mathbf{r}\right)\mathbf{p}' + \ldots \right). \tag{3.14}$$

This result can then be rearranged and expressed as (Eqn. 4.1.9a in Ref. [41])

$$\mathbf{Z}_p = \frac{1}{2}\{j_0(\rho)+j_2(\rho)\}\hat{\mathbf{Q}}\times\mathbf{l}'\times\hat{\mathbf{Q}} + \mathbf{Z}_p', \tag{3.15}$$

where (Eqn. 4.1.9b in Ref. [41])

$$\mathbf{Z}'_p = \hat{\mathbf{Q}} \times \left(\frac{i}{\hbar|\mathbf{Q}|} j_0(\rho)\mathbf{p}' + \frac{1}{2\hbar}\{j_0(\rho) + j_2(\rho)\}\{(\hat{\mathbf{Q}} \cdot \mathbf{r})\mathbf{p}' - (\hat{\mathbf{Q}} \cdot \mathbf{p}')\mathbf{r}\} + \dots \right) \tag{3.16}$$

contains all of the remaining terms in the expansion of $\mathbf{Z}_p$. $\hbar\mathbf{l}' = \hbar\mathbf{l} + \frac{e}{c}\mathbf{r} \times \mathbf{A}_e$, where $\mathbf{l} = \frac{\mathbf{r}\times\mathbf{p}}{\hbar}$ is the angular momentum. Ref. [41] shows that because $\mathbf{p}' = \frac{im}{\hbar}[\mathcal{H}, \mathbf{r}]$, all of the terms in $\mathbf{Z}'_p$ can be expressed in terms of commutators with $\mathcal{H}$ so that (Eqn. 4.1.10 in Ref. [41])

$$\mathbf{Z}'_p = \frac{m}{\hbar^2|\mathbf{Q}|}\hat{\mathbf{Q}} \times \left(-j_0(\rho)[\mathcal{H}, \mathbf{r}] + \frac{i|\mathbf{Q}|}{2}\{j_0(\rho) + j_2(\rho)\}[\mathcal{H}, \left(\hat{\mathbf{Q}} \cdot \mathbf{r}\right)\mathbf{r}] + \dots \right). \tag{3.17}$$

For any operator $\hat{\mathbf{A}}$, $\langle i|[\mathcal{H}, \hat{\mathbf{A}}]|f\rangle = (E_i - E_f)\langle i|\hat{\mathbf{A}}|f\rangle$, which means that in the limit $\mathbf{Q} \to 0$, this term will not contribute to $\langle i|\mathbf{Z}_p|f\rangle$, because $E_f \to E_i$ as $\mathbf{Q} \to 0$.

The expansion of $\mathbf{Z}_p$ has shown that the leading term in $\mathbf{Z}_p$ is of the form $\hat{\mathbf{Q}} \times A\mathbf{l}' \times \hat{\mathbf{Q}}$, where $A = \frac{1}{2}\{j_0(\rho) + j_2(\rho)\}$, which is the same general form as that of $\mathbf{Z}_s$ in Eqn. (3.12). This allows us to define the new vector operator $\mathbf{K}(\mathbf{Q})$ such that (Eqn. 4.1.11 in Ref. [41])

$$\hat{\mathbf{Q}} \times \mathbf{K} \times \hat{\mathbf{Q}} = \mathbf{Z}_p + \mathbf{Z}_s. \tag{3.18}$$

In the limit $\mathbf{Q} \to 0$ (Eqn. 4.1.12a [41])

$$2\mu_B\mathbf{K}(0) = \mu_B\left(\mathbf{l} + \frac{e}{\hbar c}\mathbf{r} \times \mathbf{A}_e + 2\mathbf{s}\right) = -\boldsymbol{\mu}_e, \tag{3.19}$$

where $\boldsymbol{\mu}_e$ is the magnetic dipole moment of the electron. This yields the result (Eqn. 4.1.12b [41])

$$V_{\text{int}}(0) = -4\pi\boldsymbol{\mu}_B \cdot \left(\hat{\mathbf{Q}} \times \boldsymbol{\mu}_e \times \hat{\mathbf{Q}}\right). \tag{3.20}$$

In the case where $\mathbf{Q} \neq 0$, an analytic solution for $V_{\text{int}}(\mathbf{Q})$ is almost impossible to obtain because $\mathbf{Z}'_p$ cannot be neglected and $j_n(\rho)$ do not commute with $\mathcal{H}$ [41]. However, if the scattering processes are restricted to those where the orbital quantum number l of the electron is conserved, then the first term in Eqn. (3.17) vanishes identically because $j_0(\rho)$ and $\mathcal{H}$ are diagonal in l. In the second term of Eqn. (3.17), it is possible to replace $\mathcal{H}$ with only the kinetic term of the Hamiltonian to first order if l is conserved. It is then shown in Ref. [41], that if the principal quantum number n and the angular momentum quantum number l are conserved between $|i\rangle$ and $|f\rangle$ states, the electron wave-function is radially symmetric and the second term in Eqn. (3.17) also vanishes identically [41]. If n is not conserved, or if $\mathcal{H}$ is not diagonal in l, then this term will lead to an imaginary contribution

to $\mathbf{K}(\mathbf{Q})$, and a contribution to the neutron scattering cross section proportional to $\mathbf{Q}^2$, however this contribution is normally very small [41].

The assumption that n and l are conserved between the $|i\rangle$ and $|f\rangle$, so that the two highest order terms in Eqn. (3.17) are negligible means that $\mathbf{K}_p$, the portion of $\mathbf{K}(\mathbf{Q})$ arising from $\mathbf{Z}_p$ is given by (Eqn. 4.1.13a in Ref. [41])

$$\mathbf{K}_p(\mathbf{Q}) = \frac{1}{2}\left\{\langle j_0(|\mathbf{Q}|)\rangle + \langle j_2(|\mathbf{Q}|)\rangle\right\}\mathbf{l}. \tag{3.21}$$

$\langle j_n(|\mathbf{Q}|)\rangle$ is defined as (Eqn. 4.1.13b in Ref. [41])

$$\langle j_n(|\mathbf{Q}|)\rangle = \int_0^\infty r^2 R^2(r) j_n(|\mathbf{Q}|r)dr, \tag{3.22}$$

where $R(r)$ is the normalized radial electron wave-function [41].

The spin contribution to $\mathbf{K}(\mathbf{Q})$, $\mathbf{K}_s(\mathbf{Q})$ is given by $\mathbf{K}_s(\mathbf{Q}) \approx \langle j_0(|\mathbf{Q}|)\rangle\mathbf{s}$, neglecting terms of order greater than $n = 2$ [41]. Adding the two contributions to $\mathbf{K}(\mathbf{Q})$ yields (Eqn. 4.1.14 in Ref. [41])

$$\mathbf{K}(\mathbf{Q}) = \frac{1}{2}\langle j_0(|\mathbf{Q}|)\rangle(\mathbf{l}+2\mathbf{s}) + \frac{1}{2}\langle j_2(|\mathbf{Q}|)\rangle\mathbf{l}. \tag{3.23}$$

This result can be generalized to an ion with more than one electron using the relations $\mathbf{L} = \sum \mathbf{l}$ and $\mathbf{S} = \sum \mathbf{s}$ to yield (Eqn. 4.1.15a in Ref. [41])

$$\mathbf{K}(\mathbf{Q}) = \frac{1}{2}\langle j_0(|\mathbf{Q}|)\rangle(\mathbf{L}+2\mathbf{S}) + \frac{1}{2}\langle j_2(|\mathbf{Q}|)\rangle\mathbf{L} = \frac{1}{2}g_J F(|\mathbf{Q}|)\mathbf{J}. \tag{3.24}$$

g_J is the Landé factor, $F(|\mathbf{Q}|) = \langle j_0(|\mathbf{Q}|)\rangle + \left(\frac{2}{g_J} - 1\right)\langle j_2(|\mathbf{Q}|)\rangle$ is the magnetic form factor, and $\mathbf{J}$ is the angular momentum operator of the ion the neutron is interacting with. The magnetic form factor for Yb^{3+} is given in Appendix F.

We now return to Eqn. (3.10), where, substituting in Eqn. (3.18), the form of $\mathbf{K}(\mathbf{Q})$ from Eqn. (3.24), and taking the sum over all of the Yb^{3+} lattice sites, we obtain [41]

$$V_{\text{int}}(\mathbf{Q}) = 8\pi\mu_B \sum_{i,a}\left(\frac{1}{2}g_J F(|\mathbf{Q}|)\right)\boldsymbol{\mu}_n \cdot \left(\hat{\mathbf{Q}} \times \mathbf{J}_i^a \times \hat{\mathbf{Q}}\right)\exp\left(-i\mathbf{Q}\cdot\mathbf{R}_i^a\right), \tag{3.25}$$

where $\mathbf{J}_i^a$ is the angular momentum operator for the ion at lattice site i and sublattice site a. The sum over the Yb^{3+} lattice sites takes us from the single ion scattering problem to the crystal scattering problem.

Now that we have determined the form of the interaction potential between the neutron and the scatterer, we can return our attention to the neutron scattering cross section. We now wish to compute the matrix element squared term in Eqn. (3.4). This term can be written as [41]

$$|\langle \mathbf{k}\mathbf{s}_n; i|V_{\text{int}}(\mathbf{Q})|\mathbf{k}'\mathbf{s}'_n; f\rangle|^2 = \langle \mathbf{s}_n; i|V_{\text{int}}(\mathbf{Q})|\mathbf{s}'_n; f\rangle\langle \mathbf{s}'_n; f|V_{\text{int}}(-\mathbf{Q})|\mathbf{s}_n; i\rangle. \tag{3.26}$$

In this study, we are only interested in unpolarized neutron scattering, so we assume an equal distribution of neutrons with spin up and spin down. Therefore, [41]

$$\begin{aligned}\sum_{\mathbf{s}_n,\mathbf{s}'_n} P_s\langle \mathbf{s}_n|\boldsymbol{\mu}_n\cdot\left(\hat{\mathbf{Q}}\times\mathbf{J}_i^a\times\hat{\mathbf{Q}}\right)|\mathbf{s}'_n\rangle\langle \mathbf{s}'_n|\boldsymbol{\mu}_n\cdot\left(\hat{\mathbf{Q}}\times\mathbf{J}_j^b\times\hat{\mathbf{Q}}\right)|\mathbf{s}_n\rangle \\ = \left(\frac{1}{2}g_n\mu_N\right)^2\left(\hat{\mathbf{Q}}\times\mathbf{J}_i^a\times\hat{\mathbf{Q}}\right)\cdot\left(\hat{\mathbf{Q}}\times\mathbf{J}_j^b\times\hat{\mathbf{Q}}\right) \qquad (3.27)\\ = \left(\frac{1}{2}g_n\mu_N\right)^2\sum_{u,v}\left(\delta_{u,v}-\hat{Q}_u\hat{Q}_v\right)J_i^{a,u}J_j^{b,v}, \qquad (3.28)\end{aligned}$$

where $g_n = 3.827$ [41] is the nuclear g factor, and μ_N is the nuclear magneton, such that $\boldsymbol{\mu}_n = -g_n\mu_N\mathbf{s}_n$. u and v are cartesian components. This result gives us one of the key aspects of neutron scattering measurements: that they measure only the correlations between the components of the magnetic moments perpendicular to the scattering wave-vector $\mathbf{Q}$. This condition is imposed by the term $\left(\delta_{u,v}-\hat{Q}_u\hat{Q}_v\right)$. This arises from the form of the Fourier transform of the interaction between the moment of the neutron and magnetic field due to the electrons, specifically the term involving the curl of the vector potential of the field due to the magnetic dipole moment of the neutron in Eq. (3.6).

Combining Eqn. (3.28) with Eqn. (3.4), we obtain the final form of the neutron scattering cross section (Eqn. 4.1.16 in Ref. [41])

$$\begin{aligned}\frac{d^2\sigma}{d\Omega dE} = \frac{|\mathbf{k}'|}{|\mathbf{k}|}\left(\frac{\hbar\gamma e^2}{mc^2}\right)^2\sum_{u,v}\left(\delta_{u,v}-\hat{Q}_u\hat{Q}_v\right)\sum_{i,a;j,b}\left(\frac{1}{2}g_J F(|\mathbf{Q}|)\right)_{i,a}\left(\frac{1}{2}g_J F(|\mathbf{Q}|)\right)_{j,b} \\ \times\sum_{i,f}P_i\langle i|J_i^{a,u}\exp\left(-i\mathbf{Q}\cdot\mathbf{R}_i^a\right)|f\rangle\langle f|J_j^{b,v}\exp\left(i\mathbf{Q}\cdot\mathbf{R}_j^b\right)|i\rangle\delta\left(E_{\mathbf{k}}-E_{\mathbf{k}'}+E_i-E_f\right), \qquad (3.29)\end{aligned}$$

where $\gamma = e^2/mc^2$ is the gyromagnetic ratio, and m is the mass of the electron.

Next we examine the integral form of the δ function [41]

$$\delta\left(E_{\mathbf{k}}-E_{\mathbf{k}'}+E_i-E_f\right) = \frac{1}{2\pi\hbar}\int_{-\infty}^{\infty}\exp\left(i\left(E_{\mathbf{k}}-E_{\mathbf{k}'}+E_i-E_f\right)t/\hbar\right)dt. \tag{3.30}$$

We can use this formulation of the δ function to write [41]

$$\begin{aligned}
&\sum_{i,f} P_i \langle i|J_i^{a,u}|f\rangle\langle f|J_j^{b,v}|i\rangle \delta\left(E_{\mathbf{k}} - E_{\mathbf{k}'} + E_i - E_f\right) \\
&= \sum_{i,f} \frac{1}{2\pi\hbar} \int_{-\infty}^{\infty} dt \exp\left(i\omega t\right) P_i \langle i| \exp\left(i\mathcal{H}t\right) J_i^{a,u} \exp\left(-i\mathcal{H}t\right) |f\rangle\langle f|J_j^{b,v}|i\rangle \\
&= \frac{1}{2\pi\hbar} \int_{-\infty}^{\infty} dt \exp\left(i\omega t\right) \sum_i P_i \langle i|J_i^{a,u}\left(t\right) J_j^{b,v}\left(0\right)|i\rangle \\
&= \frac{1}{2\pi\hbar} \int_{-\infty}^{\infty} dt \exp\left(i\omega t\right) \langle J_i^{a,u}\left(t\right) J_j^{b,v}\left(0\right)\rangle
\end{aligned} \tag{3.31}$$

where we have used the fact that $E_{\mathbf{k}} - E_{\mathbf{k}'} = \hbar\omega$. $\mathcal{H}$ is the Hamiltonian of the scatterer, and $J_i^{a,u}(t)$ is the angular momentum operator for the ion at lattice site i sublattice site a in the Heisenberg picture. Then at thermal equilibrium, combining Eqn. (3.31) with Eqn. (3.29), we can write (Eqn. 4.2.1 in Ref. [41])

$$\begin{aligned}
\frac{d^2\sigma}{d\Omega dE} = \frac{|\mathbf{k}'|}{|\mathbf{k}|}\left(\frac{\hbar\gamma e^2}{mc^2}\right)^2 \sum_{u,v}\left(\delta_{u,v} - \hat{q}_u\hat{q}_v\right) \sum_{i,a;j,b} \left(\frac{1}{2} g_J F(|\mathbf{Q}|)\right)_{i,a} \left(\frac{1}{2} g_J F(|\mathbf{Q}|)\right)_{j,b} \\
\times \frac{1}{2\pi\hbar} \int_{-\infty}^{\infty} dt \exp\left(i\omega t\right) \exp\left(i\mathbf{Q}\cdot\left(\mathbf{R}_i^a - \mathbf{R}_j^b\right)\right) \langle J_i^{a,u}\left(t\right) J_j^{b,v}\left(0\right)\rangle,
\end{aligned} \tag{3.32}$$

where we have neglected thermal fluctuations of the positions of the ions, $\mathbf{R}_i^a$, because we fix the ions to be at the sites $\mathbf{R}_i^a$ and do not allow for any fluctuations in these positions. If we were to include such fluctuations by letting $\mathbf{R}_i^a \rightarrow \tilde{\mathbf{R}}_i^a = \mathbf{R}_i^a + \mathbf{u}_i^a$, where $\mathbf{u}_i^a$ is some small fluctuation in the position of the ion at site $\mathbf{R}_i^a$ then we can write [41] $\langle \exp\left(\tilde{\mathbf{R}}_i^a - \tilde{\mathbf{R}}_j^b\right)\rangle = \exp\left(-2W(\mathbf{Q})\right) \exp\left(\mathbf{R}_i^a - \mathbf{R}_j^b\right)$, where $W(\mathbf{Q})$ is the Debye-Waller factor. This new exponential term would then appear in Eqn. (3.32). For a further discussion of the Debye-Waller factor, see Ref. [41].

If the magnetic form factor of all of the ions are the same, which is the case for $Yb_2Ti_2O_7$, we can take the form factor outside the sum (Eqn. 4.2.2a in Ref. [41])

$$\frac{d^2\sigma}{d\Omega dE} = N\frac{|\mathbf{k}'|}{|\mathbf{k}|}\left(\frac{\hbar\gamma e^2}{mc^2}\right)^2 \sum_{u,v}\left(\delta_{u,v} - \hat{q}_u\hat{q}_v\right) \left|\frac{1}{2} g_J F(|\mathbf{Q}|)\right|^2 \sum_{a,b} \mathcal{S}_{ab}^{uv}\left(\mathbf{Q},\omega\right), \tag{3.33}$$

where $\mathcal{S}_{ab}^{uv}(\mathbf{Q},\omega)$ is the Van Hove scattering function (Eqn. 4.2.2b in Ref. [41])

$$\mathcal{S}_{ab}^{uv}\left(\mathbf{Q},\omega\right) = \frac{1}{2\pi\hbar}\int_{-\infty}^{\infty} \exp\left(i\omega t\right) \frac{1}{N} \sum_{i,j} \exp\left(i\mathbf{Q}\cdot\left(\mathbf{R}_i^a - \mathbf{R}_j^b\right)\right) \langle J_i^{a,u}\left(t\right) J_j^{b,v}\left(0\right)\rangle dt, \tag{3.34}$$

which is simply $1/(2\pi\hbar)$ times the Fourier transform of the correlation function $\langle J_i^{a,u}(t) J_j^{b,v}(0)\rangle$ [41].

3.2 The Relationship Between Quasi-elastic Neutron Scattering and the Q-dependent Magnetic Susceptibility

We saw in the previous section that in order to compute the neutron scattering cross section a method for computing the van Hove scattering function, $\mathcal{S}_{ab}^{uv}(\mathbf{Q},\omega)$, is required. In this section we will show the relationship between $\mathcal{S}_{ab}^{uv}(\mathbf{Q},\omega)$ and the wave-vector dependent magnetic susceptibility in the static approximation.

We start with the generalized susceptibility, $\chi_{BA}(\omega)$, a measure of the change of an ensemble averaged physical observable $\hat{B}$ to a perturbation by some operator $\hat{A}$. The generalized susceptibility has two components

$$\chi_{AB}(\omega) = \chi'_{AB}(\omega) + i\chi''_{AB}(\omega), \tag{3.35}$$

where $\chi'_{AB}(\omega)$ is referred to as the reactive part of $\chi_{AB}(\omega)$ and $\chi''_{AB}(\omega)$ is referred to as the absorptive part of $\chi_{AB}(\omega)$. If the matrix elements $\langle i|\hat{B}|f\rangle$ and $\langle f|\hat{A}|i\rangle$ are real, then $\chi'_{AB}(\omega)$ and $\chi''_{AB}(\omega)$ are the real and imaginary parts of $\chi_{AB}(\omega)$ respectively. $\chi'_{AB}(\omega)$ is given by (Eqn. 3.3.6a in Ref. [41])

$$\chi'_{AB}(\omega) = \sum_{if}^{E_i \neq E_f} \frac{\langle i|\hat{B}|f\rangle\langle f|\hat{A}|i\rangle}{E_i - E_f - \hbar\omega}(n_i - n_f) + \chi'_{AB}(el)\,\delta_{\omega=0}, \tag{3.36}$$

where (Eqn. 3.3.6b in Ref. [41])

$$\chi'_{AB}(el) = \beta\left(\sum_{if}^{E_i=E_f} \langle i|\hat{B}|f\rangle\langle f|\hat{A}|i\rangle n_i - \langle B\rangle\langle A\rangle\right). \tag{3.37}$$

$\beta = \frac{1}{k_B T}$, and $n_\alpha = \exp(-\beta E_\alpha)/Z$ is the thermal occupation number of state $|\alpha\rangle$, and Z is the partition function. $\chi''_{AB}(\omega)$ is given by (Eqn. 3.3.5 in Ref. [41])

$$\chi''_{AB}(\omega) = \pi\sum_{if}\langle i|\hat{B}|f\rangle\langle f|\hat{A}|i\rangle(n_i - n_f)\,\delta(\hbar\omega - (E_i - E_f)). \tag{3.38}$$

To obtain the wave-vector dependent magnetic susceptibility, we take the generalized susceptibility and choose

$$\hat{A} = N^{-1/2} \sum_i J_i^{a,u} \exp\left(-i\mathbf{Q}\cdot\mathbf{R}_i^a\right)$$

and

$$\hat{B} = N^{-1/2} \sum_j J_j^{b,v} \exp\left(i\mathbf{Q}\cdot\mathbf{R}_j^b\right),$$

to create the quantity $\chi_{a,b}^{u,v}(\mathbf{Q},\omega)$.

In the previous section, we showed that the neutron scattering cross section is proportional to the van Hove scattering function, $\frac{d\sigma}{d\Omega} \propto \mathcal{S}_{ab}^{uv}(\mathbf{Q},\omega)$. This is simply a Fourier transformed two operator correlation function, where the operators are $J_i^{a,u}$ and $J_j^{b,v}$, which correspond to our choice of $\hat{A}$ and $\hat{B}$ to define the wave-vector dependent magnetic susceptibility. According to Ref. [43], in the case of paramagnetic scattering near a phase transition we can write (Eqn. 13.17 in Ref. [43])

$$\mathcal{S}_{ab}^{uv}(\mathbf{Q},\omega) - \mathcal{S}_{ab,\text{Bragg}}^{uv}(\mathbf{Q},\omega) \propto \frac{1}{\left(g_J\mu_B\right)^2}\chi_{a,b}^{u,v}(\mathbf{Q},\omega) \times \omega\left(1-\left(\exp(-\beta\hbar\omega)\right)\right)^{-1} F_{ab}^{uv}(\mathbf{Q},\omega), \tag{3.39}$$

where $\mathcal{S}_{ab,\text{Bragg}}^{uv}(\mathbf{Q},\omega)$ is the Bragg scattering due to any finite value of $\langle J_i^{a,u}\rangle$, which is very small in the paramagnetic phase and contributes only at $\omega = 0$ [43]. $F_{ab}^{uv}(\mathbf{Q},\omega)$ is the spectral weight function, which we will discuss shortly. This equation has been modified from the simple case of Ref. [43] to include sublattice structure. Equation (3.39) arrises from the fact that (Eqn. 13.9 in Ref. [43])

$$\mathcal{S}_{ab}^{uv}(\mathbf{Q},\omega) = \omega\left(1-\exp\left(-\hbar\omega\beta\right)\right)^{-1}\mathcal{R}_{ab,\mathbf{Q}}^{uv}(\omega) + \delta(\hbar\omega)\langle J_a^u\rangle\langle J_b^v\rangle, \tag{3.40}$$

where $\mathcal{R}_{ab,\mathbf{Q}}^{uv}(\omega)$ is the Fourier transform of the relaxation function $\mathcal{R}_{ab,\mathbf{Q}}^{uv}(t)$, which describes the relaxation of the magnetization due to a discontinuous magnetic field [43]. From this, it can be shown that (Eqn. 13.11 in Ref. [43])

$$\int_{-\infty}^{\infty} d\omega \left(\frac{1-\exp(-\hbar\omega\beta)}{\omega}\right)\left(\mathcal{S}_{ab}^{uv}(\mathbf{Q},\omega) - \mathcal{S}_{ab,\text{Bragg}}^{uv}\right) = \mathcal{R}_{ab,\mathbf{Q}}^{uv}(t=0), \tag{3.41}$$

and from Eqn. 13.12 of Ref. [43], $\mathcal{R}_{ab,\mathbf{Q}}^{uv}(t=0) = \frac{N}{(g_j\mu_b)^2}\chi_{a,b}^{u,v}(\mathbf{Q},\omega)$. Using this relation between $\mathcal{R}_{ab,\mathbf{Q}}^{uv}$ and $\chi_{a,b}^{u,v}(\mathbf{Q},\omega)$ then allows us to invert Eqn. (3.41) to obtain Eqn. (3.39). The spectral weight function $F(\mathbf{Q},\omega)$ is included in Eqn. (3.39) to account for the energy

dependence of the inelastic neutron scattering intensity, and is defined as (Eqn. 13.15 in Ref. [43])

$$F_{ab}^{uv}(\mathbf{Q},\omega) = \frac{1}{2\pi}\int_{-\infty}^{\infty} dt \exp\left(-i\omega t\right)\left(\frac{\mathcal{R}_{ab,\mathbf{Q}}^{uv}(t)}{\mathcal{R}_{ab,\mathbf{Q}}^{uv}(t=0)}\right) \tag{3.42}$$

So far we have considered the fully general equation for the energy dependent neutron scattering, Eqn. (3.33), which contains both the elastic and inelastic neutron scattering. The inelastic scattering is the scattering where energy of the scattered neutrons is not conserved, while elastic scattering is scattering where the energy of the neutrons is exactly conserved. In order to obtain the quasi-elastic portion of the neutron scattering cross section we use the static approximation.

The static approximation states that if the difference in energy of the incoming and scattered neutrons is sufficiently small the conservation of energy in Eqn. (3.4) can be neglected. This disregard for conservation of energy is allowed due to lack of fine energy resolution in the detector and the fact that the energy spectrum of the states of the scatterer involved in the response to the neutron is bounded, with a bandwidth much less than the energy of the incoming neutrons. More explicitly, the static approximation assumes that $E_{\mathbf{k}} \gg E_i$ and $E_{\mathbf{k}'} \gg E_f$, so that $\delta\left(\hbar\omega - (E_i - E_f)\right) \approx \delta(\hbar\omega)$ [44]. This means that $E_{\mathbf{k}} \approx E_{\mathbf{k}'}$ and $|\mathbf{k}'|/|\mathbf{k}| \sim 1$ [44]. This approximation allows us to then simply integrate over dE in Eqn. (3.29) removing the energy dependence of $d\sigma^2/dEd\Omega$ and removing $\delta(\hbar\omega)$ leaving the rest of Eqn. (3.29) [44]. This means that all information about the time dependence of the correlations in Eqn. (3.32) is lost, which is why it is called the static approximation. The static approximation also involves the approximation that for small ω, $(1+\exp(-\beta\hbar\omega))^{-1} \approx (\beta\hbar\omega)^{-1}$, giving us

$$\mathcal{S}_{ab}^{uv}\left(\mathbf{Q},\omega=0\right) - \mathcal{S}_{ab,\mathrm{Bragg}}^{uv}\left(\mathbf{Q},\omega=0\right) \;\propto\; k_{\mathrm{B}}T\frac{1}{\left(g_J\mu_B\right)^2}\chi_{a,b}^{u,v}\left(\mathbf{Q},\omega=0\right), \tag{3.43}$$

where the proportionality now includes the $\omega = 0$ value of the spectral weight function $F(\mathbf{Q},\omega)$. Finally, we can place this result into our equation for the neutron scattering cross section to obtain

$$\frac{d\sigma}{d\Omega} \propto k_{\mathrm{B}}T\left|F(|\mathbf{Q}|)\right|^2 \sum_{u,v}\left(\delta_{u,v} - \hat{q}_u\hat{q}_v\right)\sum_{a,b}\chi_{a,b}^{u,v}\left(\mathbf{Q}\right), \tag{3.44}$$

the quasi-elastic neutron scattering cross section in terms of the wave-vector dependent magnetic susceptibility in the static approximation. This result is in agreement with

Ref. [45]. In order to maintain consistency with Ref. [42], we choose to express $\chi^{u,v}_{a,b}(\mathbf{Q})$ in terms of $\chi^{u,v}_{a,b}(\mathbf{q})$. This is done by expanding the operators

$$\hat{A} = N^{-1/2} \sum_{i,a} J_i^{a,u} \exp\left(-i\mathbf{Q}\cdot\mathbf{R}_i^a\right)$$

and

$$\hat{B} = N^{-1/2} \sum_{j,b} J_j^{b,v} \exp\left(i\mathbf{Q}\cdot\mathbf{R}_j^b\right)$$

as

$$\begin{aligned}
\hat{A} &= N^{-1/2} \sum_{i,a} J_i^{a,u} \exp\left(-i\mathbf{Q}\cdot\mathbf{R}_i^a\right) \\
&= \sum_{i,a} \exp\left(-i\mathbf{G}\cdot\mathbf{r}_a\right) J_i^{a,u} \exp\left(-i\mathbf{q}\cdot\mathbf{R}_i^a\right) \qquad (3.45) \\
\hat{B} &= N^{-1/2} \sum_{j,b} J_j^{b,v} \exp\left(i\mathbf{Q}\cdot\mathbf{R}_j^b\right) \\
&= \sum_{i,a} \exp\left(i\mathbf{G}\cdot\mathbf{r}_b\right) J_i^{a,u} \exp\left(i\mathbf{q}\cdot\mathbf{R}_j^b\right). \qquad (3.46)
\end{aligned}$$

This allows us to write:

$$\chi^{u,v}_{a,b}(\mathbf{Q}) = \exp\left(-i\left(\mathbf{r}^a - \mathbf{r}^b\right)\cdot\mathbf{G}\right)\chi^{u,v}_{a,b}(\mathbf{q}), \qquad (3.47)$$

where $\chi^{u,v}_{a,b}(\mathbf{q})$ is now the generalized susceptibility for the operators

$$\hat{A} = N^{-1/2} \sum_{i} J_i^{a,u} \exp\left(-i\mathbf{q}\cdot\mathbf{R}_i^a\right)$$

and

$$\hat{B} = N^{-1/2} \sum_{j} J_j^{b,v} \exp\left(i\mathbf{q}\cdot\mathbf{R}_j^b\right).$$

This gives us the result

$$\frac{d\sigma}{d\Omega} \propto k_{\mathrm{B}}T \left|F(|\mathbf{Q}|)\right|^2 \sum_{u,v}\left(\delta_{u,v} - \hat{q}_u\hat{q}_v\right) \sum_{a,b} \exp\left(-i\left(\mathbf{r}^a - \mathbf{r}^b\right)\cdot\mathbf{G}\right)\chi^{u,v}_{a,b}(\mathbf{q}). \qquad (3.48)$$

Ref. [42] reports a different temperature dependence for $\frac{d\sigma}{d\Omega}$ than is given in Eqn. (3.48), that is (Eqn. 2 in Ref. [42])

$$\frac{d\sigma}{d\Omega} \propto \frac{1}{k_{\mathrm{B}}T} \left|F(|\mathbf{Q}|)\right|^2 \sum_{u,v}\left(\delta_{u,v} - \hat{q}_u\hat{q}_v\right) \sum_{a,b} \exp\left(-i\left(\mathbf{r}^a - \mathbf{r}^b\right)\cdot\mathbf{G}\right)\chi^{u,v}_{a,b}(\mathbf{q}). \qquad (3.49)$$

This temperature dependence is only an over all scaling factor on the neutron scattering that will be cancelled out later in the process of determining the form of the magnetic interactions in $Yb_2Ti_2O_7$, so we do not give it further consideration, but it should be noted that Eqn. (3.49) is the form used all calculations in this work.

3.3 The Random Phase Approximation Formula for Quasi-elastic Neutron Scattering

Now that we can compute the quasi-elastic neutron scattering cross section directly from the magnetic susceptibility, we require only a way to compute this quantity in terms of the CEF states of $Yb_2Ti_2O_7$ and our magnetic interaction Hamiltonian, H_{int}. To accomplish this we choose the random phase approximation (RPA). The random phase approximation arises from linear response theory, which can be used to show that many experimentally observable quantities, including the neutron scattering cross section, can be expressed in terms of two-particle correlation functions [41]. The RPA method of computing the magnetic susceptibility is discussed in Ref. [41]. The starting point for the RPA method of calculating the magnetic susceptibility is Eqn. (2.1)

$$H = H_{\text{int}} + H_{\text{CF}} \tag{3.50}$$

$$= \sum_{\langle i,a;j,b\rangle} \left(\mathbf{J}_i^a\right)^T \; \overline{\overline{\mathcal{K}}}^{a,b}(i,j)\, \mathbf{J}_j^b + H_{\text{CF}}, \tag{3.51}$$

where $\overline{\overline{\mathcal{K}}}(\mathbf{i},\mathbf{j})$ is the magnetic interaction matrix, the elements of which are given by

$$\mathcal{K}_{u,v}^{a,b}(i,j) = \mathcal{J}_{u,v}^{a,b}(i,j) + \mathcal{D}_{u,v}^{a,b}(i,j). \tag{3.52}$$

$\mathcal{J}_{u,v}^{a,b}(\mathbf{q})$ are the elements of the interaction matrix $\overline{\overline{\mathcal{J}}}$ given by Eqn. (2.5) of Chapter 2, and $\mathcal{D}_{u,v}^{a,b}(i,j)$ are the elements of the real space dipolar interaction matrix [46, 47]. The next step is to introduce the thermal expectation values of the the angular momentum operators $\langle \mathbf{J}_i^a \rangle$, and rewrite the Hamiltonian as (Eqn. 3.5.2 in Ref. [41])

$$H = \sum_{i,a} H_{\text{MF}}(i,a) - \frac{1}{2} \sum_{i,a\neq j,b} \left(\mathbf{J}_i^a - \langle \mathbf{J}_i^a \rangle\right)^T \; \overline{\overline{\mathcal{K}}}^{a,b}(i,j) \left(\mathbf{J}_j^b - \langle \mathbf{J}_j^b \rangle\right), \tag{3.53}$$

where the sum over $i, a \neq j, b$ indicates a sum over all lattice, sublattice site pairs that are not equivalent. $H_{\text{MF}}(i,a)$ is defined as (Eqn. 3.5.3 in Ref. [41])

$$H_{\text{MF}}(i,a) = H_{\text{CF}}(i,a) - \sum_{j,b} \left(\mathbf{J}_i^a - \frac{1}{2}\langle \mathbf{J}_i^a \rangle\right)^T \; \overline{\overline{\mathcal{K}}}^{a,b}(i,j) \langle \mathbf{J}_j^b \rangle, \tag{3.54}$$

where $H_{\mathrm{CF}}(i,a)$ describes the crystal field environment at the $(i,a)^{th}$ site on the pyrochlore lattice, discussed in Appendix A.

The mean field Hamiltonian, $H_{\mathrm{MF}}(i,a)$, determines the dynamic susceptibility, $\chi_a^{(0)}(\omega)$, where a labels the sublattice site. This quantity is simply the susceptibility of the magnetic moment $\mathbf{J}_i^a$ under the influence of only the CEF, because in the paramagnetic phase, the second term in Eqn. (3.54) is zero. Because the interaction term is zero, we can refer to $\chi_a^{(0)}(\omega)$ as the non-interacting susceptibility, and it is given by (Eqn. 3.5.20 in Ref. [41])

$$\chi_a^{(0)}(\omega) = \sum_{\mu,\nu}^{E_\mu \neq E_\nu} \frac{M^u_{\nu\mu,a} M^v_{\mu\nu,a}}{E_\mu - E_\nu - \hbar(\omega + i0^+)}(n_\nu - n_\mu) + \frac{\delta(\omega)}{k_B T} \sum_{\mu,\nu}^{E_\mu = E_\nu} M^u_{\nu\mu,a} M^v_{\mu\nu,a} n_\nu, \qquad (3.55)$$

where $M^u_{\nu\mu,a} = \sum_{\bar{u}} \langle \nu | \mathrm{J}^{\bar{u}} | \mu \rangle o^u_{\bar{u},a}$ and $o^u_{\bar{u},a}$ is the rotation matrix from the local $\bar{u}$ frame at sublattice site a to the global u frame. The operators $\mathrm{J}^{\bar{u}}$ act on the CEF states defined in the local $\bar{u}$ reference frames at each sublattice site. The CEF wave-functions $|\mu\rangle$ are given in Appendix A.

The next step in determining the interacting RPA susceptibility is to compute the linear response of $\langle \mathbf{J}_i^a(t) \rangle$ to a small perturbing field $\mathbf{h}_j^b(t) = g_J \mu_B \overline{\mathbf{H}}_j^b(t)$ where $\overline{\mathbf{H}}_j^b(t)$ is an applied time dependent magnetic field. If we collect all of the terms in Eqn. (3.53) that depend on $\mathbf{J}_i^a$ into an effective Hamiltonian H_i^a, we obtain (Eqn. 3.5.4 in Ref. [41])

$$H_i^a(t) = H_{\mathrm{MF}}(i,a,t) - \sum_{j,b} \left(\mathbf{J}_i^a(t) - \langle \mathbf{J}_i^a \rangle\right)^T \overline{\overline{\mathcal{K}}}^{a,b}(i,j) \left(\left(\mathbf{J}_j^b(t) - \langle \mathbf{J}_j^b \rangle\right) + \mathbf{h}_i^a(t) \right). \qquad (3.56)$$

According to Ref. [41],the difference term $\left(\mathbf{J}_j^b(t) - \langle \mathbf{J}_j^b(t) \rangle\right)$ fluctuates in an uncorrelated manner from ion to ion, making this terms contribution to Eqn. (3.56) very small so it may be neglected. This is equivalent to replacing $\mathbf{J}_j^b(t)$ with $\langle \mathbf{J}_j^b(t) \rangle$ for all terms where $i,a \neq j,b$. This is the random phase approximation, because it is equivalent to the assumption that $\left(\mathbf{J}_j^b(t) - \langle \mathbf{J}_j^b(t) \rangle\right)$ can be replaced by a random phase factor [41].

Introducing the RPA in Eqn. (3.56) the only dynamical variable left over is $\mathbf{J}_i^a(t)$ and Eqn. (3.56) becomes equivalent to the mean field Hamiltonian in Eqn. (3.54), but with $\mathbf{h}_i^a(t)$ replaced by an effective field $\mathbf{h}_{i,\mathrm{eff}}^a(t)$. The Fourier transform of this effective field is given by (Eqn. 3.5.5 in Ref. [41])

$$\mathbf{h}_{i,\mathrm{eff}}^a(\omega) = \mathbf{h}_i^a(\omega) + \sum_{j,b} \overline{\overline{\mathcal{K}}}^{a,b}(i,j) \langle \mathbf{J}_j^b(\omega) \rangle, \qquad (3.57)$$

where $\langle \mathbf{J}_j^b(\omega) \rangle$ is the Fourier transform of $\left(\mathbf{J}_j^b(t) - \langle \mathbf{J}_j^b \rangle\right)$. Using these two relations, we can write [41]

$$\langle \mathbf{J}_j^b(\omega) \rangle = \chi_a^{(0)}(\omega) \mathbf{h}_{i,\mathrm{eff}}^a(\omega). \qquad (3.58)$$

If we compare the form of Eqn. (3.57) to the response determined by the two-ion susceptibility function of the system defined as (Eqn. 3.5.6 in Ref. [41])

$$\langle \mathbf{J}_j^b(\omega) \rangle = \sum_{j,b} \chi_{ab}(i,j,\omega)\, \mathbf{h}_j^b(\omega)\,. \tag{3.59}$$

these two equations should be equivalent [41], which means that we can write (Eqn. 3.5.7 in Ref. [41])

$$\chi_{ab}(i,j,\omega) = \chi_a^{(0)}(\omega) \left(\delta_{a,b} + \sum_{k,c} \overline{\overline{\mathcal{K}}}^{a,c}(i,k)\, \chi_{cb}(k,j,\omega) \right). \tag{3.60}$$

Finally we can take the Fourier transform of real space interaction matrix $\overline{\overline{\mathcal{K}}}^{a,b}(i,j)$ to obtain the reciprocal space interaction matrix $\mathcal{K}_{u,v}^{a,b}(\mathbf{q}) = \mathcal{J}_{u,v}^{a,b}(\mathbf{q}) + \mathcal{D}_{u,v}^{a,b}(\mathbf{q})$, where $\mathcal{J}_{u,v}^{a,b}(\mathbf{q})$ is the Fourier transform of the nearest-neighbour bilinear exchange interaction matrix, as defined in Eqn. (G.3) of Appendix G and $\mathcal{D}_{u,v}^{a,b}(\mathbf{q})$ is the Fourier transform of the long-range dipolar interactions determined using the Ewald summation technique discussed in Appendix E. Expressing the final result in terms of matrix elements, we obtain the interacting RPA susceptibility $\chi(\mathbf{q},\omega)$ (Eqn. 3.5.8 [41])

$$\chi_{ab}^{uv}(\mathbf{q},\omega) + \sum_{s,t,c} \chi_a^{0,us}(\omega) \mathcal{K}_{ac}^{st}(\mathbf{q}) \chi_{cb}^{tv}(\mathbf{q},\omega) = \delta_{ab} \chi_a^{0,uv}(\omega), \tag{3.61}$$

$\chi_{ab}^{uv}(\mathbf{q},\omega)$ is then obtained by inverting Eqn. (3.61) numerically.

Now we are able compute the RPA interacting susceptibility from the CEF parameterizations of Refs. [19, 20] and our model Hamiltonian. From this we can compute the quasi-elastic neutron scattering cross section by setting $\omega = 0$. The next step is to extract the form of $\overline{\overline{\mathcal{J}}}(i,j)$ from the quasi-elastic neutron scattering measurements of Chapter 1.6. It is important to consider the validity of the use of the RPA for this calculation. For the case of $Yb_2Ti_2O_7$, as discussed in Chapter 2, the gap between the ground and first excited doublets of the CEF ($\Delta \sim 650 \pm 40$ K) is much much larger than either the energy scale of the of either H_{ex} or H_{dip}, based on the value of $\theta_{\text{CW}} = 0.75 \pm 0.05$ K [20, 18]. As explained in Ref. [31], this implies that there is minimal admixing between the ground and excited CEF doublets. These calculations are also performed at a temperature of $T = 1.4$ K, which is approximately twice θ_{CW} for this material, and six times the experimentally observed transition temperature of 214 mK [16]. This should place the system squarely in the paramagnetic regime, making the RPA valid for calculations of the susceptibility.

3.4 Summary

In this chapter we have derived the form of the magnetic neutron scattering cross-section from the microscopic interaction between the magnetic moment of the neutron and the magnetic field that arrises from the electrons in a material. This derivation exposed the fact that neutron scattering only probes correlations between the components of magnetic moments perpendicular to the wave-vector of the scattered neutron, and that this arrises from the form of the Fourier transformed interaction between the magnetic moment of the neutron and the magnetic field created by the motion of the electrons in the sample. We also examined the relationship between the quasi-elastic neutron scattering cross-section and the wave-vector dependent susceptibility $\chi(\mathbf{q})$. This relationship will be very important in Chapter 4 where we will use it in combination with the random phase approximation method of computing $\chi(\mathbf{q})$ to compute the quasi-elastic neutron scattering from our model Hamiltonian. This will allow us to compare the quasi-elastic neutron scattering cross-section generated by our model to that found in experiment in order to determine the strengths of the symmetry allowed bilinear exchange terms in our interaction model.

Chapter 4

Determining the Magnetic Interactions in $Yb_2Ti_2O_7$ from Paramagnetic Quasi-elastic Neutron Scattering

This chapter focuses on the method used to determine the form of the magnetic interactions in the material $Yb_2Ti_2O_7$ from quasi-elastic neutron scattering measurements made at $T = 1.4$ K on single crystal samples [31]. Specifically, we wish to determine the strengths of the four symmetry allowed bilinear exchange terms defined in Chapter 2. The quasi-elastic neutron scattering data, which was discussed in Chapter 1.6 was collected by Prof. Henrik Rønnow and Dr. Louis-Pierre Regnault. These measurements reveal the presence of anisotropic correlations in $Yb_2Ti_2O_7$ at $T = 1.4$ K via the presence of rod-like features in the data along $\langle 111 \rangle$ symmetry related directions. In a completely non-interacting system no such correlations would be present, as it is the magnetic interactions that give rise to these correlations. Because the interactions give rise to the correlations, the form of these correlations should be directly related to the nature of the magnetic interactions in $Yb_2Ti_2O_7$, and it should be possible to extract the form of the magnetic interactions in $Yb_2Ti_2O_7$ by fitting the quasi-elastic neutron scattering. We choose to use the data collected at $T = 1.4$ K rather than the data collected at $T = 9.1$ K as the signal to noise ratio of this data is higher. In principal the $T = 9.1$ K data would have better suited our purposed, as at this temperature $Yb_2Ti_2O_7$ is situated much more firmly in the paramagnetic phase, avoiding any potential problems with $Yb_2Ti_2O_7$ being in a collective paramagnetic phase, and correlation effects that appear due to the presence of a nearby phase transition.

4.1 Simulated Annealing

In this section we explain the method by which the form of the magnetic interactions is extracted from the quasi-elastic neutron scattering of Prof. Rønnow shown in Chapter 1.6. Initial attempts to fit the experimental neutron scattering using the model of symmetry allowed nearest-neighbour bilinear exchange were rather haphazard, involving manual manipulation of the parameters $\{\mathcal{J}_n\}$ in an attempt to generate a neutron scattering pattern using the RPA method similar to that seen in experiment. After many unsuccessful attempts at manual fitting, numerical optimization was decided upon as the best method to determine if it was indeed possible to fit the experimental neutron scattering using the proposed model Hamiltonian (Eq. (C.15)).

The numerical optimization method chosen to determine the values $\{\mathcal{J}_n\}$ is simulated annealing. This method is closely related to the physical thermodynamic process of annealing, which is the process of slowly cooling a system in order to allow the system to enter its absolute ground state rather than becoming trapped in a local energy minimum. This arises in the growth of single crystal material samples. If a molten sample of some material that forms a crystal at low temperatures is cooled rapidly, it will form a disordered polycrystalline sample when it solidifies. On the other hand if the sample is cooled slowly it maintains equilibrium during the process and is able to locate its lowest energy state forming large crystals.

4.1.1 The Metropolis Algorithm

Reference [48] presents an explanation of the simulated annealing method. The basis for simulated annealing is the Boltzmann probability distribution for a system in thermal equilibrium [48], which is given by

$$P(E) \sim \exp\left(-E/\left(k_{\mathrm{B}}T\right)\right), \tag{4.1}$$

where $P(E)$ is the probability of a system being in a state with energy E, $k_{\mathrm{B}} = 1.3806504 \times 10^{-23}$ J/K is the Boltzmann constant, and T is the temperature. This distribution expresses the fact that even at very low temperatures there is a finite but small probability for the system to be in a high energy state [48]. This means that there exists a corresponding chance of escaping a local energy minimum in order to find a "better" more global minimum via a multistep process involving a high energy state [48]. The Metropolis algorithm [49] provides a way for this principle to be applied to numerical simulations. This algorithm is

based on the proposition that if the system is in a state with energy E_1, the probability of it transitioning to a state with energy E_2 is given by [48]

$$p = \exp\left(-\left(E_2 - E_1\right)/k_{\mathrm{B}}T\right). \tag{4.2}$$

It can be seen that if $E_2 < E_1$, this probability will be greater than 1. In this case, the probability of the transition is simply set to 1 and the system transitions to the state with energy E_2. In the case where the probability is less than 1, a pseudo-random number generator (PSRNG) is used to generate a number in the range $(0, 1)$, if the generated number is less than p, the transition is allowed.

4.1.2 The Effective Energy Function and Implementation of the Metropolis Algorithm

For the determination of $\{\mathcal{J}_n\}$ for $Yb_2Ti_2O_7$, the energy function used is in Eqn. (4.1) is given by

$$E_{\mathrm{eff}} = \sum_{\mathbf{Q}} \left((c_0 S(\mathbf{Q}) + c_1 + c_2|\mathbf{Q}|) - S_{\mathrm{exp}}\left(\mathbf{Q}\right) - \overline{\Delta S} \right)^2 + \Lambda \left(\theta_{\mathrm{CW}}^{\mathrm{model}} - \theta_{\mathrm{CW}} \right)^2, \tag{4.3}$$

where $S(\mathbf{Q})$ is the RPA neutron scattering intensity given by Eqn. (3.49) for a specific value of $\mathbf{Q}$. $S_{\mathrm{exp}}\left(\mathbf{Q}\right)$ is the experimental neutron scattering intensity at the same point in reciprocal space and

$$\overline{\Delta S} = \mathrm{mean}\left((c_0 S(\mathbf{Q}) + c_1 + c_2|\mathbf{Q}|) - S_{\mathrm{exp}}\left(\mathbf{Q}\right) \right). \tag{4.4}$$

The scaling factors c_0, c_1, and c_2 are used to relate the model neutron scattering intensity, which is computed in arbitrary units, to the experimental neutron scattering intensity, which is recorded in terms of number of neutrons counted. The $|\mathbf{Q}|$ term was found to be important when comparing model and experimental neutron scattering cross sections in Ref. [50]. The specific points in reciprocal space used in the sum over $\mathbf{Q}$ are marked by the red lines in Fig. 4.1

$\theta_{\mathrm{CW}}^{\mathrm{model}}$ is the Curie-Weiss temperature of the model Hamiltonian, obtained by fitting a straight line to the inverse powder susceptibility, χ, computed at $T = 2.5$ K and $T = 10$ K, the same temperatures used in experimental fits [20]. The value of θ_{CW} used in Eqn. (4.3) is that of Ref. [20], $\theta_{\mathrm{CW}} = 0.75$ K. The powder susceptibility is given by

$$\chi = \frac{1}{3} Tr \left(\frac{1}{4} \sum_{ab} \chi_{ab}^{uv}(\mathbf{q} = \mathbf{0}, \omega = 0) \right). \tag{4.5}$$

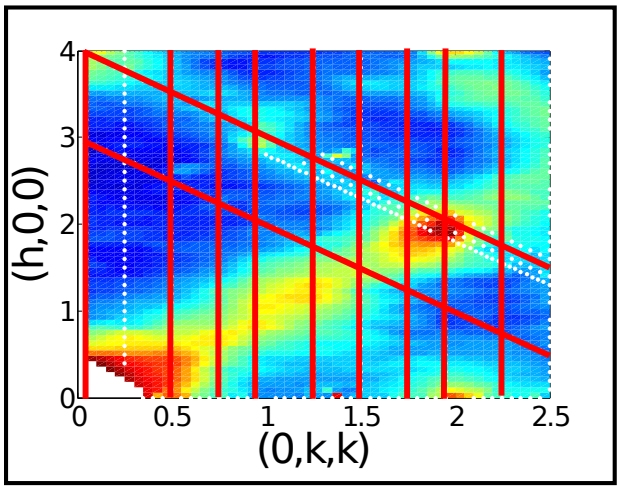

Figure 4.1: The quasi-elastic neutron scattering data at $T = 1.4$ K used to determine the form of the magnetic interactions in $Yb_2Ti_2O_7$, with the cuts of the (h, k, k) plane used in the simulated annealing fit marked in red.

In this equation the sum over sublattices a and b, and the trace of the resulting 3×3 matrix represent taking the powder average of the susceptibility, consistent with what was done in experiment. The sum over a and b of $\chi^{uv}_{ab}(\mathbf{q} = \mathbf{0}, \omega = 0)$ yields 4 times the single crystal susceptibility, which is diagonal. Taking the trace of this result and dividing by 3 results in the average of the susceptibility in all of the global cartesian coordinates, which is what is recorded in powder susceptibility measurements because of the random orientations of the powder grains.The value of Λ was chosen ad hoc to be 100000, in order to give this term the same weight in the calculation of E_{eff} as the neutron scattering term.

The following procedure is used to determine the values of $\{\mathcal{J}_n\}$ and $\{c_n\} = \{c_0, c_1, c_2\}$ that, when used in the model of Eqn. (C.15) to compute the RPA neutron scattering, result in the best fit to the experimental quasi-elastic neutron scattering data. First, a random initial set of interaction energies $\{\mathcal{J}_n\}$ and scaling parameters $\{c_n\}$ are chosen, along with a beginning effective temperature T_{eff} to start the process. We then proceed as follows:

1. Choose a parameter P from $\{\mathcal{J}_n\}$ or $\{c_n\}$ at random using a PSRNG.

2. Using a PSRNG once again, generate a random value in the range $(-1, 1)$. Multiply this value by the maximum allowed step size for P and add this value to P to form P_{new}.

3. Compute E_{eff} using P and P_{new}, yielding the values $E_{\text{eff}}^{\text{init}}$ and $E_{\text{eff}}^{\text{fin}}$.

4. Using $E_{\text{eff}}^{\text{init}}$ and $E_{\text{eff}}^{\text{fin}}$, compute $p = \exp\left(\left(E_{\text{eff}}^{\text{fin}} - E_{\text{eff}}^{\text{init}}\right)/T_{\text{eff}}\right)$.

5. If $p > 1$ set $P = P_{\text{new}}$. If not, generate a random number z in the range $(0, 1)$, if $z < p$, set $P = P_{\text{new}}$, otherwise do nothing.

6. Return to step 1.

This process is repeated 4000 times for a given T_{eff}, at which point T_{eff} is lowered to $T_{\text{eff}}/(1+\kappa)$, a process that is performed 100 times, leading to 400000 Monte Carlo steps in total. This part of the process is known as the annealing schedule [48].

This process will not yield the absolute minimum E_{eff}, and thus the optimal values of $\{\mathcal{J}_n\}$ and $\{c_n\}$, using one single annealing run, even if massive numbers of Monte Carlo steps and a very slow annealing schedule are used. To account for this, the code was run 100 times in parallel using different random seeds for the PSRNG, to obtain a distribution of results. The results of this process are discussed in the next section.

4.1.3 The Curie-Weiss Temperature Constraint and Additional Refinement of Simulated Annealing Results

As discussed in Chapter 4.1.2, the second term of Eqn. (4.3) is proportional to the difference between the experimental Curie-Weiss temperature for $Yb_2Ti_2O_7$, $\theta_{\text{CW}} = 0.75$ K [20], and the Curie-Weiss temperature of the model Hamiltonian, $\theta_{\text{CW}}^{\text{model}}$. This constraint is included in order to impose the correct energy scale on the interactions determined using the simulated annealing fit to the experimental quasi-elastic neutron scattering data, because this energy scale is directly related to θ_{CW}.

θ_{CW} in Ref. [20] is determined by fitting a straight line to experimental measurements of the inverse powder magnetic susceptibility at temperatures between $T = 2.5$ K and $T = 10$ K. The temperature axis intercept of this line is θ_{CW}. $\theta_{\text{CW}}^{\text{model}}$ is determined by fitting a straight line to the inverse susceptibility calculated at $T = 2.5$ K and $T = 10$ K. This simple fit was chosen in order to make the process of determining $\theta_{\text{CW}}^{\text{model}}$ simple and computationally efficient in order to make the calculations run quickly. If computational efficiency had not been an issue, a more ideal way to compute $\theta_{\text{CW}}^{\text{model}}$ would have been to compute χ_{mod}^{-1}, the inverse susceptibility of our magnetic interaction model at the same points at which χ_{exp}^{-1}, the experimental inverse magnetic susceptibility, was measured.

If this method had been used, then we could have replaced the soft constraint imposed on $\theta_{\rm CW}^{\rm model}$ via the second term in Eqn. (4.3), $E_2 = \Lambda \left(\theta_{\rm CW}^{\rm model} - \theta_{\rm CW}\right)^2$, with a functionally equivalent term

$$E_2' = \Lambda \sum_i \left(\chi_{{\rm exp},i}^{-1} - \chi_{{\rm mod},i}^{-1}\right)^2 . \tag{4.6}$$

In this new new term, $\chi_{{\rm exp},i}$ and $\chi_{{\rm mod},i}$ are the experimental and model values of the powder magnetic susceptibility at specific temperature points indexed by the label i. The sum over i indicates the sum over all of the temperatures at which the experimental powder susceptibility is available. As the number of points i in E_2' increases, $P(E_{\rm eff})$, which contains the terms $\exp\left(-E_2'/T\right)$ will look more and more like a delta function,

$$\delta\left(\{\chi_{{\rm exp},i}^{-1}\}, \{\chi_{{\rm mod},i}^{-1}\}\right)$$

, where $\{\chi_{{\rm exp},i}^{-1}\}$ and $\{\chi_{{\rm mod},i}^{-1}\}$ are the sets of all the points for which $\chi_{\rm exp}$ and $\chi_{\rm mod}$ are available. This delta function is equivalent to the delta function $\delta\left(\theta_{\rm CW}, \theta_{\rm CW}^{\rm model}\right)$, because the inverse powder susceptibility and $\theta_{\rm CW}$ are directly related. As the fit between $\{\chi_{{\rm exp},i}^{-1}\}$ and $\{\chi_{{\rm mod},i}^{-1}\}$ is further and further constrained by the increasing number of points, so is the fit between $\theta_{\rm CW}$ and $\theta_{\rm CW}^{\rm model}$.

This discussion of using a constraint based directly on the inverse powder susceptibility rather than on $\theta_{\rm CW}$ is directly related to the issue of filtering the results of our simulated annealing method. This filtering is required because the simulated annealing fit process will result in a large cloud of points in $\{\mathcal{J}_n\}$ space, not all of which are actually models that fit the experimental neutron scattering pattern or $\theta_{\rm CW}$. This poor fitting occurs because the constraints on $\theta_{\rm CW}^{\rm model}$ and $S(\mathbf{Q})$ are soft constraints, meaning that these values are allowed to vary in an attempt to minimize the global function $E_{\rm eff}$, and not fixed to the precise values found in experiment by a delta-function like constraint. Fig. 4.2 shows $S(\mathbf{Q})$ for two sets of couplings, $\{\mathcal{J}_n\}$, the results of two different simulated annealing runs. One of these sets of $\{\mathcal{J}_n\}$, matches $S(\mathbf{Q})_{\rm exp}$ and $\theta_{\rm CW} = 0.75$ K [20] well, while the other fits them poorly, with $\theta_{\rm CW}^{\rm model} = 0.78$ K. Such poorly fitting $\{\mathcal{J}_n\}$ were eliminated from further consideraction, with any result where $\theta_{\rm CW}^{\rm model}$ varied from 0.75 K by more than 0.01 K being discarded. This stringent constraint is justified by the previously explained argument, whereby an improved method of fitting $\theta_{\rm CW}$, based on a fit to $\{\chi_{{\rm exp},i}^{-1}\}$, would result in a very stringent constraint on $\theta_{\rm CW}^{\rm model}$.

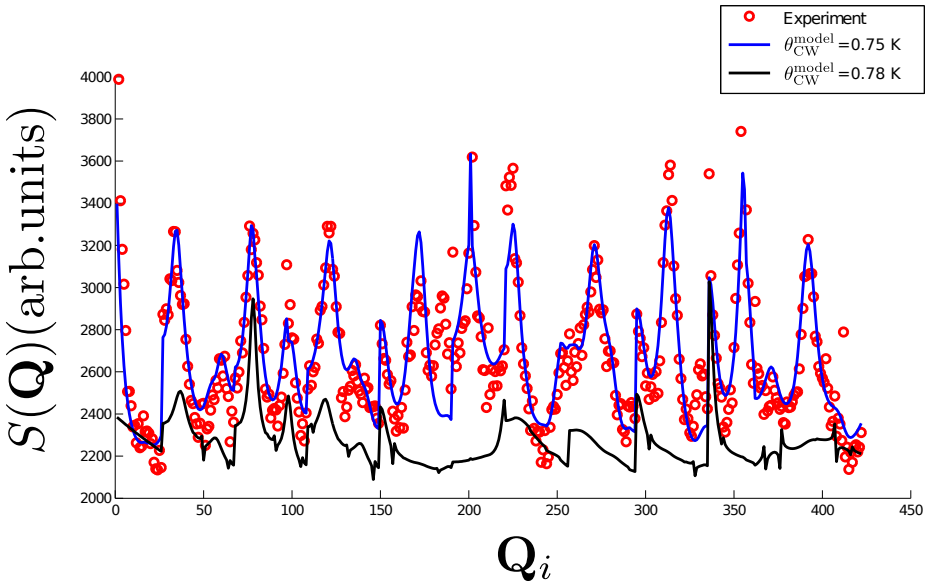

Figure 4.2: $S(\mathbf{Q})$ plotted for the sets of couplings, $\{\mathcal{J}_n\}$, resulting from two different simulated annealing runs. One set of $\{\mathcal{J}_n\}$ yields $\theta_{\rm CW}^{\rm model} = 0.78$ K, while the other yields $\theta_{\rm CW}^{\rm model} = 0.75$ K. It can be seen quite clearly that $S(\mathbf{Q})$ for the set of $\{\mathcal{J}_n\}$ with $\theta_{\rm CW}^{\rm model} = 0.75$ K fits the experimental data much better than the set of $\{\mathcal{J}_n\}$ with $\theta_{\rm CW}^{\rm model} = 0.78$ K. $\mathbf{Q}_i$ denotes all of the points in the sum over $\mathbf{Q}$ in Eqn. (4.3) appended into a single set, as they would be stored in our simulated annealing program.

4.2 Results

We now present the results of simulated annealing fits to the quasi-elastic neutron scattering data collected by Prof. Rønnow [31], discussed in Chapter 1.6. Simulated annealing fits were performed using two slightly different models. These two models are differentiated by the CEF parameterization used to compute the single ion susceptibility in Eqn. (3.55).

Each of the two sets of simulated annealing fits resulted in a cloud of points in $\{\mathcal{J}_n\}$ space. As previously discussed in Chapter 4.1.3, some of these points are not in fact good fits to the experimental neutron scattering data and/or the experimental value of $\theta_{\rm CW}$ used in the optimization, $\theta_{\rm CW} = 0.75$ K [20], due to the model becoming trapped in a local minimum of $E_{\rm eff}$. These poorly fitting points were discarded for both fits with any result where ${\theta_{\rm CW}}^{\rm model}$ varied from 0.75 K by more than 0.01 K being discarded. The resulting points are displayed in $\{\mathcal{J}_n\}$ space for both the CEF of Hodges *et al.* [20] and Cao *et al.*

[19] in Fig. 4.3. As can be seen, both CEF parameterizations result in tight clusters in $\{\mathcal{J}_n\}$ space. The average values of these clusters are marked by the crossing points of the three red lines (in $\mathcal{J}_1$, $\mathcal{J}_2$, $\mathcal{J}_3$). The exact values of these points for both CEF parameterization used are reported in Table 4.1 along with uncertainties of 1 standard deviation.

Table 4.1: Average values of the coupling parameters $\{\mathcal{J}_n\}$ resulting from simulated annealing. The indicated uncertainties correspond to one standard deviation.

CEF Parameterization	$\mathcal{J}_1$	$\mathcal{J}_2$	$\mathcal{J}_3$	$\mathcal{J}_4$
Hodges *et al.* [20]	0.100 ± 0.005 K	0.202 ± 0.003 K	0.166 ± 0.006 K	0.001 ± 0.004 K
Cao *et al.* [19]	0.061 ± 0.003 K	0.171 ± 0.002 K	0.139 ± 0.004 K	0.001 ± 0.003 K

Using the relationship between $\{\mathcal{J}_e\} = \{\mathcal{J}_{\text{Ising}}, \mathcal{J}_{\text{iso}}, \mathcal{J}_{\text{pd}}, \mathcal{J}_{\text{DM}}\}$, and$\{\mathcal{J}_n\}$, discussed in Chapter 2.2.2 and Appendix C.2, we can rewrite the coupling values of Table 4.1 in terms of $\{\mathcal{J}_e\}$, obtaining the results in Table 4.2. This notation will be used from now on.

If we examine the coupling values of $\{\mathcal{J}_e\}$ we can see that the largest term in both sets of $\{\mathcal{J}_e\}$ is the local Ising term $\mathcal{J}_{\text{Ising}}$, which is very interesting as it is in direct opposition to the planar nature of the ground state doublet of the both CEF parameterizations. The other three couplings are similar in magnitude, being approximately one quarter of the value of $\mathcal{J}_{\text{Ising}}$. It is interesting to note that the negative sign of $\mathcal{J}_{\text{pd}}$ in Tables 4.2 and 4.3, would correspond to physical, as opposed to unphysical, dipolar interactions, if this interaction were the long-range magnetic dipolar interaction. Finally it is interesting that $\mathcal{J}_{\text{DM}}$ is on the order of the other couplings. The DM interaction arises as a perturbative term due to spin orbit coupling in magnetic materials [51] and because it arrises due to perturbation theory, it is expected to be quite small. Recent work by Onoda *et al.* [52, 53] has shown that is indeed possible for values of the DM coupling on the order of those found here to exist in the case of $Yb_2Ti_2O_7$. This work is discussed further in Appendix H.

The black dots in Fig. 4.3 mark chosen values for direct comparison of the model results to experiment, and whose specific values of $\{\mathcal{J}_e\}$ are given in Table 4.3. Exact rather than average values are used as precise scaling parameters $\{c_n\}$ are required for comparison between model and experiment (reported in Table 4.4), and averaging these would lead to a poor fit. The scattering in the (h, k, k) plane generated by the two models in Table 4.3 are shown in Fig. 4.4(a,b). Examining the RPA scattering for both models it can be seen that they successfully reproduce most of the features of interest in the experimental data shown in Fig. 4.4(d), including the $[1, 1, 1]$ rod of scattering, the rod-like feature between $(2, 2, 2)$

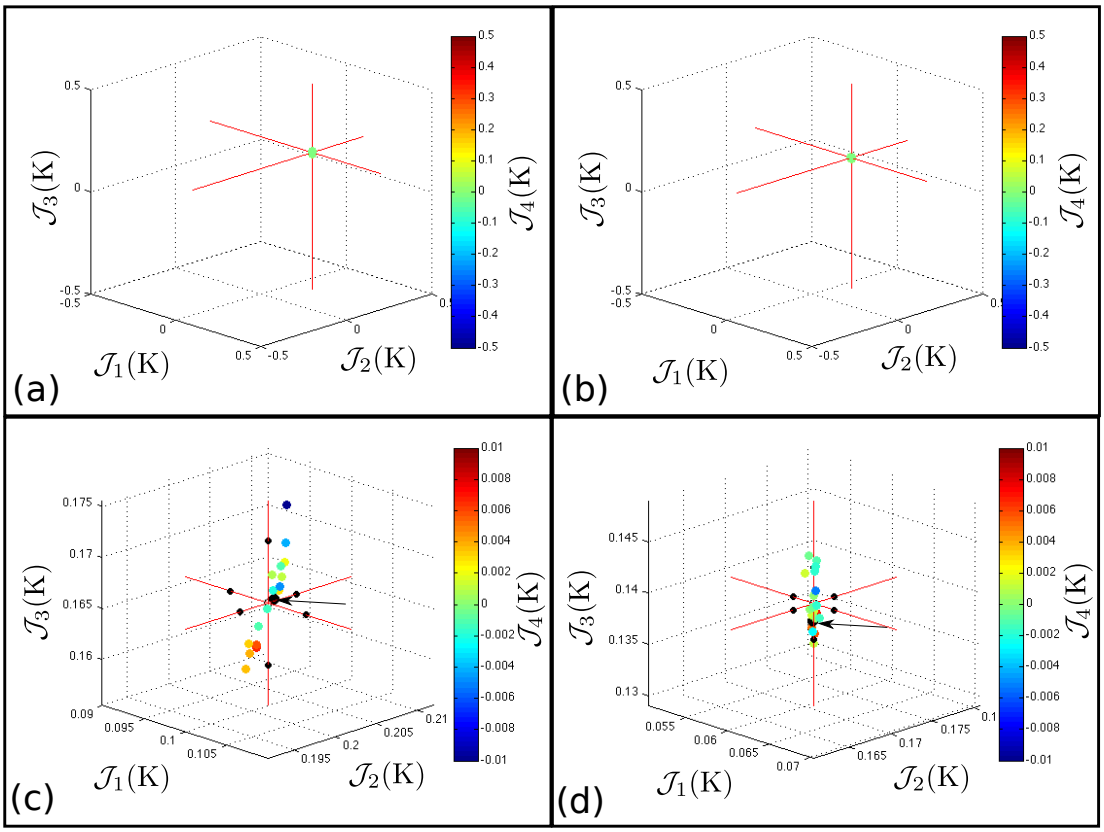

Figure 4.3: The refined results of simulated annealing optimization for the CEF parameterizations of (a,c) Hodges *et al.* [20] and (b,d) Cao *et al.* [19]. It can be seen in (a) and (b) that the refined clusters are quite small in $\{\mathcal{J}_n\}$ space. The red lines illustrate the location of the average value of the cluster, given in Table 4.1. Panels (c) and (d) show closer views of the clusters. The red lines once again mark the average value of $\{\mathcal{J}_n\}$ for the cluster, with the small black dots showing one standard deviation in each of $\mathcal{J}_1$,$\mathcal{J}_2$, and $\mathcal{J}_3$. $\mathcal{J}_4$ is omitted from this treatment as it is shown on the colour scale and its range is small. The large black dots in panels (c) and (d), highlighted by arrows, indicate the simulated annealing results that have been selected for direct comparison to experiment.

Table 4.2: Average values of the coupling parameters $\{\mathcal{J}_e\}$ computed from the values of $\{\mathcal{J}_n\}$ in Table 4.1.

CEF Parameterization	$\mathcal{J}_{\text{Ising}}$	$\mathcal{J}_{\text{iso}}$	$\mathcal{J}_{\text{pd}}$	$\mathcal{J}_{\text{DM}}$
Hodges *et al.* [20]	0.80 ± 0.02 K	0.223 ± 0.003 K	-0.289 ± 0.009 K	-0.267 ± 0.009 K
Cao *et al.* [19]	0.75 ± 0.02 K	0.181 ± 0.002 K	-0.259 ± 0.006 K	-0.248 ± 0.006 K

and $(0, 0, 4)$, and the intensity around the point $(2, 2, 0)$. It is also interesting to note that neither model reproduces the feature centred around $(2.25, 2.24, 3.5)$. This means that the model has successfully postdicted the fact that this feature is not magnetic in origin, as discussed in Chapter 1.6. Figure 4.4(c) shows the result of attempting the reproduce the experimental data using only isotropic exchange ($\mathcal{J}_{\text{Ising}} = \mathcal{J}_{\text{pd}} = \mathcal{J}_{\text{DM}} = 0$), with strength $\mathcal{J}_{\text{iso}} = 0.06$ K, determined from a single parameter fit to match $\theta_{\text{CW}} = 0.75$ K [20, 31]. It can be seen quite clearly that this model fails to reproduce any of the features of interest in the experimental data.

Table 4.3: Selected values of $\{\mathcal{J}_e\}$ for comparison of model neutron scattering to experiment. These sets of $\{\mathcal{J}_e\}$ are taken from near the centre of the cluster of the results of simulated annealing optimization shown in Fig. 4.3. θ_{CW} for the models, computed using the method given in Chapter 4.1 is also shown.

CEF Parameterization	$\mathcal{J}_{\text{Ising}}$	$\mathcal{J}_{\text{iso}}$	$\mathcal{J}_{\text{pd}}$	$\mathcal{J}_{\text{DM}}$	$\theta_{\text{CW model}}$
Hodges *et al.* [20]	0.808767 K	0.0.223796 K	-0.289994 K	-0.267714 K	0.750093 K
Cao *et al.* [19]	0.755082 K	0.180150 K	-0.258359 K	-0.247568 K	0.753445 K

Figure 4.5 shows a quantitative comparison of experimental and model neutron scattering data at $T = 1.4$ K for both models in Table 4.3 and the simple isotropic exchange model. This comparison allows us to see that both models are not only excellent qualitative fits to the experimental neutron scattering pattern, as seen in Fig. 4.4, but are also excellent quantitative fits to experimental neutron scattering intensities. This is in contrast to the isotropic exchange model, which is confirmed to be a very poor fit to experiment despite separate annealing to determine the best possible set of coupling parameters $\{c_n\}$ for this model. This poor fit occurs despite this separate annealing because the neutron scattering pattern of the isotropic exchange model is so fundamentally different from that

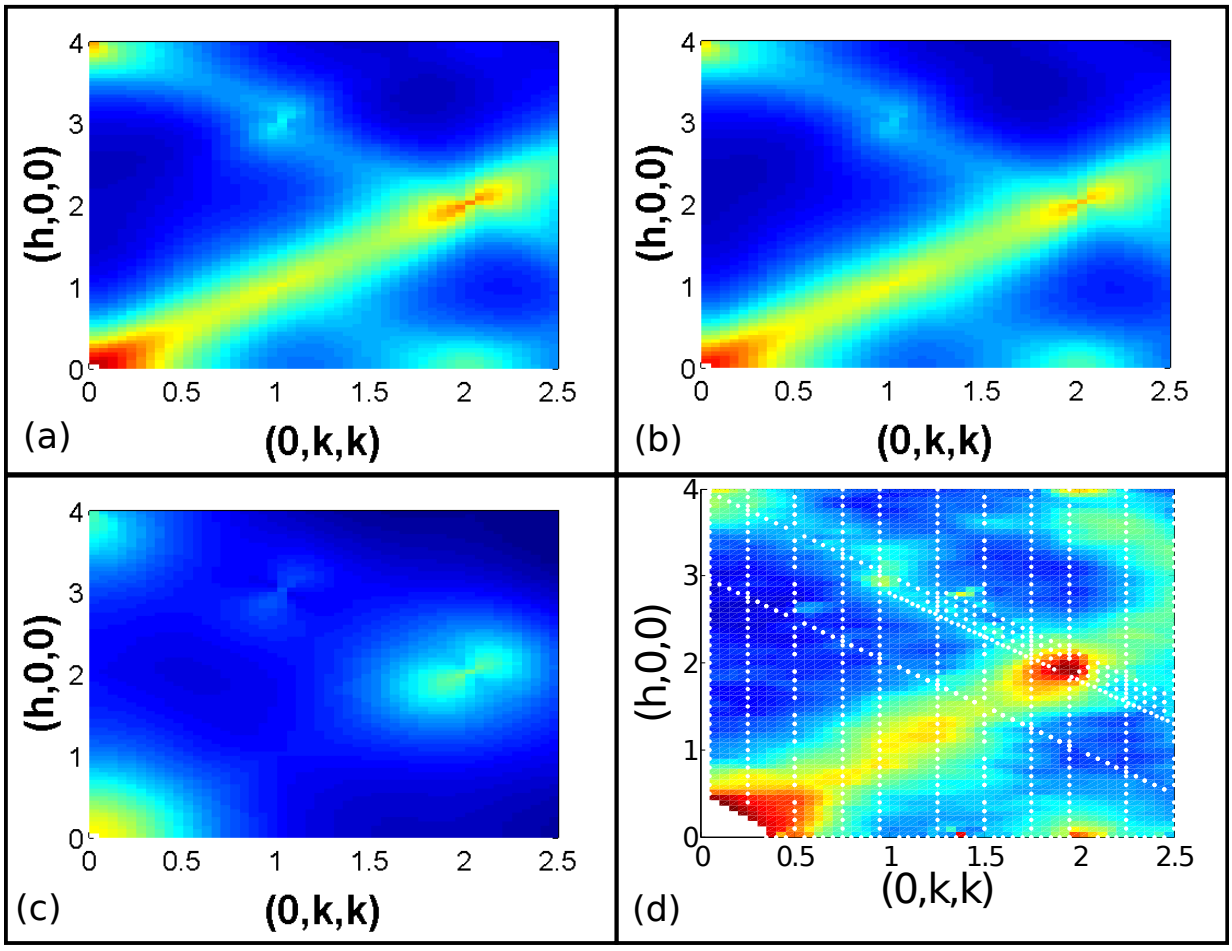

Figure 4.4: Quasi-elastic neutron scattering computed at $T = 1.4$ K for the models in Table 4.3. Panel (a) shows the neutron scattering for the coupling parameters obtained using the CEF of Hodges *et al.* [20]. Panel (b) shows the neutron scattering for the coupling parameters obtained using the CEF of Cao *et al.* [19]. Panel (c) shows the neutron scattering generated by a model using only isotropic exchange ($\mathcal{J}_{\text{iso}} = 0.06$ K) and long-range dipolar interactions. Panel (d) shows the experimentally obtained quasi-elastic neutron scattering at $T = 1.4$ K of Ref. [31] for comparison.

of experiment that even the optimal combination of $\{c_n\}$ that minimizes E_{eff} results in a poor fit to experiment. Fig. 4.5a does appear to show a good fit between the neutron scattering of the isotropic exchange model and experiment. This occurs because the cut along $(h, 0.05, 0.05)$ in reciprocal space passes through a region of the neutron scattering pattern where there are no magnetic features, and only background noise, in both experiment and the scattering of the isotropic exchange model. This means that the data in Fig. 4.5(a)a does not actually represent any kind of agreement between the isotropic exchange model and experiment, it only shows that we can match the background noise level.

Table 4.4: Values of the scaling parameters $\{c_n\}$ for the two sets of couplings $\{\mathcal{J}_e\}$ reported in Table 4.3 that are required for quantitative comparison of RPA neutron scattering calculations to experiment.

CEF Parameterization	c_0	c_1	c_2
Hodges *et al.* [20]	38.625395	1700	13.406493
Cao *et al.* [19]	39.181870	1700	20.618574

The result of all of these comparisons is that we have two potential models, one for each of the CEF parameterizations used that are capable of explaining the features seen in the experimental paramagnetic quasi-elastic neutron scattering data.

Now we must place some constraints on our results. These constraints arise from the use of the RPA, specifically the assumptions about the energy resolution. More rigorous calculations of $d\sigma/d\Omega(\mathbf{q})$ using $\chi(\mathbf{q}, \omega)$ and then integrating over a finite range of $d\omega$ were performed by Dr. Paul McClarty. These calculations [31] found very similar, but not quantitatively identical, scattering patterns in the (h, k, k) plane to those in Fig. 4.4(a,b). This indicates that some small changes in $\{\mathcal{J}_e\}$ would be evident if the simulated annealing fit were to be performed using exact integration over the same energy range measured by the detectors in the experiment. In addition to this, when using the RPA to perform calculations it is important to consider the possible presence of correlations due to the proximity of a phase transition and not just magnetic interactions. Our calculations were performed at $T = 1.4$ K, which as previously discussed, and noted in Ref. [31], is approximately five to six times the reported temperature of the phase transition in $Yb_2Ti_2O_7$, $T_c \approx 214$ mK [16], and twice the experimentally reported value of $\theta_{\text{CW}} = 0.75 \pm 0.05$ K [18, 20]. Given this proximity to the observed phase transition some correlation effects, due to the divergence of the correlation length near the phase transition, are to be expected. If the effects of these correlations related to the phase transition were to be accounted for, some change in the

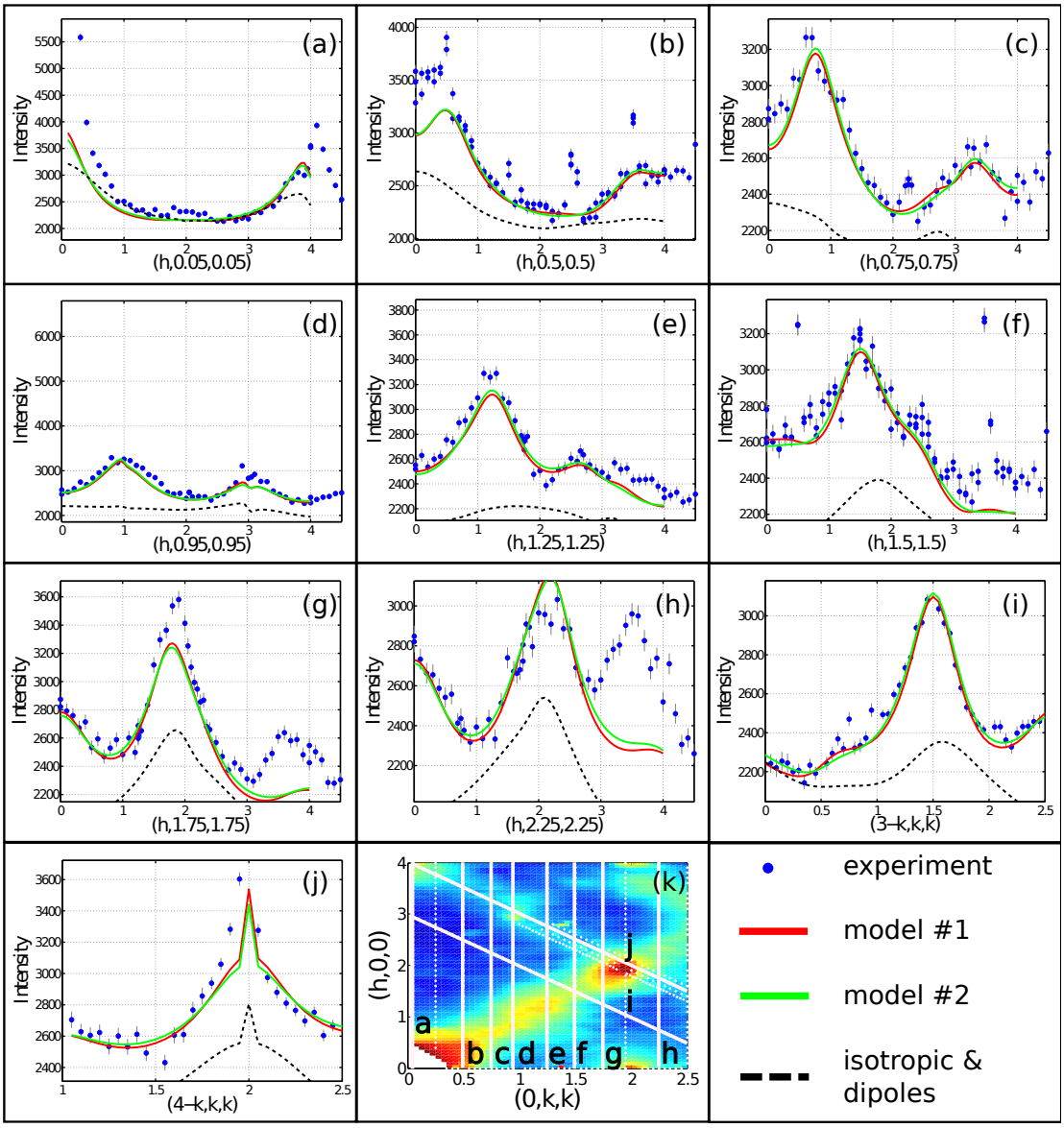

Figure 4.5: Panels (a) through (j) show cuts through the (h, k, k) plane in reciprocal space. The blue dots show the experimental paramagnetic quasi-elastic neutron scattering at $T = 1.4$ K. The solid red lines show the results of RPA calculations of the quasi-elastic neutron scattering at $T = 1.4$ K using the set of couplings $\{\mathcal{J}_e\}$ shown in Table 4.3 for the CEF parameterization of Hodges *et al.* [20] (model #1). The solid green lines show the same calculation, but using $\{\mathcal{J}_e\}$ obtain using the CEF parameterization of Cao *et al.* [19] (model #2). The black dashed line shows the result of RPA calculations using only isotropic exchange ($\mathcal{J}_{\rm iso} = 0.06$ K) discussed in the text. Panel (k) shows a map of the (h, k, k) plane, indicating the positions of all of the cuts in panels (a) through (j).

values of $\{\mathcal{J}_e\}$ determined using the current method would be expected, possibly on the order of $1/\left(T-\theta_{\rm CW}\right)^2 \sim 25\%$, the leading correction to the high temperature expansion of $\chi(\mathbf{q})$ [31]. Despite these constraints, the RPA calculation of $d\sigma/d\Omega(\mathbf{q})$ will generate a unique scattering pattern in the (h,k,k) plane for a given set of couplings $\{\mathcal{J}_e\}$, so the variation of the couplings when these constraints are taken into account should be on the order of one [31]. The overall energy scale of the couplings $\{\mathcal{J}_e\}$ also cannot change drastically due to the imposition during the simulated annealing fit that $\theta_{\rm CW}^{\rm model}$ must match that found in experiment, placing a constraint on the energy scales of the interactions. The net result of these constraints and the assumption of bilinear exchange discussed earlier is that the Hamiltonian we find to describe the magnetic interactions in $Yb_2Ti_2O_7$ will capture the important elements of the low temperature physics of $Yb_2Ti_2O_7$. It will not capture the physics of $Yb_2Ti_2O_7$ at large energies, on the order of the CEF splitting.

RPA calculations can also provide us with other interesting properties of our model Hamiltonian; those being the RPA transition temperature $T_{\rm RPA}$ and the ordering wave-vector. $T_{\rm RPA}$ is determined by lowering the temperature at which the neutron scattering is computed until the scattering cross section becomes negative for some point in $\mathbf{q}$ space. The temperature at which this occurs will be directly proportional to the largest eigenvalue of $\overline{\overline{\mathcal{J}}}\left(\mathbf{q}\right)$ anywhere inside the first Brillouin zone. The mean field ordering wave-vector is the point $\mathbf{q}$ at which the largest eigenvalue occurs [2]. By searching over the first Brillouin zone, we find that both models yield $\mathbf{q}=0$ order, with values of $T_{\rm RPA} \sim 1.17$ K.

[2] The mean field free energy of a system, $F\left(\{\mathbf{m}_i^a\}\right)$, is a function of $\{\mathbf{m}_i^a\}$, the set of all of the vector order parameters $\mathbf{m}_i^a$ for all of the sites on the pyrochlore lattice [54, 55]. If we then Fourier transform the free energy into momentum space, it takes the from $F\left(\{\mathbf{m}^a\left(\mathbf{q}\right)\}\right)$, where $\{\mathbf{m}^a\left(\mathbf{q}\right)\}$ are the Fourier transformed order parameters. Then, in order to diagonalize the Fourier transformed interaction matrix $\overline{\overline{\mathcal{K}}}^{ab}\left(\mathbf{q}\right)$, $\{\mathbf{m}^a\left(\mathbf{q}\right)\}$ must be transformed into normal mode variables, whose amplitude are denoted $\phi_{\mathbf{q}}^{\alpha}\mu$, where α and μ label the normal modes [54]. The quadratic term in the free energy expressed in terms of these normal mode amplitudes (Eqn. 10 in Ref. [54]) is given by $\frac{1}{2}\sum_{\mathbf{q},\alpha,\mu}\left[nT-\lambda_{\mu}^{\alpha}\left(\mathbf{q}\right)\right]\left|\phi_{\mathbf{q}}^{\alpha}\mu\right|^2$, where n is the dimension of the spin ($n=3$ for Heisenberg spins), T is the temperature, and $\lambda_{\mu}^{\alpha}\left(\mathbf{q}\right)$ are the eigenvalues of the Fourier transformed interaction matrix. From this result it can be seen that if the coefficient of one of the normal mode amplitudes becomes negative, the value of the normal mode amplitude which minimizes $F\left(\{\mathbf{m}^a\left(\mathbf{q}\right)\}\right)$ will become non-zero, and the system will order. The highest temperature at which the coefficient for one of the normal mode amplitudes becomes negative will correspond to the largest $\lambda_{\mu}^{\alpha}\left(\mathbf{q}\right)$ inside the first Brillouin zone, and the mean field ordering wave-vector is the wave-vector $\mathbf{q}$ at which this eigenvalue achieves its maximum value.

4.3 Summary

In this chapter we have used fits to experimental quasi-elastic neutron scattering patterns to determine the strength of the four symmetry allowed bilinear exchange terms in our model of the magnetic interactions in$Yb_2Ti_2O_7$. Quasi-elastic neutron scattering is used to determine the form of the interactions because it is directly related to the interaction driven correlations between the magnetic moments in $Yb_2Ti_2O_7$. In order to compute the quasi-elastic neutron scattering from our proposed model, we use the random phase approximation (RPA) and compared RPA neutron scattering and experiment using a simulated annealing process to determine optimal strengths of the various bilinear exchange terms. The results of this simulated annealing show that a model containing anisotropic nearest-neighbour bilinear exchange and long-range magnetic dipolar interactions can successfully reproduce the important features seen in the experimental quasi-elastic neutron scattering. The model that we obtain consists of nearest-neighbour local Ising exchange, nearest-neighbour isotropic exchange, nearest-neighbour pseudo-dipolar exchange, and Dzyaloshinskii-Moriya exchange. We find that nearest-neighbour local Ising exchange is the strongest term in our model for $Yb_2Ti_2O_7$, being approximately four times the strength of the other three exchange terms. We also find that Dzyaloshinskii-Moriya exchange is abnormally large in our model.

Chapter 5

Real Space Correlations

In Ref. [40] it was proposed that the rod-like features in the paramagnetic quasi-elastic neutron scattering discussed in the previous chapter arise from two-dimensional correlations within the kagome planes that make up the pyrochlore lattice. This is because neutron scattering is a probe magnetic correlations between the elements of the magnetic moments $\mathbf{J}$ perpendicular to the scattering wave-vector $\mathbf{Q}$. If we have a system with magnetic correlations in some direction $\hat{\mathbf{r}}$, with characteristic length γ, then the neutron scattering cross section in a direction $\hat{\mathbf{Q}} \parallel \hat{\mathbf{r}}$ will exhibit a peak around $\mathbf{Q} = 2\pi/\gamma$, as shown in Fig. 5.1(a). If there are no correlations along a given $\mathbf{Q}$, the neutron scattering along that direction in reciprocal space will consist only of background scattering, as shown in Fig. 5.1(b). If correlations exist in two dimensions, but not in a third, these two types of scattering will be superimposed, as shown in Fig. 5.1, resulting in a rod of scattering in reciprocal space.

Now that we have determined two sets of magnetic interactions for $Yb_2Ti_2O_7$ that successfully reproduce the neutron scattering pattern seen in experiment, we can test whether this pattern does in fact arise from two-dimensional correlations as suggested in Ref. [40], by actually computing the spin-spin correlation function along several high symmetry directions of the pyrochlore lattice within the random phase approximation (RPA).

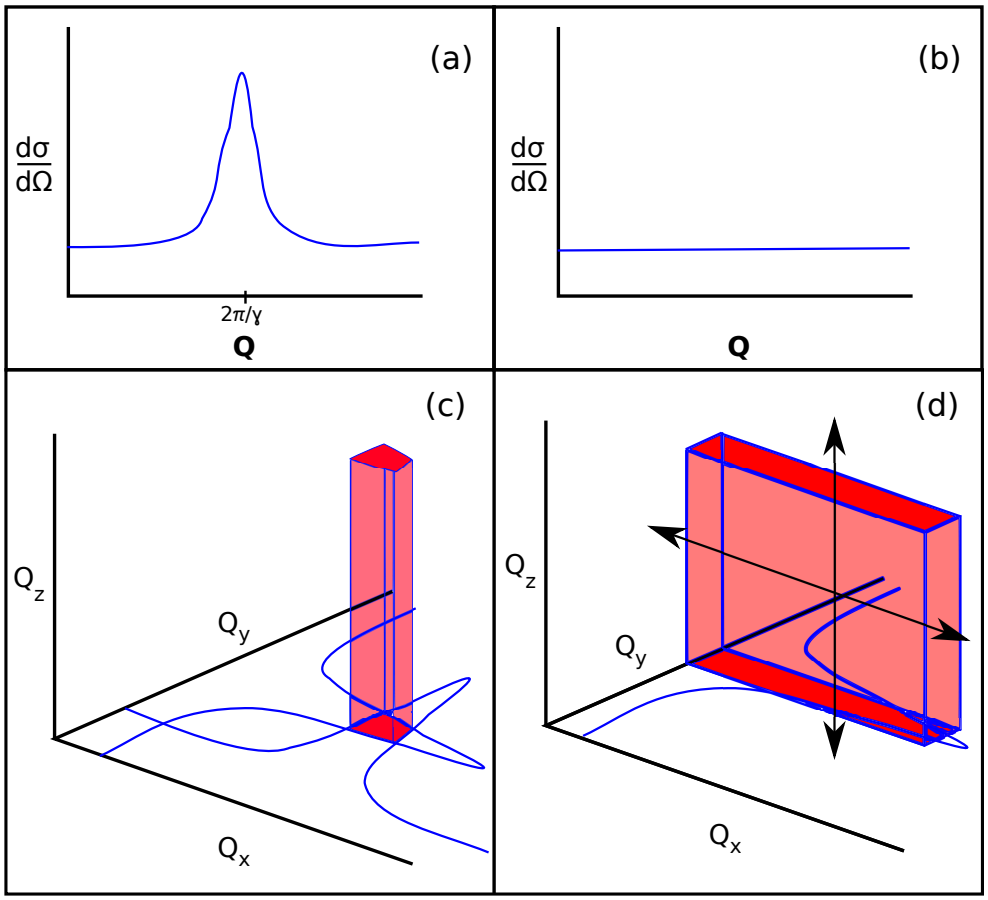

Figure 5.1: Panel (a) shows the neutron scattering intensity along $\mathbf{Q}$ in reciprocal space, arising from real space magnetic correlations along $\hat{\mathbf{r}} \parallel \hat{\mathbf{Q}}$, with characteristic length γ. Panel (b) shows the neutron scattering intensity when there are no such correlations. Panel (c) shows the rod of neutron scattering intensity in $3D$ reciprocal space that arises from the superposition of correlations in two directions, i.e. two-dimensional correlations. Panel (d) shows the plane of neutron scattering intensity in $3D$ reciprocal space that arises from correlations in one direction in reciprocal space, with the black arrows showing the directions in which the plane extends.

5.1 Computing the Real Space Correlation Function in the Random Phase Approximation

In order to compute the real space correlations, we return to the RPA. We saw in Chapter 3 that there is a direct relationship between the wave-vector dependent susceptibility and the correlation function $\langle J_i^{a,u} J_j^{b,v} \rangle$. This means that it is possible to extract the real space correlation function $\langle J_i^{a,u} J_j^{b,v} \rangle$ from the RPA susceptibility. The specific relationship required for this calculation can be shown in the following manner. We start from Eqn. (3.43)

$$\begin{aligned}
\chi_{a,b}^{u,v}(\mathbf{Q},0) &\propto \frac{1}{k_{\mathrm{B}}T}\left(\mathcal{S}_{ab}^{uv}(\mathbf{Q},0) - \mathcal{S}_{ab,\mathrm{Bragg}}^{uv}(\mathbf{Q},0)\right) \\
&\propto \frac{1}{k_{\mathrm{B}}T}\left(\sum_{i,j}\exp\left(i\mathbf{Q}\cdot\left(\mathbf{R}_i^a - \mathbf{R}_j^b\right)\right)\langle J_i^{a,u} J_j^{b,v}\rangle - \sum_{i,j}\exp\left(i\mathbf{Q}\cdot\left(\mathbf{R}_i^a - \mathbf{R}_j^b\right)\right)\langle J_i^{a,u}\rangle\langle J_j^{b,v}\rangle\right).
\end{aligned}$$

By taking the inverse Fourier transform of this equation, we obtain the result

$$\langle J_i^{a,u} J_j^{b,v}\rangle \propto \int_{\mathrm{BZ}} \exp\left(-i\mathbf{Q}\cdot\left(\mathbf{R}_i^a - \mathbf{R}_j^b\right)\right)\chi_{a,b}^{u,v}(\mathbf{Q},0)\,d\mathbf{Q}, \tag{5.1}$$

where the integral over $d\mathbf{Q}$ is taken over the first Brillouin zone of the FCC lattice. If we take one of the moments to be at the origin, by setting $i = 0$, $a = 1$, we can vary j and b to determine the $\mathbf{R}_{ij}^{ab}$ dependence of the real space correlations along different directions in real space. This integral is performed using Monte Carlo integration. We choose to compute two quantities using this method:

$$S(\mathbf{r}) = \int_{\mathrm{BZ}} \exp\left(-i\mathbf{Q}\cdot\left(\mathbf{R}_i^a - \mathbf{R}_j^b\right)\right)\chi_{a,b}^{u,u}(\mathbf{Q},0)\,d\mathbf{Q}, \tag{5.2}$$

which is proportional to $\langle \mathbf{J}_i^a \cdot \mathbf{J}_j^b \rangle$, and

$$S_{\perp}(\mathbf{r}) = \int_{\mathrm{BZ}} \exp\left(-i\mathbf{Q}\cdot\left(\mathbf{R}_i^a - \mathbf{R}_j^b\right)\right)\left(\delta_{u,v} - \hat{Q}_u\hat{Q}_v\right)\chi_{a,b}^{u,v}(\mathbf{Q},0)\,d\mathbf{Q}, \tag{5.3}$$

which is directly related to the inverse Fourier transform of the neutron scattering cross section. Now that we can compute the real space correlation functions from the wave-vector dependent susceptibility, it is a simple matter to use the RPA method of Chapter 3.3 to compute the wave-vector dependent susceptibility in the RPA and use this to compute the real space magnetic correlation functions.

5.2 Results

Using the set of anisotropic exchange couplings for the CEF parameterization of Hodges *et al.* from Table 4.3, we have computed the real space correlation functions $S(\mathbf{r})$ and $S_{\perp}(\mathbf{r})$ along three high symmetry directions of the pyrochlore lattice. We feel justified in computing these correlations using only one of the two models obtained in Chapter 3 as the scattering patterns generated by the two models are almost indistinguishable. As the scattering cross section is directly related to the magnetic correlations this means that the real space correlations generated by the two models should also be essentially indistinguishable. The three high symmetry directions are $[0\bar{1}1]$, a nearest-neighbour chain direction, $[1\bar{2}1]$, a second nearest-neighbour direction, and [111], a cubic unit cell body diagonal direction, perpendicular to one of the kagome planes in the pyrochlore lattice. As our model does not break any of the symmetries of the pyrochlore lattice, all symmetry equivalent nearest-neighbour chain directions, second nearest-neighbour directions, and $\langle 111 \rangle$ cubic body diagonal directions will display identical magnetic correlations. This means that we need only compute the real space correlations along one example of each of these high symmetry directions. This symmetry of the correlation function was checked by computing the real space correlation functions along various symmetry equivalent directions on the pyrochlore lattice, and it was found that the correlation functions behave identically along symmetry related directions. These high symmetry directions are shown in Fig. 5.2.

The results of our calculations, performed at $T = 1.4$ K are shown in Fig. 5.3. There, it can be seen that both correlations functions, $S(\mathbf{r})$ and $S_{\perp}(\mathbf{r})$, behave in similar manners as a function of distance. As the distance from the origin increases, the correlations functions decay in an exponential-like manner with the three directions splitting into two groups in terms of the strengths of the correlations. The strongest correlations are found along the nearest-neighbour chain direction $[0\bar{1}1]$, for both $S(\mathbf{r})$ and $S_{\perp}(\mathbf{r})$. Perhaps most interestingly, the correlation functions $S(\mathbf{r})$ and $S_{\perp}(\mathbf{r})$ have very similar values along the second nearest-neighbour direction $[1\bar{2}1]$ and cubic body diagonal direction [111].

In the case of two dimensional correlations within the kagome planes, we would naively expect a three way, rather than two way splitting of the correlation functions $S(\mathbf{r})$ and $S_{\perp}(\mathbf{r})$. This is based on the fact that any nearest-neighbour chain within the pyrochlore lies in two of the kagome planes that make up the pyrochlore lattice, as illustrated in Fig. 5.2. The second nearest-neighbour directions of the pyrochlore lattice lie within only one of these kagome planes, and the cubic unit cell body diagonals are not parallel to any kagome planes. The fact that the nearest-neighbour directions lie in two kagome planes means that if we had correlations within the kagome planes, but not between them, the correlations along nearest-neighbour chains would have contributions from the correlations

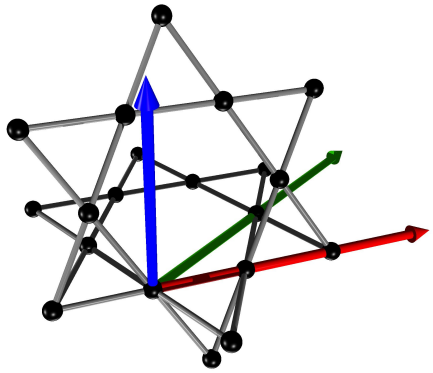

Figure 5.2: High symmetry directions of the pyrochlore lattice. $[0\bar{1}1]$ (red) is one of the nearest-neighbour chain directions of the pyrochlore lattice. $[1\bar{2}1]$ (green) is one of the second nearest-neighbour directions of the pyrochlore lattice that lies within the horizontal kagome plane shown. [111] (blue) is one of the cubic unit cell body diagonal directions of the pyrochlore lattice. Two of the kagome planes that can be used to construct the pyrochlore lattice are shown.

within two kagome planes. This would make these correlations stronger than the correlations along the second nearest-neighbour directions, which would have contributions from only one kagome plane. In addition the correlations along the second nearest-neighbour directions would be stronger than the correlations along the cubic unit cell body diagonals because they are parallel to no kagome planes. This is not consistent with the two-way splitting we observe in $S(\mathbf{r})$ and $S_{\perp}(\mathbf{r})$ computed from our model. We therefore conclude that two dimensional correlations within the kagome planes in the pyrochlore lattice are not the source of the rods of neutron scattering intensity in $Yb_2Ti_2O_7$. Instead, if we return to Fig. 5.3 and examine the correlation function $S(\mathbf{r})$, we can see that the strongest correlations are along the nearest-neighbour chains. Based on this observation we conclude that the rods of scattering somehow arise from the superposition of strong correlations along all of the nearest-neighbour chains that make up the pyrochlore lattice. If the correlations were only along parallel chains, $Yb_2Ti_2O_7$ would exhibit planes of scattering, as shown in Fig. 5.1(d), resulting from a superposition of the scattering resulting from correlations in one direction, and no correlations in two others. However, according to our model the correlations along all of the nearest-neighbour chains are the same. If these chains were orthogonal, it would lead to "spots" in the neutron scattering intensity,

arising from the superposition of correlations in three dimensions. Instead the pyrochlore lattice geometry somehow results in the superposition of nearest-neighbour chain correlations leading to rods of neutron scattering intensity. This model of isotropic correlations along all nearest-neighbour chains within the pyrochlore lattice should be equivalent to isotropic correlations between the spins, as would be found for a Heisenberg ferromagnet on the pyrochlore lattice. Interestingly, preliminary investigations of the Heisenberg ferromagnet on the pyrochlore lattice, discussed in Chapter 7, also find rod-like features in the paramagnetic quasi-elastic neutron scattering.

We have also computed the correlation lengths of $S(\mathbf{r})$ along the three high symmetry directions of the pyrochlore lattice by fitting the correlations in Fig. 5.3(a) to the function $a \exp(-|\mathbf{r}|/\gamma_c)$. Along the nearest-neighbour chain direction $[0\bar{1}1]$, the correlation length is $\gamma_c = 3.8 \pm 0.3$ Å. Along the second nearest-neighbour direction $[1\bar{2}1]$, the correlation length is $\gamma_c = 3.4 \pm 0.6$ Å, and along the cubic unit cell body diagonal the correlation length is $\gamma_c = 3.2 \pm 0.5$ Å. These correlation lengths are not significantly different from one another, which is strange given that the correlation function magnitudes show such clear separation between nearest-neighbour chain directions, and the other high symmetry directions.

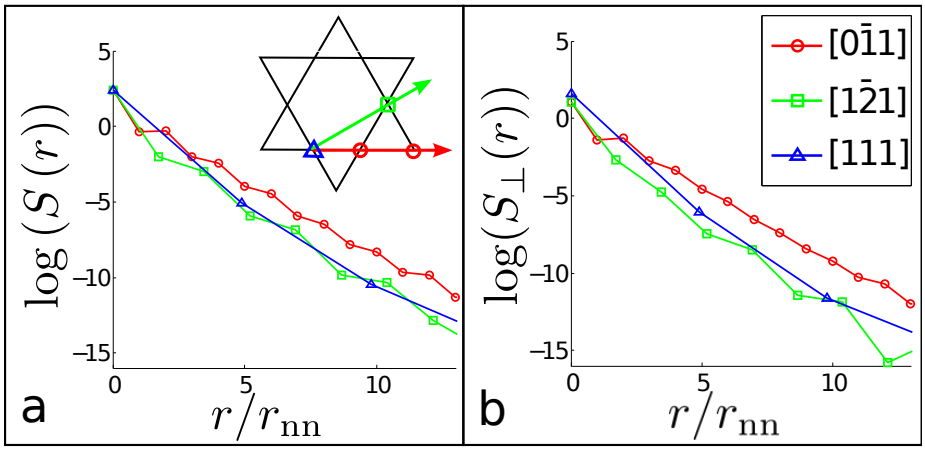

Figure 5.3: Figure reproduced from Ref. [31]. Real space correlations functions $S(\mathbf{r})$ (a) and $S_\perp(\mathbf{r})$ (b), computed at $T = 1.4$ K, plotted along three high symmetry directions of the pyrochlore lattice.

One other possible method to examine the real space correlations is to look at neutron scattering in planes perpendicular to the [111] rod, as shown in Fig. 5.4. The scattering in these planes is computed using the same model Hamiltonian as used to compute the

real space correlation functions, described by the set of couplings $\{\mathcal{J}_e\}$ from Table 4.3 for the CEF parameterization of Hodges *et al.* [20]. In Fig. 5.4 we can see that the rods have a distorted triangular cross section, being widest along the $[1\bar{2}1]$ symmetry related directions, due to the presence of the other symmetry related $\langle 111 \rangle$ rods and other features in the scattering. This cross section is consistent with our calculations of the real space correlations. The width of the rod in a given direction in reciprocal space is inversely proportional to the correlations in that direction in real space. This means that if the rod is wide in a certain direction, it is expected that the correlations in that direction will fall off more quickly than in directions where the rod is narrower. As we can see in Fig. 5.4, the rod is wider along the $[1\bar{2}1]$ symmetry related second nearest-neighbour directions than along the $[0\bar{1}1]$ symmetry related nearest-neighbour chain directions. This is consistent with the correlations along the $[1\bar{2}1]$ symmetry directions being weaker than those along the $[0\bar{1}1]$ symmetry related directions. Based on this logic, if the rods of scattering intensity were indeed due to isotropic correlations in the kagome planes, we would expect the rod to be perfectly circular in cross section. Therefore these neutron scattering plots provide further evidence that correlations within but not between kagome planes is not the correct explanation of the rods.

5.3 Summary

To summarize, we have calculated the real space correlations that result from our model of anisotropic nearest-neighbour bilinear exchange along high symmetry directions of the pyrochlore lattice. Ref. [40] suggested that the rods of scattering intensity in $Yb_2Ti_2O_7$ arise due to correlations within, but not between, the kagome planes that make up the pyrochlore lattice. The results of our calculations are not consistent with this picture. Instead we find that the rods arise due to strong correlations along all of the nearest-neighbour chains in the pyrochlore lattice.

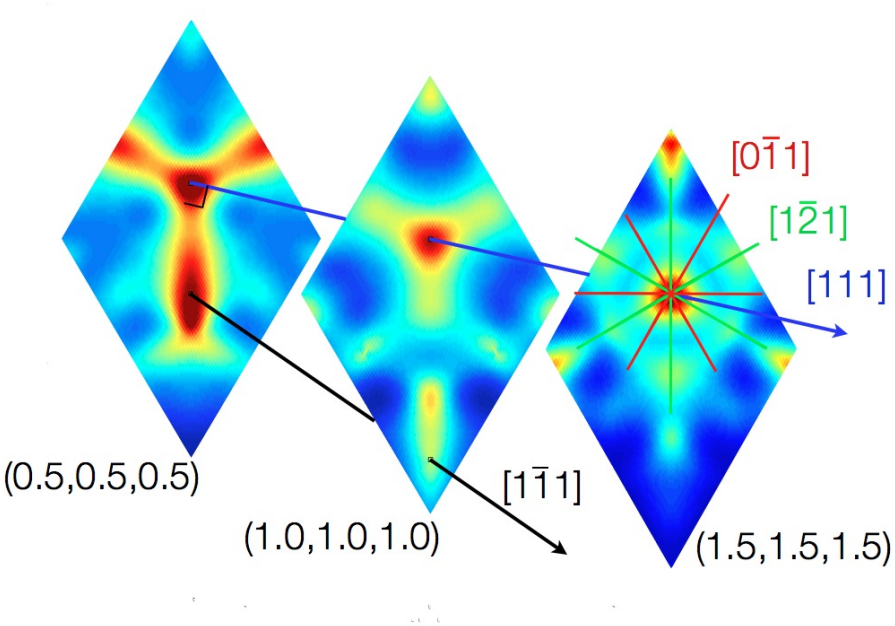

Figure 5.4: RPA Quasi-elastic neutron scattering computed in three planes perpendicular to the direction [111] in reciprocal space, passing through the points $(0.5, 0.5, 0.5)$,$(1, 1, 1)$, and $(1.5, 1.5, 1.5)$. The high symmetry directions $[0\bar{1}1]$ (red), $[1\bar{2}1]$ (green), and [111] (blue) are shown.

Chapter 6

The Local Susceptibility

Now that we possess a pair of Hamiltonians that can successfully reproduce the paramagnetic quasi-elastic neutron scattering of $Yb_2Ti_2O_7$, we wish to obtain an a further confirmation that our models correctly describe the magnetic interactions in $Yb_2Ti_2O_7$. In order to do this, we require an experimentally measurable property of $Yb_2Ti_2O_7$ that depends on the magnetic interactions between Yb^{3+} ions and that we can compute using our model. The quantity that we choose for comparison between experiment and model results is the local susceptibility, χ_a. The local susceptibility was discussed briefly in Chapter 1, where the recent works in which measurements of this quantity were reported and discussed, Refs. [19, 34, 37], were summarized. In this chapter we discuss what χ_a is, and how it is measured in experiment. We will also present calculations of χ_a based on the anisotropic exchange Hamiltonian found for $Yb_2Ti_2O_7$ in Chapter 3.

6.1 Definition of the Local Susceptibility

In magnetic materials the bulk susceptibility χ is defined as $\chi = \frac{\partial M}{\partial H}$, the change of the of the system magnetization M with respect to an external magnetic field H. In a full three dimensional system, χ is actually a 3×3 tensor, with elements $\chi^{uv} = \frac{\partial M^u}{\partial H^v}$, where u and v index the global cartesian components of $\mathbf{M}$ and $\mathbf{H}$, respectively the vector magnetization and external magnetic field. The bulk magnetization describes the response of the average moment of a magnetic system to an external field. The average moment is the sum of all individual magnetic moments divided by the total number of moments. The local susceptibility can also be defined. It describes the response of a single magnetic moment, $\mathbf{M}_a$, to the external field, via the equation $\mathbf{M}_a = \overline{\chi}_a \mathbf{H}$, where $\overline{\chi}_a$ is χ_a expressed in the

global coordinates. The relationship between χ_a and $\overline{\chi}_a$ is given by $\overline{\chi}_a = o^u_{\bar{u},a}\chi_a {o^u_{\bar{u},a}}^T$, where $o^u_{\bar{u},a}$ is the transformation matrix from the local coordinate system at sublattice site a given in Table 1.3 to global cartesian coordinates. The relationship between the bulk and local susceptibility is given by $\chi \equiv \frac{1}{N_s}\sum_a \overline{\chi}_a$, where the sum is over all sublattice sites, and N_s is the number of sublattice sites. If $\overline{\chi}_a$ is the same for all sites on the lattice, then this relationship simplifies to $\chi \equiv \overline{\chi}_a$. If on the other hand $\overline{\chi}_a$ is not the same for all sublattice sites, the sum over the sublattice sites can lead to the bulk and local susceptibilities having very different properties.

In the case of the rare earth pyrochlore oxides, particularly $Yb_2Ti_2O_7$, the crystal structure is formed of a tetrahedral sublattice structure on an FCC lattice. At each sublattice site, the CEF imposes a different asymmetry on the magnetic moments, leading to an inequivalence of χ and $\overline{\chi}_a$. In the case of $Yb_2Ti_2O_7$, the magnetic moments prefer to lie in easy planes (see Fig. 1.4). This means that the components of χ_a will be greatest in these planes, but the sum over all of the sublattices will be completely isotropic, and thus measurements of the bulk susceptibility cannot access any of the easy plane physics in this material. If we define χ_a in terms of the local coordinate systems defined in Table 1.3, then in zero magnetic field, χ_a has two components, $\chi_\parallel$ and $\chi_\perp$, and is of the form

$$\chi_a = \begin{pmatrix} \chi_\perp & 0 & 0 \\ 0 & \chi_\perp & 0 \\ 0 & 0 & \chi_\parallel \end{pmatrix}. \tag{6.1}$$

In global coordinates, $\overline{\chi}_a$ is different at each sublattice site. If we choose sublattice one, then it has the form

$$\overline{\chi}_a = \begin{pmatrix} \overline{\chi}_{1,1} & \overline{\chi}_{1,2} & \overline{\chi}_{1,3} \\ \overline{\chi}_{2,1} & \overline{\chi}_{2,2} & \overline{\chi}_{2,3} \\ \overline{\chi}_{3,1} & \overline{\chi}_{3,2} & \overline{\chi}_{3,3} \end{pmatrix}. \tag{6.2}$$

In the case of local easy planar symmetry $\overline{\chi}_{1,1} = \overline{\chi}_{2,2} = \overline{\chi}_{3,3}$, and $\overline{\chi}_{1,2} = \overline{\chi}_{1,3} = \overline{\chi}_{2,1} = \overline{\chi}_{2,3} = \overline{\chi}_{3,1} = \overline{\chi}_{3,2}$. The relationship between the components of the local susceptibility in these two representations is $\chi_\perp = \overline{\chi}_{1,1} - \overline{\chi}_{1,2}$ and $\chi_\parallel = \overline{\chi}_{1,1} + 2\overline{\chi}_{1,2}$. These four relationships can be found quite simply by, applying the rotation matrices $o^u_{\bar{u},a}$ to Eqn. (6.2).

Now that we have defined the quantity we wish to compute, we can look at how it is measured in real materials. This is done by using the results of polarized neutron scattering measurements, following the method of Gukasov and Brown laid out in Ref. [35]. As already stated, $\overline{\chi}_a$ is the quantity relating the magnetic moment at a single sublattice site to the external field, that is $\mathbf{M}_a = \overline{\chi}_a \mathbf{H}$. The same holds for all sublattice sites, meaning that

for another sublattice site, b, $\mathbf{M}_b = \overline{\chi}_b \mathbf{H}$. The local susceptibility at these two sublattice sites are, following Ref. [35], related by the equation $\overline{\chi}_b = \tilde{\mathbf{R}} \overline{\chi}_a \tilde{\mathbf{R}}^{-1}$. $\tilde{\mathbf{R}}$ is the rotation matrix component of the space group symmetry operation connecting the two sublattice sites, $\{\tilde{\mathbf{R}} : \mathbf{t}\}$, and $\mathbf{t}$ is the translation vector between the sites.

If we start with an atom at position $\mathbf{r}_a$, then we can construct the position dependent magnetization as

$$\mathbf{M}(\mathbf{r}) = \sum_p \tilde{\mathbf{R}}_p \overline{\chi}_a \tilde{\mathbf{R}}_p^{-1} \mathbf{H} \; \rho\left(\mathbf{r} - \tilde{\mathbf{R}}_p \mathbf{r}_a - \mathbf{t}_p\right), \tag{6.3}$$

where $\rho(\mathbf{r})$ is the distribution of the magnetic moment about the lattice site. The sum over p is the sum over all N_g symmetry operations for the space group that describes the lattice. Fourier transforming this equation yields [35]

$$\mathbf{M}(\mathbf{q}) = \frac{1}{N_a} f(\mathbf{q}) \sum_p \tilde{\mathbf{R}}_p \chi_a \tilde{\mathbf{R}}_p^{-1} \mathbf{H} \exp i\mathbf{q} \cdot \left(\tilde{\mathbf{R}}_p \mathbf{r}_a + \mathbf{t}_p\right), \tag{6.4}$$

where $f(\mathbf{q}) = \int_0^\infty \exp(ikr)\, 4\pi r^2 \rho(r)\, dr$, assuming spherical symmetry for $\rho(r)$, is the magnetic form factor. N_a is the number of operators q for which $\tilde{\mathbf{R}}_q \mathbf{r}_a + \mathbf{t}_q = \mathbf{r}_a$ and N_g/N_a is the multiplicity of the lattice site a [35].

Next we examine the form of the equation for polarized neutron scattering intensity [35]

$$I(\mathbf{q}) = N^2 + 2\mathbf{P}_0 \cdot (N' M'_\perp + N'' M''_\perp) + M_\perp^2, \tag{6.5}$$

where $N = N' + iN''$ is the nuclear structure factor and $\mathbf{P}_0$ is the polarization vector [35]. $M_\perp = M'_\perp + iM''_\perp = \mathbf{q} \times \mathbf{M}(\mathbf{q}) \times \mathbf{q}$ is the component of the reciprocal space magnetization perpendicular to the scattering wave-vector $\mathbf{q}$ [35]. This equation directly relates the reciprocal space magnetization $\mathbf{M}(\mathbf{q})$ and the polarized neutron scattering $I(\mathbf{q})$, so that it should be possible to extract one from the other.

According to Ref. [35], the actual quantity measured in experiments used to determine χ_a is the polarized neutron scattering flipping ratio $R = I^+/I^-$. $I^+(\mathbf{q})$ and $I^-(\mathbf{q})$ are the scattering intensities for neutrons polarized parallel and anti-parallel to the external magnetic field. The ratio R can be directly related to χ_a using Eqns. (6.4) and (6.5). Using numerical refinement methods it is then possible to vary the components of χ_a until the flipping ratio for multiple points in reciprocal space have been matched and thus determine the form of χ_a [35].

6.2 Calculating the Local Susceptibility

The obvious method of choice for computing the local susceptibility for $Yb_2Ti_2O_7$ from our model is the random phase approximation (RPA), as discussed in Chapter 3.3. If we were to use this method, $\overline{\chi_a}$ is given by

$$\overline{\chi_a}^{uv} = \sum_b \overline{\chi}_{ab}^{uv} \left(\mathbf{q} = 0, \omega = 0\right), \tag{6.6}$$

where $\overline{\chi}_{ab}^{uv}\left(\mathbf{q} = 0, \omega = 0\right)$ is the wave-vector dependent RPA susceptibility at $\mathbf{q} = 0$, defined in Eqn. (3.61). The global susceptibility is given by

$$\chi^{uv} = \frac{1}{4} \sum_a \overline{\chi_a}^{uv}. \tag{6.7}$$

This allows for the direct calculation of the bulk susceptibility χ using the RPA methods of Chapter 3.3.

Unfortunately the method of Chapter 3.3 and the CEF states of Appendix A do not account for an applied magnetic field. In Ref. [19] it is explained that χ_a is in fact measured in a 1 T field applied along the [110] direction. This field is large so calculations performed in zero field will not be valid for comparison to experiment. It is possible to perform RPA calculations of the local susceptibility using CEF states diagonalized in the presence of the 1 T field along [110], but this will yield the change in the local moment due to a small perturbing field applied in addition to the 1 T field. The quantity measured in experiment on the other hand is the change in the local moment due to the entire applied 1 T field. This difference between the RPA susceptibility and the experimentally measured quantity means that we cannot use the RPA susceptibility to compute χ_a. What we must actually compute is the expectation value of the magnetic moment at each sublattice site. Dividing this value by the applied magnetic field will yield magnetic susceptibility in units of μ_B/T due to the entire applied field, and not just a weaker applied field superimposed on the 1 T field. All of the measurements of χ_a were collected well above the temperature of the phase transition in $Yb_2Ti_2O_7$, $T_c \sim 220$ mK, so the expectation value of the moments will be zero when there is no applied field, and thus it is valid to assume that any moment found is due to the presence of the field. To calculate the the expectation value of the magnetic moment at each sublattice site we choose to use a mean field method.

The strong [110] field also introduces a second problem; it breaks the symmetry of the pyrochlore lattice, and splits the doublet ground state of $Yb_2Ti_2O_7$. This means that some of the assumptions made in Chapter 6.1 about the form of the local susceptibility are

incorrect. Specifically, the assumption of Ref. [19] that the local susceptibility expressed in local coordinates is the same at each sublattice site, is now incorrect. This occurs because the field splits the lattice into two types of nearest-neighbour chains, known as α and β chains, parallel and perpendicular to the applied field respectively. These chains are shown in Fig. 6.1. This assumption does not affect our calculations because we are not performing a fit to experiment, but rather an independent calculation based on our model, of χ_a at each sublattice site, with no assumptions about the form of this quantity,

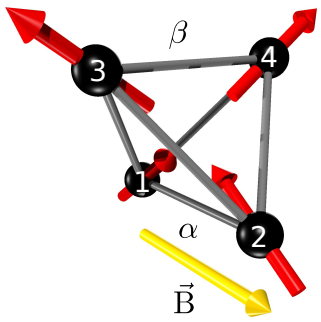

Figure 6.1: The tetrahedral sublattice of the pyrochlore lattice, showing the local $\hat{z}$ axes (red arrows) and the direction of the applied [110] magnetic field $\vec{\mathbf{B}}$ (yellow arrow). The α and β chains parallel and perpendicular to the applied field are labeled.

To calculate the local susceptibility using the more correct mean field method, we compute the moments at each sublattice site in a local mean field theory. This local mean field calculation was performed by diagonalizing the CEF matrix in the presence of a magnetic field, in a similar manner to that used to obtain the CEF states in Appendix A [38].

The interactions between the magnetic moments $\mathbf{J}_i^a$ are handled in the following manner. The interaction between two components of nearest-neighbour ions $\mathbf{J}_i^a$ and $\mathbf{J}_j^b$ is expanded in terms of expectation values as [38]

$$J_i^{au} J_j^{bv} = J_i^{au}\langle J_j^{bv}\rangle + \langle J_i^{au}\rangle J_j^{bv} - 2\langle J_i^{au}\rangle\langle J_j^{bv}\rangle + \left(J_i^{au} - \langle J_i^{au}\rangle\right)\left(J_j^{bv} - \langle J_j^{bv}\rangle\right), \tag{6.8}$$

where $\langle J_i^{au}\rangle$ is the expectation value of the u component of the angular momentum operator $\mathbf{J}_i^a$. By dropping the final term of this equation, the fluctuation term, we obtain a decoupled mean field equation. This allows us to treat the interactions between the lattice sites i, a and j, b as an effective field. The u component of the resulting interaction field at site i, a

due to the v component of J_j^b is then given by

$$h_{i,\text{eff}}^{au} = \tilde{\mathcal{J}}\langle J_j^{bv}\rangle, \tag{6.9}$$

where $\tilde{\mathcal{J}}$ is whatever combination of coupling terms in $\{\mathcal{J}_e\}$ governs the interactions between these two spin components. The total interaction field at site i, a is then given by summing over all of the nearest-neighbours j, b and components v. $\mathbf{h}_{i,\text{eff}}^a$ is then used in the mean field interaction portion of the Hamiltonian

$$H_{\text{int,MF}}(i,a) = -\mathbf{J}_i^a \cdot \mathbf{h}_{i,\text{eff}}^a. \tag{6.10}$$

Single ion wave-functions $|\nu\rangle$, at each lattice site i, a are then determined by diagonalizing $H_{\text{MF}} = \sum_i H_{\text{MF}}(i,a)$, where the sum over i, a represents the sum over all pyrochlore lattice sites. The combination of the CEF, applied magnetic field, and interaction leads to three terms in H_{MF}

$$H_{\text{MF}} = H_{\text{cf}} + H_Z + H_{\text{int,MF}}, \tag{6.11}$$

where H_{cf} is the crystal field term, discussed in Appendix A, $H_{\text{int,MF}}$ is the mean field interaction Hamiltonian, and H_Z is the Zeeman interaction term, given by

$$H_Z = \sum_{i,a} -\mu_B g_J \sum \mathbf{J}_i^a \cdot \mathbf{B}. \tag{6.12}$$

$\langle J_i^{au}\rangle$ is then given by

$$\langle J_i^{au}\rangle = \frac{Tr\left(J_i^{au}\exp\left(-\beta H_{\text{MF}}\left(i,a\right)\right)\right)}{Z}, \tag{6.13}$$

where $Z = Tr\left(\exp\left(-\beta H_{\text{MF}}\left(i\right)\right)\right)$ is the partition function. Repeated diagonalization of H_{MF} on a 16-site unit cell using periodic boundary conditions [38] refines the values of $\langle J_i^{au}\rangle$ until they no longer change by a significant amount after each step. The resulting value of $\langle J_i^{au}\rangle$ is used to determine the components of χ_a. The use of a 16-site unit cell is justified by our findings in Chapter 3; that the mean-field ordering wave-vector of these models is $\mathbf{q} = 0$ [38]. This process was performed over a range of temperatures to produce data for comparison to experiment. These calculations of χ_a using the mean field method were performed by Dr. Paul McClarty, and we are very grateful for his contribution.

6.3 Results

If we compute χ_a using only the CEF parameterizations of Refs. [19] and [20], and not interactions, we obtain the results shown in Fig. 6.2. In Fig. 6.2 it can be seen quite clearly

that the values of $\chi_\perp$ fit the experimental data well despite a lack of magnetic interactions. This CEF only model is successful in fitting $\chi_\perp$ except at the lowest temperature point $T = 2$ K, where the model data falls below the experimental data point. The model values of $\chi_\parallel$ on the other hand are seen to be quite different from both experiment and each other. The calculations of $\chi_\parallel$ based on the CEF parameterization of Ref. [19] fit the experimental data in the range $T = 20 - 70$ K, but the fit fails at both high and low temperatures. The calculations based on the CEF parameterization of Ref. [20] do not fit the experimental values of $\chi_\parallel$ well at any temperature and because of this poor fit we discard this CEF parameterization from further comparison to experiment. $\chi_\parallel$ for sublattices 3 and 4 is not shown because this quantity is zero. This is because in the β chains (see Fig. 6.1), the applied field polarizes the magnetic moments along the field, and in the easy plane of the ground state doublet, so there is no component of the moment along the local z axis with which to compute $\chi_\parallel$.

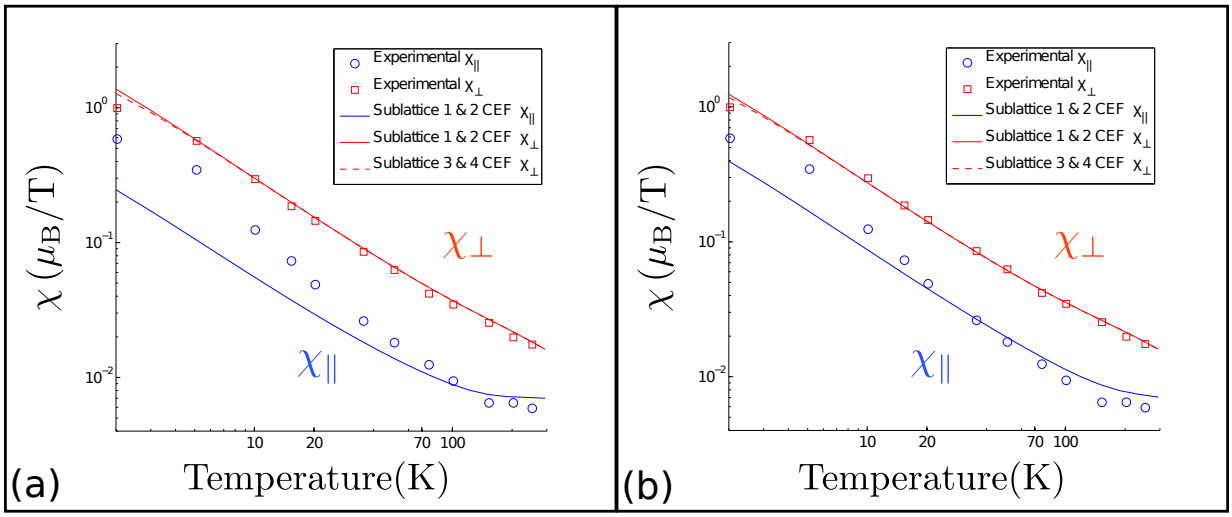

Figure 6.2: Calculations of the two components of χ_a with no interactions, using the CEF parameterizations of Ref. [20] (a) and Ref. [19] (b). $\chi_\perp$, and $\chi_\parallel$ are shown along with the experimentally determined values from Ref. [19]. $\chi_\parallel$ for sublattices 3 and 4 is zero.

Fig. 6.3 shows calculations based on the exchange couplings $\{\mathcal{J}_e\}$ of Table 4.3 for Ref. [19], along with calculations base on the isotropic exchange model discussed in Chapter 4.2. Also shown is a reproduction of the fit of Ref. [19]. This fit fails to take into account the sublattice structure of the pyrochlore lattice. It can be seen in Fig. 6.3 that the incorporation of anisotropic bilinear exchange into the mean field calculations greatly

improves the low temperature fit to $\chi_{\|}$, leading to a good fit to all but the lowest temperature point. For comparison, the same calculations were performed using an isotropic exchange model, constrained by the experimental value of $\theta_{\rm CW} = 0.75$ K [20]. The results of these calculations are shown in Fig. 6.3, where it can be seen that these calculations do not fit $\chi_{\|}$ as well as the anisotropic exchange calculations. The fit of Ref. [19] is shown in Fig. 6.3(c), and comparing this to the results of our anisotropic exchange calculations it can be seen that our calculations fit the data at least as well.

So far we have only discussed the fit of our anisotropic exchange model to χ_a at low temperatures. The calculations of χ_a when anisotropic exchange is included do not fit the high temperature data ($T > 70$ K) any better than those performed with only the CEF and Zeeman terms in $H_{\rm MF}$. One possible reason for this is that both of the CEF parameterizations used in this work fail to correctly describe the excited states of the CEF and so they fail at high temperatures. This question of whether the CEF parameterization is at issue can only be answered by further experiments to determine the precise excited states (i.e. their energies and wavefunctions) of the CEF.

RPA calculations of the powder susceptibility have also been performed using the anisotropic exchange models defined by $\{\mathcal{J}_e\}$ in Table 4.3 for the CEF parameterization of Cao *et al.* [19]. The RPA calculation using the CEF states of Appendix A is valid in this case because these experiments were performed in very low field. The results of these calculations are shown in Fig. 6.4(b). These are actually plots of the average of the three elements of χ (Eqn. (4.5)), because the experiments of Ref. [34] were performed on powder samples of $Yb_2Ti_2O_7$. It should be noted that Ref. [34] makes no mention of any demagnetization correction in the analysis of the data. Examining these results, it can be seen that once again, our anisotropic exchange model fits the experimental data well over a broad range of temperatures. The comparison to experiment is made easier by Fig. 6.4(c), which shows the differences between χ computed using: our anisotropic exchange model and experiment, our isotropic exchange model and experiment, and the fit of Ref. [34] (shown in Fig. 6.4(a)) and experiment. From this data we can see that the isotropic exchange calculations fit increasingly poorly at high temperatures, whereas calculations performed using our anisotropic exchange model give χ greater than experiment below $T \sim 20$ K and less than experiment above that temperature. The fit of Ref. [34] shows the opposite behaviour to our anisotropic exchange calculations.

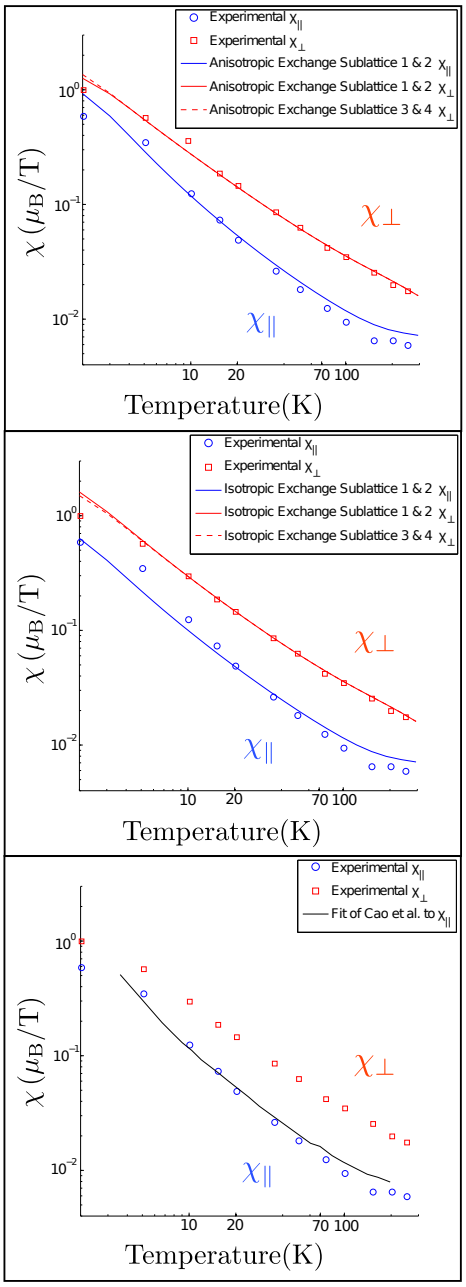

Figure 6.3: Calculations of the two components of χ_a with a model including magnetic interactions, using the exchange couplings $\{\mathcal{J}_e\}$ from Table 4.3 for the CEF parameterization of Ref. [19] (a). Calculations performed using Isotropic exchange and long-range dipolar interactions $\mathcal{J}_{\rm iso} = 0.06$ K) are shown in panel (b). Panel (c) shows the fit of Ref. [19] to $\chi_\perp$ for comparison purposes. $\chi_\perp$ for sublattices 3 and 4 is zero.

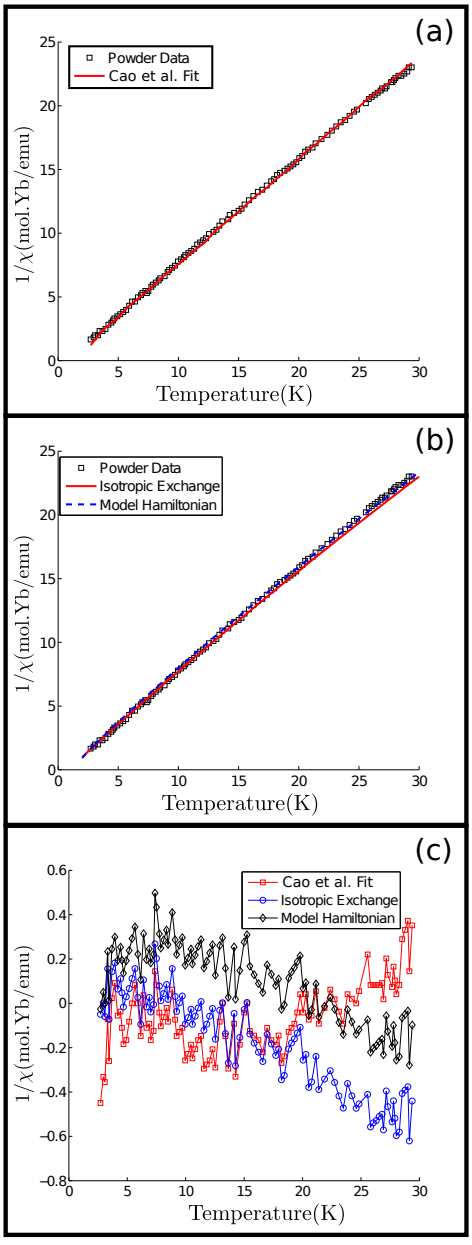

Figure 6.4: Panel (a) shows the experimentally measured bulk susceptibility of $Yb_2Ti_2O_7$ from Ref. [34], along with the fit of Ref. [34] to said data. Panel (b) shows the results of our RPA calculations using both anisotropic exchange, specifically the set of $\{\mathcal{J}_e\}$ determined using the CEF of Cao *et al.*, and isotropic exchange with long-range dipolar interactions. Panel (c) shows the differences between the bulk susceptibility computed using all three models and experiment.

6.4 Summary

In this chapter we have presented calculations of the local and bulk susceptibility performed using our anisotropic bilinear nearest-neighbour exchange models determined from fitting the quasi-elastic neutron scattering. With no adjustment of parameters, the anisotropic exchange model determined using the CEF paramterization of Ref. [19] fits experimental measurements of χ_a fairly well. The CEF parameterization of Ref. [20] was found to fit experiment poorly, perhaps indicating that future work should not be focused on this CEF parameterization. Bulk susceptibility calculations based on our anisotropic exchange model also fit experimental measurements of this quantity, reported in Ref. [34], quite well. These results provide additional confirmation that our model successfully describes the magnetic interactions in $Yb_2Ti_2O_7$ at low temperatures.

Chapter 7

Ongoing and Prospective Future Research

The next logical step after determining the magnetic interaction Hamiltonian for $Yb_2Ti_2O_7$, is to determine what the low temperature phase of this model is. In this chapter we provide a brief description of ongoing as well as proposed work involving the low temperature phase of this specific model for $Yb_2Ti_2O_7$. We also provide a brief discussion on potential investigations of the general $\{\mathcal{J}_e\}$ interaction space for the local planar but not perfectly XY model on the pyrochlore lattice and discuss ongoing investigations of the properties of the Heisenberg ferromagnet on the pyrochlore lattice.

7.1 Monte Carlo Simulations

Classical Monte Carlo simulations based on the anisotropic exchange model we have determined from fitting quasi-elastic neutron scattering measurements are currently ongoing. These simulations are being performed using an effective spin-1/2 model equivalent of our bilinear exchange model discussed in Appendix H. The classical Monte Carlo code used was written by Dr. Pawel Stasiak for his Ph.D. Thesis [56] and takes advantage of parallel tempering to improve the equilibration of the simulation. This code has been augmented by the inclusion of the symmetry allowed nearest-neighbour bilinear exchange terms discussed in this study. These simulations have been performed both with and without long-range magnetic dipolar interactions. This was done because long-range magnetic dipolar interactions significantly slow the simulation process. Figure 7.1 shows the sublattice magnetization,

energy per moment, and specific heat per moment for an $L = 5$ system with periodic boundary conditions containing 2000 spins. L is the number of 16 site cubic units cells in each of the cartesian coordinate directions, so that the total system is an $L \times L \times L$ cube. These results show evidence of a phase transition for both models around $T_c \sim 130$ mK, which is much closer to the experimentally observed transition temperature of 214 mK [16] than the critical temperature found by RPA calculations in Chapter 3, $T_{\mathrm{RPA}} \sim 1.17$ K. This massive reduction in T_c shows that thermal fluctuations have a significant effect in this model. Whether these transitions are first or second order is currently under investigation. Finite size analysis and examination of the energy histogram of the simulations have yet to provide concrete evidence for a first or second order phase transition for either model. It is interesting to note the significant difference in the height and shape of the peak in the specific heat computed from the two models in Fig. 7.1(c). This indicates that the phase transition is somehow different without the presence of long-range magnetic dipolar interactions than with them. The peak in the specific heat for the model with no long-range magnetic dipolar interactions is rather small and rounded. This is very strange because studies of the low temperature phase of this model discussed in the next section indicate that this phase transition is likely an example of a thermal order-by-disorder transition. Theoretical work to date has found that such phase transitions should be at least weakly first order [57], which is inconsistent with the observed peak in the specific heat, though simulations of larger system sizes my resolve this issue.

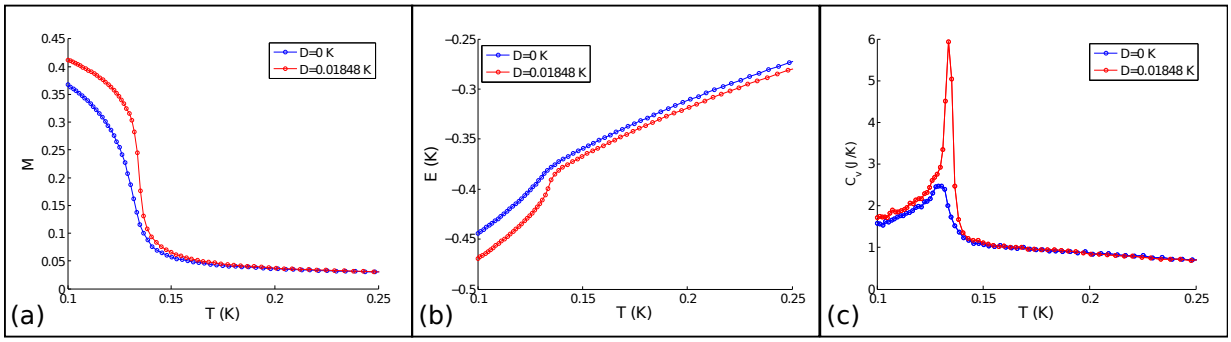

Figure 7.1: Monte Carlo simulation results for an $L = 5$ system with periodic boundary conditions. Panel (a) shows the sublattice magnetization, which goes to 1/2 as $T \to 0$, as expected for a classical spin-1/2 system. Panel (b) shows the energy per magnetic moment and panel (c) shows the specific heat per magnetic moment. All three of these quantities show features near $T_c \sim 130$ mK, indicating the presence of a phase transition.

Figure 7.2 shows the ground states of the simulations performed with and without long-

range magnetic dipolar interactions. These states were determined with the assistance of mean field calculations, discussed in Chapter 7.2. The ground state of our anisotropic exchange model without long-range magnetic dipolar interactions has no net moment. The ground state when long-range magnetic dipolar interactions are used with $D = 0.01848$ K, is a ferromagnetic, canted spin ice state state, with a net moment. This begs the question: why is the ground state of our anisotropic exchange model for $Yb_2Ti_2O_7$ so sensitive to such a weak interaction? D is approximately $1/10^{th}$ of the strength of the next strongest interaction in this model, and this relative weakness would naively lead one to expect it to have no effect on the ground state of the system, making its large effect on the ground state of the model very curious.

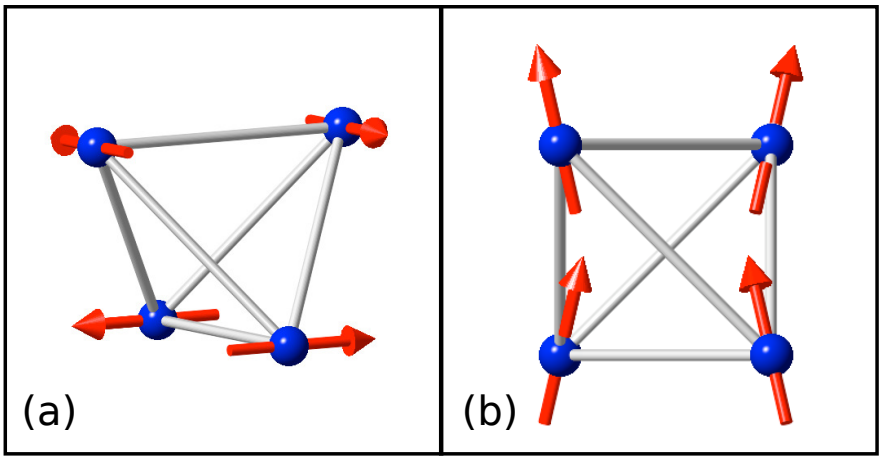

Figure 7.2: The low temperature ground states of the classical anisotropic spin-1/2 model determined using Monte Carlo simulations and mean field calculations. Panel (a) shows the ground state of the model with no long-range magnetic dipolar interactions. Panel (b) shows the ground state when $D = 0.01848$ K.

7.2 Mean Field Calculations

In addition to classical Monte Carlo simulations, mean-field calculations of the free energy have been performed using the effective spin-1/2 equivalent to our model by Mr. Behnam Javanparast. These calculations confirm the results of the Monte Carlo simulations, though they do find that the ground state of the model without long-range magnetic dipolar

interactions is degenerate to symmetry rotation within the easy planes. The Monte Carlo simulations found that specific orientations of the moments were selected, such as the one shown in Fig. 7.2(a), suggesting that thermal order-by-disorder [3]is taking place. This has been confirmed by histogram analysis of the easy plane moment angles from Monte Carlo simulations shown in Fig. 7.3. There it can be seen that the in plane moments prefer to lie at angles $\phi = (n + 1/2)(\pi/3)$. These angles correspond to the ψ_3 state of Ref. [58], also known as the "anti-Palmer-Chalker" state, which is shown in Fig. 7.2.

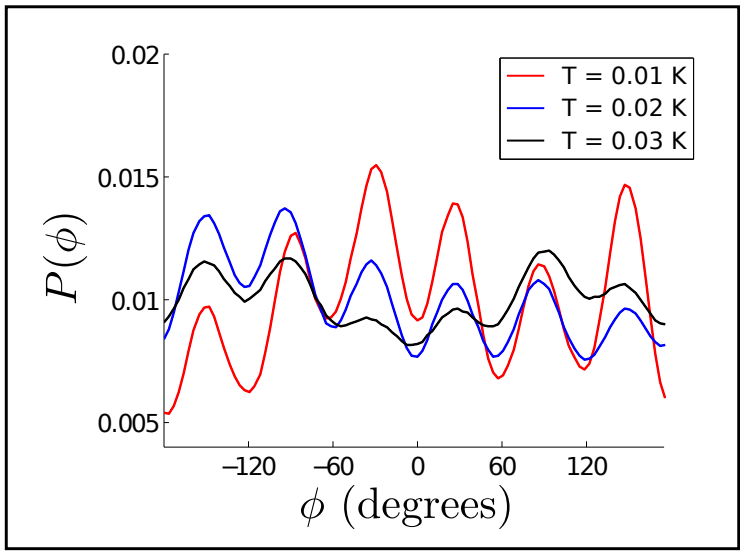

Figure 7.3: Monte Carlo calculations of $P(\phi)$ for our bilinear exchange model with no long-range magnetic dipolar interactions for $T = 0.01$ K, 0.02 K, and 0.03 K for an $L = 2$ system. ϕ is the easy plane rotation angle, the out of plane angle θ is 0.

Mean field calculations have also been performed to attempt to understand the sensitivity of our anisotropic exchange model to the presence of the long-range magnetic dipolar interaction. The result of these calculations is that the eigenvalues of the Fourier transformed interaction matrix (see footnote on pg. 62) corresponding to the normal mode amplitudes associated with the canted spin ice ground state and the anti-Palmer-Chalker

[3]Thermal order by disorder is a phenomenon whereby unique ground states are selected by thermal fluctuations from a manifold of extensively degenerate classical ground states [59]. The specific states selected by this mechanism will be those with the greatest density of zero modes. For these states, the magnitude of the entropic contribution to the free energy will be greater than for the other states in the manifold, leading to the minimization of the free energy in these states.

ground state are very close close together in energy ($\Delta \sim 3\%$) when there are no long-range magnetic dipolar interactions. As the strength of the long-range magnetic dipolar interactions is increased, the eigenvalues corresponding to the two different ground states cross, leading to the change in the ground state. This crossing occurs at $D_c \sim 0.008$ K, which is approximately half of $D = 0.01848$ K the value of D for $Yb_2Ti_2O_7$. The small gap between the eigenvalues associated with two very different types of magnetic LRO when no long-range magnetic interactions are present means that this specific model will be very susceptible to weak perturbations. This explains why such weak long-range magnetic interactions are capable of driving a phase transition from the anti-Palmer-Chalker state to the canted spin ice state. The fact that the correct value of D for $Yb_2Ti_2O_7$ is approximately twice the critical value D_c, means that $Yb_2Ti_2O_7$ is well within the canted spin ice phase in the mean field phase diagram of the nearest-neighbour bilinear exchange with long-range magnetic dipolar interaction, $\{\mathcal{J}_e\} + D$, model of the XY like effective spin-1/2 model of $Yb_2Ti_2O_7$. This is a very qualified statement, because many different properties of the model, such as the planar nature of the spins and the specific strength of all of the interactions, combine to yield this phase. It does however provide some motivation for further explorations of this phase diagram, to determine if any other combinations of anisotropic exchange, long-range magnetic dipolar interactions, and anisotropic spins yield interesting physics.

7.3 Quantum Fluctuations

We saw from the classical Monte Carlo results that thermal fluctuations are very important in our anisotropic exchange model, leading to a massive change in the critical temperature of the model computed using RPA and Monte Carlo methods. At very low temperatures these thermal fluctuations will be greatly reduced but they may be replaced by quantum fluctuations of the magnetic moments. $Yb_2Ti_2O_7$ may be especially susceptible to such quantum fluctuations as the ground state doublet can be treated as an effective spin-1/2 model and spin-1/2 systems have been known to exhibit large quantum fluctuations. The low temperature phase of the model with no long-range magnetic dipolar interactions is anti-ferromagnetic in nature suggesting that quantum fluctuations may be significant in this phase. The low temperature phase of the model with long-range magnetic interactions on the other hand, is ferromagnetic in nature and has a discrete set of ground states, suggesting that quantum fluctuations should be gapped out. The size of this gap, and thus its ability to suppress quantum fluctuations is an outstanding question of this model. The strength of the long-range magnetic dipolar interaction that drives the transition from the

anti-Palmer-Chalker phase, found when no long-range magnetic dipoles are present, to the canted spin ice phase is very small, $D \sim 0.02$ K. This means that the energy gap associated with the lowest energy spin wave mode may be quite small, so that quantum fluctuations may in fact be significant in the canted spin ice phase. Experiments performed on the low temperature phase of $Yb_2Ti_2O_7$ find no evidence of magnetic long-range order [6, 15] (see footnote on pg. 15). Perhaps quantum fluctuations drive the system into a disordered phase or even a spin liquid phase, thus explaining the lack of magnetic long-range order in $Yb_2Ti_2O_7$ at low temperatures. Investigations using the method of Ref. [60] for spin wave calculations on the pyrochlore lattice have begun in order to determine what effects quantum fluctuations play in the ground state of our model, but so far no results have been obtained.

7.4 Ground States the Full $\{\mathcal{J}_e\}$ Phase Space for the Non-Ideal Local-Planar Pyrochlore Model

The small difference between the mean field eigenvalues of the Fourier transformed interaction matrix (see footnote on pg. 62) when long-range magnetic dipolar interactions are not present, which correspond to two very different types of ground state of our anisotropic exchange model, is very intriguing. It raises questions about the stability of the ground state to changes in the relative strengths of the bilinear exchange terms $\{\mathcal{J}_e\}$. Investigation of the more general "non-perfect XY" model in the space of all possible $\{\mathcal{J}_e\}$ may yield interesting results. Particularly, as the long-range magnetic dipolar interaction has been found to be very significant in determining the low temperature phase of the model, perhaps investigations of the strength of the pseudo-dipolar exchange interaction as a function of the local Ising exchange interaction strength may yield interesting results. It may be possible to drive the anti-Palmer-Chalker to canted spin ice phase transition using some combination of the bilinear exchange interactions, and as the pseudo-dipolar exchange is so similar in form to the long-range magnetic dipolar interaction, this seems an obvious place to begin the investigation.

Also, as previously mentioned, experiments on $Yb_2Ti_2O_7$ find no evidence of long-range magnetic order in the low temperature phase, suggesting some type of disorder is preventing the system from achieving this ordered phase. One possible source of this disorder is material imperfections not considered in this work. Theoretical studies of the sensitivity of our model or similar models to dilution of the magnetic moments, and or distortion of the lattice may also yield very interesting results.

7.5 Rods of Scattering: The Pyrochlore Heisenberg Ferromagnet

Finally, preliminary investigations have been performed on the Heisenberg ferromagnet on the pyrochlore lattice. These investigations were originally performed as a simple test case, in order to better understand the real space correlations that arise from our anisotropic exchange model, discussed in Chapter 5. This investigation is based on computing the quasi-elastic neutron scattering and real space correlation functions using the mean-field method presented in Refs. [54, 55, 61]. This method is based on finding the normal modes of the Fourier transformed order parameters for each of the sublattice sites (see footnote on pg. 62). From the eigenvalues and eigenvectors of the Fourier transformed interaction matrix $\mathcal{K}(\mathbf{Q})$ (Eqn. (3.61)) corresponding to these normal modes, the mean-field neutron scattering and real-space correlation functions can be computed. This mean field approach is used as we do not possess a set of crystal field states for the Heisenberg ferromagnet, which are a required starting point for the use of the RPA method discussed in Chapter 3.3.

The results of our mean field calculations of the quasi-elastic neutron scattering and real space correlation functions, $S(\mathbf{r})$ (Eqn. (5.2)), can be seen in Fig. 7.4. Figures 7.4(a) and (b) show that the Heisenberg ferromagnet on the pyrochlore lattice displays [111] rods of quasi-elastic neutron scattering intensity. Figure 7.4(c) shows the real space correlation function $S(\mathbf{r})$ computed along three of the high symmetry directions of the pyrochlore lattice. From this calculation we can see that $S(\mathbf{r})$ for the Heisenberg ferromagnet shows similar splitting between in the strength of $S(\mathbf{r})$ along the nearest-neighbour direction $[0\bar{1}1]$ and the second nearest-neighbour $[1\bar{2}1]$ to the splitting found for our anisotropic exchange model (see Fig. 5.3). This indicates that the presence of stronger correlations along nearest-neighbour chains within the kagome planes that make up the pyrochlore lattice than along other directions within these planes may be responsible for rod-like features in the neutron scattering of pyrochlore materials. In the case of the Heisenberg ferromagnet the splitting is not as large as that observed in our anisotropic exchange model. This weaker splitting may explain why the rods are weaker in Figs. 7.4(a) and (b) than those found for our anisotropic exchange model. There is one significant difference between the correlation functions of the two models, the fact that for the Heisenberg ferromagnet, $S(\mathbf{r})$ computed along [111] is just as strong as $S(\mathbf{r})$ computed along the nearest neighbour chains direction. What this means in relation to form of the rod-like features observed is currently unknown.

The rods of scattering generated by the Heisenberg ferromagnet on the pyrochlore lattice, and the splitting of $S(\mathbf{r})$ between nearest-neighbour chains and second nearest-

neighbour directions, suggest that there may be a hidden relationship between these two models. Perhaps studying the Heisenberg ferromagnet may lead to a better understanding of how the rods of scattering present in $Yb_2Ti_2O_7$ arise, and how the rods of scattering are related to the magnetic correlations in $Yb_2Ti_2O_7$. The existence of [111] rods in the neutron scattering of the Heisenberg ferromagnet on the pyrochlore lattice may also indicated that the rods are directly related to the symmetry of the pyrochlore lattice. Further study of the Heisenberg ferromagnet on the pyrochlore lattice is required and a real material described by this model would be quite interesting to study. One current prospect for such a material is $Lu_2V_2O_7$, but this material has recently been found to possess significant easy axis anisotropy [62].

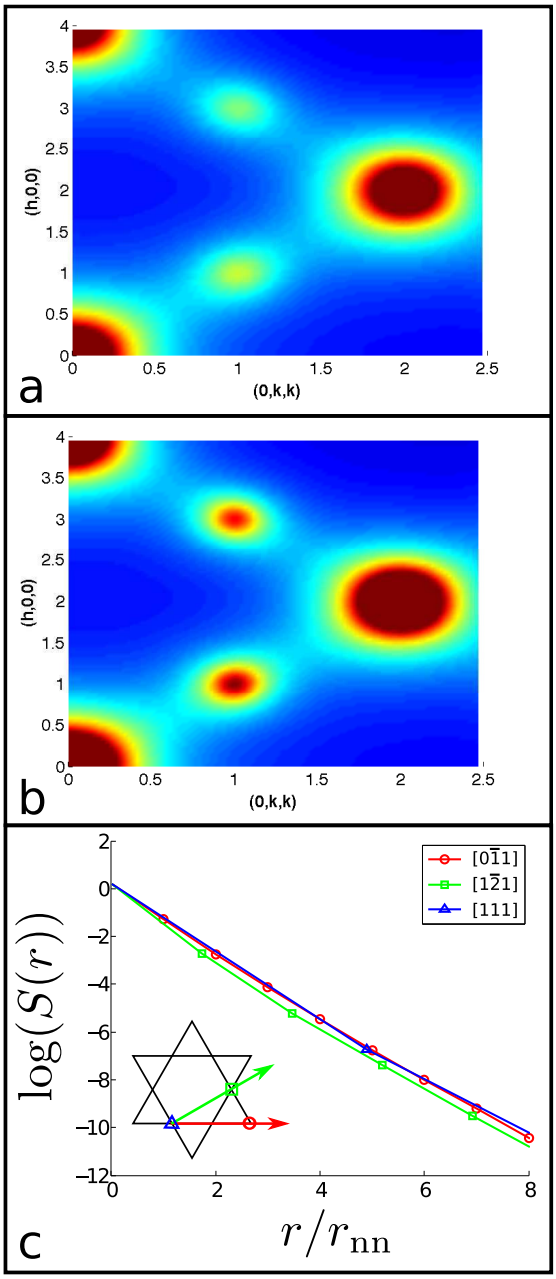

Figure 7.4: Mean field neutron scattering results for the Heisenberg ferromagnet at (a) $T = 1.1\ T_c^{\mathrm{MF}}$ and (b) $T = 1.05\ T_c^{\mathrm{MF}}$. Panel (c) shows real space correlation functions computed at $T = 1.05\ T_c^{\mathrm{MF}}$ plotted along the high symmetry directions of the pyrochlore lattice, as shown in the inset.

Chapter 8

Conclusions

The study of frustrated magnetic materials has led to the discovery of many novel and exotic low temperature phenomena. One family of frustrated magnetic materials in particular, the rare earth pyrochlore oxides, have been found to display a broad range of interesting low temperature behaviours ranging from spin liquid behaviour in $Tb_2Ti_2O_7$ [9], to spin ice in $Dy_2Ti_2O_7$ and $Ho_2Ti_2O_7$ [1], to persistent spin dynamics at even the lowest measured temperatures in $Gd_2Sn_2O_7$ and $Er_2Ti_2O_7$ [1]. These interesting phenomena arise due to material specific conditions, making the study of other rare earth pyrochlore oxide materials an excellent prospect for discovering even more exotic low temperature phenomena. One such material is $Yb_2Ti_2O_7$, where experiments have found evidence of a first order phase transition [15, 16] in powder samples of this material at $T_c \sim 220$ mK, but no evidence of long-range order below the temperature of this phase transition [6, 15] (see footnote on pg. 15). In fact evidence is found for continued spin dynamics below the temperature of the phase transition [15]. In order to understand what is actually occurring at low temperatures in this material, a model that describes all of the contributions to the environment inhabited by the magnetic moments, including the crystal field, exchange interactions, and long-range magnetic dipolar interactions is required. The crystal field of $Yb_2Ti_2O_7$ has been determined experimentally in Refs. [19, 20], and the strength of the magnetic dipolar interactions are fixed by the fact that the Yb^{3+} ion is a $J = 7/2$ ion, leaving only the exchange interaction contribution to this model as an unknown. In this work we have set out, and as we have seen, succeeded, in determining a set of exchange interactions that successfully describe many experimentally observed properties of $Yb_2Ti_2O_7$.

The model we have chosen to describe the exchange interactions between the magnetic moments of the Yb^{3+} ions in $Yb_2Ti_2O_7$ includes all nearest-neighbour symmetry allowed bilinear exchange model which, on the pyrochlore lattice, consists of four terms. These

four terms can be expressed in many different ways, but the easiest form to understand is one that consists of local Ising exchange, isotropic exchange, pseudo-dipolar exchange, and Dzyaloshinskii-Moriya exchange. This model choice leaves us with four free parameters, which are the strengths of the four different types of exchange.

In order to determine the strengths of these four type of exchange interactions in $Yb_2Ti_2O_7$, we have performed a simulated annealing fit to quasi-elastic neutron scattering, which was collected well above the temperature of the experimentally observed phase transition. This neutron scattering data shows rods of scattering intensity along the [111] crystallographic direction, indicating the presence of interaction driven correlations between the Yb^{3+} magnetic moments, and making it an excellent quantity from which to determine the form of the magnetic interactions, as it is so highly featured. The fit to this data was performed by comparing random phase approximation (RPA) neutron scattering calculations performed using our proposed model to experimental observations of the neutron scattering intensity along cuts through the (h, k, k) plane. This difference was treated as an effective energy in a simulated annealing optimization of the strengths of the four interactions, along with a contribution to ensure agreement between the experimental and model Curie-Weiss temperatures. These calculations successfully determined two sets of exchange strengths, one for each crystal field parameterization used, that reproduce the experimental neutron scattering to a high degree of accuracy. Both of these models have ferromagnetic local Ising exchange as the energetically strongest interaction, which is interesting as this is opposite to the local planar nature of the crystal field ground state of $Yb_2Ti_2O_7$. The other three exchange terms are found to be approximately four times weaker than the local Ising exchange, but still energetically significant. The fact that the Dzyaloshinskii-Moriya interaction is so strong is interesting, as this interaction arises as a perturbative effect due to spin-orbit coupling in magnetic materials, making it typically very small. Recent work published in Ref. [52] has shown that such a large Dzyaloshinskii-Moriya interaction is in fact allowed in $Yb_2Ti_2O_7$. The set of interactions we have determined does suffer from some limitations. The model considered only takes into account bilinear exchange terms, while Yb^{3+} ions in $Yb_2Ti_2O_7$ are in fact $J = 7/2$ ions, which means that higher order exchange terms are allowed in this system. Our model is an "unprojected" full blown angular momentum, $\mathbf{J}$, form of an effective spin-1/2 model of the interactions in $Yb_2Ti_2O_7$. Effective spin-1/2 models involve "down projecting", projecting all of the interactions in the microscopic Hamiltonian, H_{mic}, into a Hilbert space spanned by the ground state doublet of the crystal field. Such a down projection is allowed because of the fact that the excited states of the crystal field are at significantly higher energies than those of the interactions, and also much larger than the temperature at which the neutron scattering was collected. This means our model is most likely only correct at low

energies, and not at energies on the scale of the crystal field splitting.

After successfully finding a set of exchange interactions capable of the describing the quasi-elastic neutron scattering of $Yb_2Ti_2O_7$, we then proceeded to use this model to compute the real space correlations generated by this model in an effort to understand how the rods of scattering intensity arise from our interaction model. The real space correlation function was computed by integrating the RPA susceptibility over the first Brillouin zone of the FCC lattice. The real space correlations were computed along three high symmetry directions on the pyrochlore lattice: the nearest-neighbour chain direction, the second nearest-neighbour direction, and the cubic unit cell body diagonal direction. We found that the correlations along the second nearest-neighbour and cubic unit cell body diagonal directions are weaker than the correlations along nearest-neighbour chains. This indicates that the rods are due to the presence of strong correlations along all of the nearest-neighbour chains in the pyrochlore lattice, not isotropic correlations within kagome planes in the pyrochlore lattice, as has been suggested in Ref. [40].

Finally we computed the bulk and local susceptibilities from our model using mean field and RPA methods. These calculations were compared to experimental measurements of these quantities reported in Refs. [19, 34]. We found good agreement between our model and experiment, but only using the crystal field parameterization of Ref. [19]. The crystal field parameterization of Ref. [20] resulted in a very poor fit to the experimental local susceptibility, so it was eliminated from any further consideration. The success of the anisotropic exchange model corresponding to the crystal field parameterization of Ref. [19] provides additional confirmation that our bilinear exchange model does indeed describe the magnetic interactions of $Yb_2Ti_2O_7$, at least at low energies. The model fails to fit the local susceptibility at high temperatures suggesting that the crystal field parameterization may incorrectly describe the excited crystal field states. The bulk susceptibility computed using our anisotropic exchange model was also found to fit experiment well at low temperatures.

With a Hamiltonian describing the magnetic interactions in $Yb_2Ti_2O_7$ now available, it should be possible to use it to better understand the low temperature phase of this material. We have presented some preliminary results aimed at determining the ground state of our model, using both classical Monte Carlo simulations and mean field calculations. These results show that the ground state is highly dependent on the presence of long-range magnetic dipolar interactions, suggesting that our model is highly susceptible to perturbations. This may indicate that quantum fluctuations or material disorder could destroy the ordered ground state of the classical spin-1/2 model, and lead to the experimentally observed fluctuating and disordered low temperature phase. This possibility means that calculations of the quantum fluctuations of the computed ground state may yield very interesting results. Further calculations to determine the nature of the phase transition of

this model are required, as calculations to date have failed to determine concretely whether this phase transition is first or second order. The possibility of an order-by-disorder phase transition in the case where long-range magnetic dipolar interactions are not present has been found, and further investigations of this transition are also required. The sensitivity of the ground state of our model for $Yb_2Ti_2O_7$ to small perturbations should also motivate investigations into the ground states of the more general local planar pyrochlore system. Various combinations of all of the possible symmetry allowed nearest-neighbour exchange interactions may yield very exotic phenomena.

APPENDICES

Appendix A

Crystal Field Parameterizations

This Appendix contains a detailed description of the CEF parameterizations of $Yb_2Ti_2O_7$ used in this study. Two such parameterizations are used, that of Hodges *et al.* from Ref. [20], described in Section A.1 and that of Cao *et al.* from Ref. [19], described in Section A.2. These crystal field parameterizations take the from

$$H_{\rm CF} = B_2^0 O_2^0 + B_4^0 O_4^0 + B_4^3 O_4^3 + B_6^0 O_6^0 + B_6^3 O_6^3 + B_6^6 O_6^6, \tag{A.1}$$

where O_n^m are Steven's operators, which are defined in Appendix B.

A.1 The Crystal Field of Hodges *et al.*

In this section we provide the details of the crystal field parameterization of Ref. [20]. This crystal field parameterization is based on ^{170}Yb Mössbauer spectroscopy, ^{170}Yb perturbed angular correlations, specific heat measurements, and magnetic susceptibility measurements [20]. The crystal field parameters determined based on these measurements are shown in Table A.1. Using these parameters $H_{\rm CF}$ can be diagonalized [63] to determine the energies and wave-functions of the crystal field states; these results are shown in Table A.2. It should be noted that the ground state doublet here is different to that published in the literature. Reference [61] indicates that the first term of the ground state wave-function in Ref. [20] should have a $\pm$ sign in front of it, and the small difference in the prefactor of the $|J = 7/2, J_z^a = +5/2\rangle$ and $|J = 7/2, J_z^a = -5/2\rangle$ terms is due to small differences in diagonalization results. As we can see in Table A.2, the separation between the ground state doublet and the first excited state doublet is very large, so that the low

temperature physics of $Yb_2Ti_2O_7$ will be governed by the ground state of this set of crystal field parameters. Because of this it is useful to compute the ground state matrix elements $\langle\psi_0^1|J_x^a|\psi_0^2\rangle$, $\langle\psi_0^1|J_y^a|\psi_0^2\rangle$, and $\langle\psi_0^1|J_z^a|\psi_0^1\rangle$. These matrix elements are used in the creation of the **g** tensor, used when projecting the system on to an effective spin-1/2 ground state, a useful technique when the behaviour of the system is governed by the doublet ground state. Performing this calculation, we find $\langle\psi_0^1|J_x^a|\psi_0^2\rangle = i\langle\psi_0^1|J_y^a|\psi_0^2\rangle = J_\perp = 1.83$ and $\langle\psi_0^1|J_z^a|\psi_0^1\rangle = J_\parallel = 0.772$, which can be used to determine the ground state **g** tensor of the Yb^{3+} ion via the equation [52]:

$$\mathbf{g} = \begin{pmatrix} 2g_J J_\perp & 0 & 0 \\ 0 & 2g_J J_\perp & 0 \\ 0 & 0 & 2g_J J_\parallel \end{pmatrix} \tag{A.2}$$

where g_J is the Landé factor for the Yb^{3+} ion, $g_J = 8/7$ [18]. This equation yields the following **g** tensor for the ground state of the Yb^{3+} ion in $Yb_2Ti_2O_7$ given in Table A.2:

$$\mathbf{g} = \begin{pmatrix} 4.18 & 0 & 0 \\ 0 & 4.18 & 0 \\ 0 & 0 & 1.76 \end{pmatrix} \tag{A.3}$$

Table A.1: Crystal Field Parameters for $Yb_2Ti_2O_7$ from References [19] and [20].

	B_2^0	B_4^0	B_4^3	B_6^0	B_6^3	B_6^6
Hodges *et al.* [20]	12.4K	−0.178K	−6.8K	0.021K	−0.14K	0.161K
Cao *et al.* [19]	11.9K	−0.509K	6.147K	0.006K	0.189K	0.098K

A.2 The Crystal Field of Cao *et al.*

In this section we provide details of the crystal field parameterization of Ref. [19]. This crystal field parameterization is based on rescaling the crystal field parameters of $Ho_2Ti_2O_7$, and fitting to the ^{170}Yb perturbed angular correlations of Ref. [20] as explained in Ref. [19]. The crystal field parameters determined using this method are shown in Table A.1. It should be noted that the crystal field in Ref. [19] is presented in a different notation from

Table A.2: The wave-functions and energies of the crystal field states of $Yb_2Ti_2O_7$ determined using the crystal field parameterization of Ref. [20]. $|\psi\rangle_n^m$ is the m^{th} degenerate wavefunction of the n^{th} energy state, which is given by summing all of the terms in the associated column. The quantization direction z is chosen to be along the local $\langle 111 \rangle$ direction at each sublattice site a.

	$\|\psi\rangle_0^1$	$\|\psi\rangle_0^2$	$\|\psi\rangle_1^1$	$\|\psi\rangle_1^2$	$\|\psi\rangle_2^1$	$\|\psi\rangle_2^2$	$\|\psi\rangle_3^1$	$\|\psi\rangle_3^2$
Energy (K)	0.0	0.0	621.08	621.08	732.97	732.97	943.50	943.50
$\|J = 7/2, J_z^a = -7/2\rangle$	0.0	−0.388	−0.010	−0.216	0.0	0.0	0.896	0.018
$\|J = 7/2, J_z^a = -5/2\rangle$	−0.245	0.0	0.912	−0.040	0.0	0.0	0.007	−0.326
$\|J = 7/2, J_z^a = -3/2\rangle$	0.0	0.0	0.0	0.0	−1.0	0.0	0.0	0.0
$\|J = 7/2, J_z^a = -1/2\rangle$	0.0	0.889	−0.015	−0.346	0.0	0.0	0.301	0.006
$\|J = 7/2, J_z^a = +1/2\rangle$	0.889	0.0	0.346	−0.015	0.0	0.0	−0.006	0.301
$\|J = 7/2, J_z^a = +3/2\rangle$	0.0	0.0	0.0	0.0	0.0	1.0	0.0	0.0
$\|J = 7/2, J_z^a = +5/2\rangle$	0.0	0.245	0.040	0.912	0.0	0.0	0.326	0.007
$\|J = 7/2, J_z^a = +7/2\rangle$	0.388	0.0	−0.216	0.010	0.0	0.0	0.018	−0.896

Ref. [20], that of irreducible tensor operators. The conversion between the two forms is performed by noting that in the notation of Ref. [19] and Ref. [20], $B_n^m = a_n A_n^m \langle r^n \rangle$, while in the unfortunately similar notation of Ref. [19], $B_n^m = d_n A_n^m \langle r^n \rangle$. The values of a_n can be found in Table 18 of Ref. [64], and the values of d_n can be found in Table 6-1 of Ref. [24]. As in the previous section, using these parameters, H_{CF} can be diagonalized to determine the energies and wavefunctions of the crystal field states, which are shown in Table A.3. Similar to the crystal field described by the parameterization of Ref. [20], the crystal field described by the parameterization of Ref. [19] has a ground state doublet well separated from the first excited state. Due to this, the low temperature physics of a system described by these crystal field parameters is governed by the ground state doublet. As before we compute the ground state matrix elements $\langle \psi_0^1 | J_x^a | \psi_0^2 \rangle$, $\langle \psi_0^1 | J_y^a | \psi_0^2 \rangle$, and $\langle \psi_0^1 | J_z^a | \psi_0^1 \rangle$ and the $\mathbf{g}$ tensor via Eqn. (A.2). Using the crystal field states of Table A.3, we find $\langle \psi_0^1 | J_x^a | \psi_0^2 \rangle = i \langle \psi_0^1 | J_y^a | \psi_0^2 \rangle = J_\perp = 1.74$, $\langle \psi_0^1 | J_z^a | \psi_0^1 \rangle = J_\parallel = 0.982$, and

$$\mathbf{g} = \begin{pmatrix} 3.98 & 0 & 0 \\ 0 & 3.98 & 0 \\ 0 & 0 & 2.24 \end{pmatrix}. \tag{A.4}$$

With all of the wave-functions for the crystal field of the Yb^{3+} ion for both crystal field parameterizations, our description of H_{CF} is complete.

Table A.3: The wave-functions and energies of the crystal field states of $Yb_2Ti_2O_7$ determined using the crystal field parameterization of Ref. [19]. $|\psi\rangle_n^m$ is the m^{th} degenerate wavefunction of the n^{th} energy state, which is given by summing all of the terms in the associated column. The quantization direction z is chosen to be along the local $\langle 111 \rangle$ direction at each sublattice site a.

	$\|\psi\rangle_0^1$	$\|\psi\rangle_0^2$	$\|\psi\rangle_1^1$	$\|\psi\rangle_1^2$	$\|\psi\rangle_2^1$	$\|\psi\rangle_2^2$	$\|\psi\rangle_3^1$	$\|\psi\rangle_3^2$
Energy (K)	0.0	0.0	693.07	693.07	796.82	796.82	1051.02	1051.02
$\|J = 7/2, J_z^a = -7/2\rangle$	0.0	0.411	0.0	0.0	−0.873	0.0	0.0	0.263
$\|J = 7/2, J_z^a = -5/2\rangle$	0.089	0.0	0.0	0.0	0.0	0.249	0.964	0.0
$\|J = 7/2, J_z^a = -3/2\rangle$	0.0	0.0	−0.438	−0.899	0.0	0.0	0.0	0.0
$\|J = 7/2, J_z^a = -1/2\rangle$	0.0	0.907	0.0	0.0	0.420	0.0	0.0	−0.025
$\|J = 7/2, J_z^a = +1/2\rangle$	0.907	0.0	0.0	0.0	0.0	−0.420	0.025	0.0
$\|J = 7/2, J_z^a = +3/2\rangle$	0.0	0.0	0.899	−0.438	0.0	0.0	0.0	0.0
$\|J = 7/2, J_z^a = +5/2\rangle$	0.0	−0.089	0.0	0.0	0.249	0.0	0.0	0.964
$\|J = 7/2, J_z^a = +7/2\rangle$	−0.411	0.0	0.0	0.0	0.0	−0.873	0.264	0.0

Appendix B

The Stevens-operator Equivalents Required to Describe the Crystal Field of $Yb_2Ti_2O_7$

This appendix provides the operator equivalent definitions of the Steven's operators [64], used to define the crystal field of $Yb_2Ti_2O_7$. The crystal field of $Yb_2Ti_2O_7$ is defined as:

$$H_{\mathrm{CF}} = B_0^2 O_0^2 + B_0^4 O_0^4 + B_3^4 O_3^4 + B_0^6 O_0^6 + B_3^6 O_3^6 + B_6^6 O_6^6, \tag{B.1}$$

where B_m^n are coefficients, given in Table A.1. O_m^n are Steven's operators, defined as [64]:

$$O_2^0 = 3\left(J_z^a\right)^2 - J^a\left(J^a+1\right) \tag{B.2}$$

$$\begin{aligned} O_4^0 = {} & 35\left(J_z^a\right)^4 - 30J^a\left(J^a+1\right)\left(J_z^a\right)^2 + 25\left(J_z^a\right)^2 \\ & - 6J^a\left(J^a+1\right) + 3\left(J^a\right)^2\left(J^a+1\right)^2 \end{aligned} \tag{B.3}$$

$$O_4^3 = \frac{1}{2}\left\{J_z^a\left(J_+^a + J_-^a\right)\right\}_S \tag{B.4}$$

$$\begin{aligned} O_6^0 = {} & 231\left(J_z^a\right)^6 - 315J^a\left(J^a+1\right)\left(J_z^a\right)^4 + 735\left(J_z^a\right)^4 \\ & + 105\left(J^a\right)^2\left(J^a+1\right)^2\left(J_z^a\right)^2 - 525J^a\left(J^a+1\right)\left(J_z^a\right)^2 \\ & + 294\left(J_z^a\right)^2 - 5\left(J^a\right)^3\left(J^a+1\right)^3 + 40\left(J^a\right)^2\left(J^a+1\right)^2 \\ & - 60J^a\left(J^a+1\right) \end{aligned} \tag{B.5}$$

$$O_6^3 = \frac{1}{2}\left\{\left(11\left(J_z^a\right)^3 - J^a\left(J^a+1\right)J_z^a - 59J_z^a\right)\left(\left(J_+^a\right)^3 + \left(J_-^a\right)^3\right)\right\}_S \tag{B.6}$$

$$O_6^6 = \frac{1}{2}\left(\left(J_+^a\right)^6 + \left(J_-^a\right)^6\right), \tag{B.7}$$

where $\{AB\}_S = \frac{1}{2}(AB + BA)$ [64]. The a superscript denotes the use of the local $\langle 111 \rangle$ direction for the a sublattice site as the quantization direction for the total angular momentum J.

Appendix C

Symmetry Allowed Exchange Interactions on the Pyrochlore Lattice

To describe the exchange interactions present in $Yb_2Ti_2O_7$ we propose that H_{ex} contains all the symmetry allowed nearest-neighbour bilinear exchange interactions on the pyrochlore lattice. These are exchange interactions whose form remains unchanged under the symmetry operations of the pyrochlore lattice, which is described by the $Fd\bar{3}m$ (O_h^7) space group [7] and the O_h point group. The space group describes all of the operations that leave the lattice structure unchanged including translations, while the point group considers only rotation, inversion, and reflection operations.

C.1 Deriving the Symmetry Allowed Exchange Interactions

In order to determine the number of independent symmetry allowed interactions that make up $\overline{\overline{\mathcal{J}}}$ (Eqn. (2.5)) and determine the form of these interactions, we must first understand some basic representation theory. The O_h point group is made up of symmetry operations such as rotation and reflection, but not translation, that transform the lattice structure into itself. These operations are broken up into classes, groups of operations that when written in matrix form can be transformed into one another by a third symmetry operation in the group [65]. The symmetry operations A and B are members of the same class if

there exists a third symmetry operation C such that $C^{-1}AC = B$. A representation Γ is the set of matrices $\{\mathbf{D}(R)\}$ that perform all of the symmetry operations $\{R\}$ of a group [65]. A very useful property of the matrices $\{\mathbf{D}(r)\}$ is that their trace, or character ($\chi(R)$) as it is called in representation theory, does not change depending on the coordinate system chosen for the representation, and every matrix $\mathbf{D}(R)$ in a class has the same character. One final useful aspect of representation theory is the idea of an irreducible representation. A representation is said to be reducible if there exists a similarity transform that transforms all of the matrices of the representation into the same block diagonal form [65]. A representation where this is not possible is said to be irreducible. The characters of all of the symmetry operations of a group for all of irreducible representations are given in character tables, such the the O_h character table shown in Table C.1.

The first step in determining the number of independent symmetry allowed nearest-neighbour bilinear exchange interactions on the pyrochlore lattice is to define the order of the group (Eqn. 3-10 in Ref.[65]),

$$h = \sum_{\alpha} l_{\alpha}. \tag{C.1}$$

l_{α} is the dimensionality of the α^{th} irreducible representation, which is identical to the character of the identity symmetry operation E for the α^{th} irreducible representation [65]. We must also define m_{α}, the number of times the α^{th} irreducible representation appears in the decomposition of a reducible representation. This quantity is given by (Eqn. 3-12 in Ref. [65])

$$m_{\alpha} = \frac{1}{h} \sum_{\alpha} \chi^{\alpha}(R)\chi^{*}(R), \tag{C.2}$$

where $\chi^{\alpha}(R)$ is the character of the symmetry operation R in the α^{th} irreducible representation, and $\chi^{*}(R)$ is the character of the symmetry operation R in the representation we seek to decompose [65].

Now we may define our chosen representation, Γ, in which to compute the form of the symmetry allowed interactions. We chose the representation consisting of all of the possible bilinear interactions between the various cartesian components of the $\mathbf{J}$ angular momenta at the four sublattice sites:

$$\Gamma = \sum_{a \neq b, u, v} J_u^a J_v^b, \tag{C.3}$$

where u and v are the cartesian components x, y, and z. Γ encompasses all of the possible nearest neighbour interactions that may be contained in H_{ex}. In this representation, assuming that the interaction matrix is symmetric, that is $J_u^a J_v^b = J_v^b J_u^a$, there are 54 independent components in the representation, thus Γ has a dimensionality of 54. Now we

require $\chi(R)$ for all of the symmetry operations of the group O_h in this representation. The easiest character to compute is that of the identity operation E, which trivially has a character of 54. The characters of the other operations are more difficult to compute. In the order of Table C.1, the symmetry operations of the O_h point group are [65]:

- E, The identity transformation,
- C_3, $2\pi/3$ rotation about the $\langle 111 \rangle$ cubic body diagonals,
- C_2', π rotation about the $\hat{x}+\hat{y}$, $\hat{x}+\hat{z}$, and $\hat{y}+\hat{z}$ directions,
- C_4, $\pi/2$ rotation about the cartesian $\hat{x}$, $\hat{y}$, and $\hat{z}$ directions,
- C_2, π rotation operation about the $\hat{x}$, $\hat{y}$, and $\hat{z}$ directions,
- i, The inversion operator that swaps x to $-x$, y to $-y$, and z to $-z$,
- S_4, $\pi/2$ rotation about the $\hat{x}$, $\hat{y}$, and $\hat{z}$ directions accompanied by a reflection in through the plane perpendicular to these directions,
- S_6, $\pi/3$ rotation about the $\langle 111 \rangle$ cubic body diagonals accompanied by a ref reflection in through the plane perpendicular to these directions,
- σ_h, reflection through the planes normal to the C_4 rotation directions,
- σ_d, reflection though the planes normal to the C'$_2$ rotation directions.

Understanding exactly how these operations act on Γ is not a trivial process, but there are some symmetry relations that make it easier to understand how the elements of Γ will transform into one another under these symmetry operations. These relations will also simplify the computation of the character of each of the symmetry operations in this representation. These symmetry relations revolve around the idea that, in Table C.1, all of the symmetry operations in the columns to the right of the inversion operation are operations to the left of the inversion operation, combined with inversion. In fact the inversion operator itself can be thought of as the identity operator combined with inversion [65]. It should be noted that the symmetry operations that result from the combination of inversion with the elements E, C_3, C_2', C_4, and C_2 are not in the same order as these operations. The symmetry relationships are i=i$\otimes$E, S_4 =i$\otimes C_4$, S_6 =i$\otimes C_3$, σ_h =i$\otimes C_2$, and σ_d =i$\otimes C_2'$. This means that once we know how one symmetry operation acts on Γ, we simply invert it and automatically generate another symmetry operation. Another

useful relation is that the character of symmetry operations related by inversion are either identical, or multiplied by -1 depending on whether a representation is odd or even under inversion. In the case of Γ, as inversion maps all four sub-lattices to themselves and because all the terms are bilinear, the inversion of the coordinate system is cancelled out.

Table C.1: The character table of the O_h point group [65]. The rows give the characters of the various irreducible representations, while the columns label the symmetry operations.

	E	$8C_3$	$6C_2'$	$6C_4$	$3C_2$	i	$6S_4$	$8S_6$	$3\sigma_h$	$6\sigma_d$
A_{1g}	1	1	1	1	1	1	1	1	1	1
A_{2g}	1	1	-1	-1	1	1	-1	1	1	-1
E_g	2	-1	0	0	2	2	0	-1	2	0
T_{1g}	3	0	-1	1	-1	3	1	0	-1	-1
T_{2g}	3	0	1	-1	-1	3	-1	0	-1	1
A_{1u}	1	1	1	1	1	-1	-1	-1	-1	-1
A_{2u}	1	1	-1	-1	1	-1	1	-1	-1	1
E_u	2	-1	0	0	2	-2	0	1	-2	0
T_{1u}	3	0	-1	1	-1	-3	-1	0	1	1
T_{2u}	3	0	1	-1	-1	-3	1	0	1	-1

Table C.2: The characters of the symmetry operations of the O_h point group in the representation Γ.

	E	$8C_3$	$6C_2'$	$6C_4$	$3C_2$	i	$6S_4$	$8S_6$	$3\sigma_h$	$6\sigma_d$
Γ	54	0	2	0	10	54	0	0	10	2

The precise action of each of the symmetry operations of the O_h symmetry group on the elements of Γ are given in Appendix D. If we define a vector space with dimension 54, one independent dimension for each independent element in Γ, we can write all of the symmetry operations in Γ as 54×54 matrices. The elements of these matrices describe how the components of Γ transform into each other under the various symmetry operations of the O_h point group. For example, under the identity operation, E, all of the elements of Γ

transform into themselves, so the matrix representation of E is simply a 54×54 identity matrix. The character of this or any other symmetry operation is then determined by taking the trace of the matrix representation of the symmetry operation. The characters of all of the symmetry operations in the representation Γ, computed using this method, are given in Table C.2.

Now that we know the character of all of the symmetry operations in O_h for the reducible representation Γ, we can use Eq. (C.2) to decompose Γ into a combination of irreducible representations. Using the characters of the symmetry operations of the point group O_h for all of the irreducible representations of O_h given in Table C.1, and the characters of the symmetry operations in the representation Γ given in Table C.2, we can compute the number of times each of the irreducible representations appears in Γ. Performing this decomposition we obtaining the result

$$\Gamma = 4A_{1g} \oplus 3A_{2g} \oplus 7E_g \oplus 5T_{1g} \oplus 6T_{2g}. \tag{C.4}$$

The irreducible representation A_{1g} is the irreducible representation where all of the symmetry operations leave the elements unchanged, as the character of all of the symmetry operations in the representation are identical. The fact that A_{1g} appears four times in Γ means that Γ contains four sets of elements that will be left unchanged under all of the symmetry operations of O_h. These sets are referred to as symmetry invariant.

In order to determine what these four sets of elements are, we must turn to the concept of symmetry coordinates in representation theory. Symmetry coordinates are n-dimensional hyper-vectors containing combinations of the elements of a chosen representation that when acted on by any symmetry operation of a group, transform in simple ways [65]. Specifically, for a one dimensional irreducible representation like A_{1g}, the symmetry coordinates will be transformed into themselves multiplied by a constant, the character of the given symmetry operation [65]. The method for determining the symmetry coordinates for a given irreducible representation that appears in the decomposition of a reducible representation is called the projector method. In this method, a projector is defined as (Eqn. 3-16 in Ref. [65])

$$P^{(\gamma)} \propto \sum_R \chi^{(\gamma)}(R)^* O_R, \tag{C.5}$$

where γ is the chosen irreducible representation and $\{R\}$ are all of the symmetry operations of the group. $\chi^{(\gamma)}(R)^*$ is the complex conjugate of the character of the symmetry operation R in the irreducible representation γ and O_R is the operator that transforms a hyper-vector into the form it would take after the symmetry operation R [65]. The proportionality symbol is introduced by the desire to have normalized and orthogonal symmetry coordinates.

As we are only concerned with the irreducible representation A_{1g}, the characters of all of the symmetry operations are 1, so Eqn. (C.5) simplifies to

$$P^{(A_{1g})} \propto \sum_R O_R. \tag{C.6}$$

The simplest way to use $P^{(A_{1g})}$ to determine the symmetry coordinates for A_{1g} of Γ is to chose one element of Γ and operate $P^{(A_{1g})}$ on it to determine what elements of Γ are contained in the resulting symmetry coordinate. This is repeated, choosing an element of Γ that is not in the previous symmetry coordinate, operating $P^{(A_{1g})}$ on this element, and repeating this process until all of the elements of Γ are accounted for. Performing this operation yields the following symmetry coordinates for the irreducible representation A_{1g} of the representation Γ, which we will refer to as $\{\mathcal{X}_n\}$:

$$\begin{aligned}\mathcal{X}_1 = {} & J_x^1 J_x^2 + J_y^1 J_y^2 + J_x^1 J_x^3 + J_z^1 J_z^3 + J_y^1 J_y^4 + J_z^1 J_z^4 \\ & + J_y^2 J_y^3 + J_z^2 J_z^3 + J_x^2 J_x^4 + J_z^2 J_z^4 + J_x^3 J_x^4 + J_y^3 J_y^4\end{aligned} \tag{C.7}$$

$$\mathcal{X}_2 = J_z^1 J_z^2 + J_y^1 J_y^3 + J_x^1 J_x^4 + J_x^2 J_x^3 + J_y^2 J_y^4 + J_z^3 J_z^4 \tag{C.8}$$

$$\begin{aligned}\mathcal{X}_3 = {} & J_x^1 J_y^2 + J_y^1 J_x^2 + J_x^1 J_z^3 + J_z^1 J_x^3 + J_y^1 J_z^4 + J_z^1 J_y^4 \\ & - J_y^2 J_z^3 - J_z^2 J_y^3 - J_x^2 J_z^4 - J_z^2 J_x^4 - J_x^3 J_y^4 - J_y^3 J_x^4\end{aligned} \tag{C.9}$$

$$\begin{aligned}\mathcal{X}_4 = {} & J_x^1 J_z^2 + J_y^1 J_z^2 - J_z^1 J_x^2 - J_z^1 J_y^2 + J_x^1 J_y^3 + J_z^1 J_y^3 \\ & - J_y^1 J_z^3 - J_y^1 J_x^3 + J_y^1 J_x^4 + J_z^1 J_x^4 - J_x^1 J_z^4 - J_x^1 J_y^4 \\ & + J_x^2 J_z^3 + J_y^2 J_z^3 - J_x^2 J_y^3 - J_z^2 J_x^3 + J_x^2 J_y^4 + J_y^2 J_z^4 \\ & - J_y^2 J_x^4 - J_z^2 J_y^4 + J_x^3 J_z^4 + J_z^3 J_y^4 - J_y^3 J_z^4 - J_z^3 J_x^4.\end{aligned} \tag{C.10}$$

These symmetry coordinates are one form of the four symmetry allowed exchange interactions on the pyrochlore lattice. Examining $\{\mathcal{X}_n\}$, we can see that they are identical to the invariants defined as χ_n in Ref. [66] (we choose not to use χ here, as it is used to denote the magnetic susceptibility). We can cast these symmetry coordinates in a form that allows for the construction of the interaction matrix $\overline{\overline{\mathcal{J}}}$ (Eqn. (2.5)), by writing each of them as an implicitly defined 12×12 matrix, where each term in Eqns. (C.7)-(C.10) is replaced with $+1$ or -1 at the appropriate location in the matrix. The resulting matrix forms of

$\{\mathcal{X}_n\}$ are given by:

$$\overline{\overline{\mathcal{X}}}_1 = \begin{pmatrix} 0 & 0 & 0 & 1 & 0 & 0 & 1 & 0 & 0 & 0 & 0 & 0 \\ 0 & 0 & 0 & 0 & 1 & 0 & 0 & 0 & 0 & 0 & 1 & 0 \\ 0 & 0 & 0 & 0 & 0 & 0 & 0 & 0 & 1 & 0 & 0 & 1 \\ 1 & 0 & 0 & 0 & 0 & 0 & 0 & 0 & 0 & 1 & 0 & 0 \\ 0 & 1 & 0 & 0 & 0 & 0 & 0 & 1 & 0 & 0 & 0 & 0 \\ 0 & 0 & 0 & 0 & 0 & 0 & 0 & 0 & 1 & 0 & 0 & 1 \\ 1 & 0 & 0 & 0 & 0 & 0 & 0 & 0 & 0 & 1 & 0 & 0 \\ 0 & 0 & 0 & 0 & 1 & 0 & 0 & 0 & 0 & 0 & 1 & 0 \\ 0 & 0 & 1 & 0 & 0 & 1 & 0 & 0 & 0 & 0 & 0 & 0 \\ 0 & 0 & 0 & 1 & 0 & 0 & 1 & 0 & 0 & 0 & 0 & 0 \\ 0 & 1 & 0 & 0 & 0 & 0 & 0 & 1 & 0 & 0 & 0 & 0 \\ 0 & 0 & 1 & 0 & 0 & 1 & 0 & 0 & 0 & 0 & 0 & 0 \end{pmatrix}, \tag{C.11}$$

$$\overline{\overline{\mathcal{X}}}_2 = \begin{pmatrix} 0 & 0 & 0 & 0 & 0 & 0 & 0 & 0 & 0 & 1 & 0 & 0 \\ 0 & 0 & 0 & 0 & 0 & 0 & 0 & 1 & 0 & 0 & 0 & 0 \\ 0 & 0 & 0 & 0 & 0 & 1 & 0 & 0 & 0 & 0 & 0 & 0 \\ 0 & 0 & 0 & 0 & 0 & 0 & 1 & 0 & 0 & 0 & 0 & 0 \\ 0 & 0 & 0 & 0 & 0 & 0 & 0 & 0 & 0 & 0 & 1 & 0 \\ 0 & 0 & 1 & 0 & 0 & 0 & 0 & 0 & 0 & 0 & 0 & 0 \\ 0 & 0 & 0 & 1 & 0 & 0 & 0 & 0 & 0 & 0 & 0 & 0 \\ 0 & 1 & 0 & 0 & 0 & 0 & 0 & 0 & 0 & 0 & 0 & 0 \\ 0 & 0 & 0 & 0 & 0 & 0 & 0 & 0 & 0 & 0 & 0 & 1 \\ 1 & 0 & 0 & 0 & 0 & 0 & 0 & 0 & 0 & 0 & 0 & 0 \\ 0 & 0 & 0 & 0 & 1 & 0 & 0 & 0 & 0 & 0 & 0 & 0 \\ 0 & 0 & 0 & 0 & 0 & 0 & 0 & 0 & 1 & 0 & 0 & 0 \end{pmatrix}, \tag{C.12}$$

$$\overline{\overline{\mathcal{X}}}_3 = \begin{pmatrix} 0 & 0 & 0 & 0 & 1 & 0 & 0 & 0 & 1 & 0 & 0 & 0 \\ 0 & 0 & 0 & 1 & 0 & 0 & 0 & 0 & 0 & 0 & 0 & 1 \\ 0 & 0 & 0 & 0 & 0 & 0 & 1 & 0 & 0 & 0 & 1 & 0 \\ 0 & 1 & 0 & 0 & 0 & 0 & 0 & 0 & 0 & 0 & 0 & -1 \\ 1 & 0 & 0 & 0 & 0 & 0 & 0 & 0 & -1 & 0 & 0 & 0 \\ 0 & 0 & 0 & 0 & 0 & 0 & 0 & -1 & 0 & -1 & 0 & 0 \\ 0 & 0 & 1 & 0 & 0 & 0 & 0 & 0 & 0 & 0 & -1 & 0 \\ 0 & 0 & 0 & 0 & 0 & -1 & 0 & 0 & 0 & -1 & 0 & 0 \\ 1 & 0 & 0 & 0 & -1 & 0 & 0 & 0 & 0 & 0 & 0 & 0 \\ 0 & 0 & 0 & 0 & 0 & -1 & 0 & -1 & 0 & 0 & 0 & 0 \\ 0 & 0 & 1 & 0 & 0 & 0 & -1 & 0 & 0 & 0 & 0 & 0 \\ 0 & 1 & 0 & -1 & 0 & 0 & 0 & 0 & 0 & 0 & 0 & 0 \end{pmatrix}, \tag{C.13}$$

and

$$\overline{\overline{\mathcal{X}}}_4 = \begin{pmatrix} 0 & 0 & 0 & 0 & 0 & 1 & 0 & 1 & 0 & 0 & -1 & -1 \\ 0 & 0 & 0 & 0 & 0 & 1 & -1 & 0 & -1 & 1 & 0 & 0 \\ 0 & 0 & 0 & -1 & -1 & 0 & 0 & 1 & 0 & 1 & 0 & 0 \\ 0 & 0 & -1 & 0 & 0 & 0 & 0 & -1 & 1 & 0 & 1 & 0 \\ 0 & 0 & -1 & 0 & 0 & 0 & 1 & 0 & 0 & -1 & 0 & 1 \\ 1 & 1 & 0 & 0 & 0 & 0 & -1 & 0 & 0 & 0 & -1 & 0 \\ 0 & -1 & 0 & 0 & 1 & -1 & 0 & 0 & 0 & 0 & 0 & 1 \\ 1 & 0 & 1 & -1 & 0 & 0 & 0 & 0 & 0 & 0 & 0 & -1 \\ 0 & -1 & 0 & 1 & 0 & 0 & 0 & 0 & 0 & -1 & 1 & 0 \\ 0 & 1 & 1 & 0 & -1 & 0 & 0 & 0 & -1 & 0 & 0 & 0 \\ -1 & 0 & 0 & 1 & 0 & -1 & 0 & 0 & 1 & 0 & 0 & 0 \\ -1 & 0 & 0 & 0 & 1 & 0 & 1 & -1 & 0 & 0 & 0 & 0 \end{pmatrix}. \tag{C.14}$$

A linear combination of these matrices will define all of the symmetry allowed nearest neighbour interactions, so that the symmetry allowed form of $\overline{\overline{\mathcal{J}}}$ is

$$\overline{\overline{\mathcal{J}}} = -\mathcal{J}_1\overline{\overline{\mathcal{X}_1}} - \mathcal{J}_2\overline{\overline{\mathcal{X}_2}} - \mathcal{J}_3\overline{\overline{\mathcal{X}_3}} - \mathcal{J}_4\overline{\overline{\mathcal{X}_4}}. \tag{C.15}$$

$\{\mathcal{J}_n\} = \{\mathcal{J}_1, \mathcal{J}_2, \mathcal{J}_3, \mathcal{J}_4\}$ are the coupling energies of each of the four symmetry allowed nearest neighbour exchange terms.

C.2 Other Representations of the Symmetry Allowed Nearest Neighbour Interactions

Now that we have determined the form of the symmetry allowed nearest-neighbour interactions, we can examine other representations of these interactions that are easier to understand physically. As the symmetry allowed exchange interactions we found in Chapter C.1 are invariant under all of the symmetry operations of the O_h point group, any linear combinations of these interactions will also be invariant under the symmetry operations of O_h. This means that we are free to choose any form we want for the nearest neighbour interactions, so long as it has four linearly independent terms that consist only of linear combinations of the terms in $\{\mathcal{X}_n\}$. Reference [66] gives us one possible representation (denoted X_n), which is in terms of the local crystal field coordinate system, defined in

Table 1.3 of Chapter 1.4. In Ref. [66] we are given the relationship between $\{X_n\}$, and two terms of $\mathcal{X}_n$, the other relationships are provided by Ref. [67] and are:

$$\mathcal{X}_1 = 2X_1 + \frac{1}{2}X_2 + \frac{1}{2}X_3 + 2X_4 \tag{C.16}$$

$$\mathcal{X}_2 = -X_1 + \frac{1}{2}X_2 + \frac{1}{2}X_3 - X_4 \tag{C.17}$$

$$\mathcal{X}_3 = 2X_1 + \frac{1}{2}X_2 - X_3 - X_4 \tag{C.18}$$

$$\mathcal{X}_4 = -4X_1 + \frac{1}{2}X_2 - X_3 + 2X_4. \tag{C.19}$$

The invariants $\{X_n\}$ are given by (Table 1 in Ref. [66]):

$$X_1 = -\frac{1}{3}J_1^z J_2^z - \frac{1}{3}J_1^z J_3^z - \frac{1}{3}J_1^z J_4^z - \frac{1}{3}J_2^z J_3^z - \frac{1}{3}J_2^z J_4^z - \frac{1}{3}J_3^z J_4^z \tag{C.20}$$

$$\begin{aligned} X_2 = &-\frac{\sqrt{2}}{3}\left(J_1^z J_2^+ + J_1^+ J_2^z\right) - \frac{\sqrt{2}}{3}\left(J_1^z J_2^- + J_1^- J_2^z\right) \\ &- \frac{\sqrt{2}}{3}\epsilon\left(J_1^z J_3^+ + J_1^+ J_3^z\right) - \frac{\sqrt{2}}{3}\epsilon^*\left(J_1^z J_3^- + J_1^- J_3^z\right) \\ &- \frac{\sqrt{2}}{3}\epsilon^*\left(J_1^z J_4^+ + J_1^+ J_4^z\right) - \frac{\sqrt{2}}{3}\epsilon\left(J_1^z J_4^- + J_1^- J_4^z\right) \\ &- \frac{\sqrt{2}}{3}\epsilon^*\left(J_2^z J_3^+ + J_2^+ J_3^z\right) - \frac{\sqrt{2}}{3}\epsilon\left(J_2^z J_3^- + J_2^- J_3^z\right) \\ &- \frac{\sqrt{2}}{3}\epsilon\left(J_2^z J_4^+ + J_2^+ J_4^z\right) - \frac{\sqrt{2}}{3}\epsilon^*\left(J_2^z J_4^- + J_2^- J_4^z\right) \\ &- \frac{\sqrt{2}}{3}\left(J_3^z J_4^+ + J_3^+ J_4^z\right) - \frac{\sqrt{2}}{3}\left(J_3^z J_4^- + J_3^- J_4^z\right) \end{aligned} \tag{C.21}$$

$$\begin{aligned} X_3 = &\frac{1}{3}J_1^+ J_2^+ + \frac{1}{3}J_1^- J_2^- + \epsilon^* J_1^+ J_3^+ + \epsilon J_1^- J_3^- + \epsilon J_1^+ J_4^+ + \epsilon^* J_1^- J_4^- \\ &+ \epsilon J_2^+ J_3^+ + \epsilon^* J_2^- J_3^- + \epsilon^* J_2^+ J_4^+ + \epsilon J_2^- J_4^- + \frac{1}{3}J_3^+ J_4^+ + \frac{1}{3}J_3^- J_4^- \end{aligned} \tag{C.22}$$

$$\begin{aligned} X_4 = &-\frac{1}{6}J_1^+ J_2^- - \frac{1}{6}J_1^- J_2^+ - \frac{1}{6}J_1^+ J_3^- - \frac{1}{6}J_1^- J_3^+ - \frac{1}{6}J_1^+ J_4^- - \frac{1}{6}J_1^- J_4^+ \\ &- \frac{1}{6}J_2^+ J_3^- - \frac{1}{6}J_2^- J_3^+ - \frac{1}{6}J_2^+ J_4^- - \frac{1}{6}J_2^- J_4^+ - \frac{1}{6}J_3^+ J_4^- - \frac{1}{6}J_3^- J_4^+. \end{aligned} \tag{C.23}$$

In this representation of the invariants, J_a^α and J_b^β, where $\alpha, \beta = z, +, -$, are expressed in local quantization coordinates as opposed to the global cartesian coordinates used in the

$\{\mathcal{X}_n\}$ representation. $J_a^+ = J_a^x + iJ_a^y$ and $J_a^+ = J_a^x - iJ_a^y$ are the conventional raising and lowering operators, and $\epsilon = \exp(2\pi i/3)$ is a phase factor.

The conversion between various forms of the symmetry allowed nearest neighbour interactions lends itself well to matrix representation. If $\overline{\mathcal{X}}$ is the column vector made up of the $\{\mathcal{X}_n\}$ form of the symmetry allowed nearest-neighbour interactions, defined as

$$\overline{\mathcal{X}} = \begin{pmatrix} \mathcal{X}_1 \\ \mathcal{X}_2 \\ \mathcal{X}_3 \\ \mathcal{X}_4 \end{pmatrix}, \tag{C.24}$$

and $\overline{X}$ is the column vector representation of the $\{X_n\}$ form of the same interactions, defined as

$$\overline{X} = \begin{pmatrix} X_1 \\ X_2 \\ X_3 \\ X_4 \end{pmatrix}, \tag{C.25}$$

then we can relate the two representations via the equation

$$\overline{\mathcal{X}} = \overline{\overline{W}}\ \overline{X}, \tag{C.26}$$

where $\overline{\overline{W}}$ is a matrix with the coefficients of Eqns. C.16-C.19 in the rows. This form of the relation between $\mathcal{X}_n$ and X_n is also very useful in that it allows for convenient relation of the coupling terms of the Hamiltonian as well. If we define H_{ex} as

$$H_{\text{ex}} = -\mathcal{J}_1\mathcal{X}_1 - \mathcal{J}_2\mathcal{X}_2 - \mathcal{J}_3\mathcal{X}_3 - \mathcal{J}_4\mathcal{X}_4, \tag{C.27}$$

this can be written as

$$H_{\text{ex}} = -\overline{\mathcal{J}}^T\ \overline{\mathcal{X}}, \tag{C.28}$$

where $\overline{\mathcal{J}}$ is the column vector made up of the elements of $\{\mathcal{J}_n\}$, defined as

$$\overline{\mathcal{J}} = \begin{pmatrix} \mathcal{J}_1 \\ \mathcal{J}_2 \\ \mathcal{J}_3 \\ \mathcal{J}_4 \end{pmatrix}. \tag{C.29}$$

Equivalently, we could write

$$H_{\text{ex}} = -J_1 X_1 - J_2 X_2 - J_3 X_4 - J_4 X_4, \tag{C.30}$$

which has the vector form

$$H_{\text{ex}} = -\overline{J}^T \, \overline{X}, \tag{C.31}$$

where

$$\overline{J} = \begin{pmatrix} J_1 \\ J_2 \\ J_3 \\ J_4 \end{pmatrix}. \tag{C.32}$$

Then, using Eqn. (C.26), we can write

$$H_{\text{ex}} = -\overline{\mathcal{J}}^T \, \mathcal{X} \tag{C.33}$$

$$= -\overline{\mathcal{J}}^T \, \overline{\overline{W}} \, \overline{X} \tag{C.34}$$

$$= -\overline{J}^T \, \overline{X}, \tag{C.35}$$

arriving at the relationship

$$\overline{J}^T = \overline{\mathcal{J}}^T \, \overline{\overline{W}}, \tag{C.36}$$

which provides us with a very convenient method of converting between the coupling energies of various representations of the symmetry allowed nearest neighbour interactions.

One particular representation that will be very useful is the "physically motivated" representation. This representation is made of up of exchange terms commonly seen in physics literature instead of the rather arbitrary terms in X_n and $\mathcal{X}_n$. In this representation, we define the nearest neighbour interaction Hamiltonian as

$$H_{\text{ex}} = H_{\text{Ising}} + H_{\text{iso}} + H_{\text{pd}} + H_{\text{DM}}. \tag{C.37}$$

$$H_{\text{Ising}} = -\mathcal{J}_{\text{Ising}} \sum_{<i,j;a,b>} \left(\mathbf{J}_i^a \cdot \hat{\mathbf{z}}^a\right) \left(\mathbf{J}_j^b \cdot \hat{\mathbf{z}}^b\right), \tag{C.38}$$

is the nearest neighbour local [111] Ising interaction on the pyrochlore lattice.

$$H_{\text{iso}} = -\mathcal{J}_{\text{iso}} \sum_{<i,j;a,b>} \mathbf{J}_i^a \cdot \mathbf{J}_j^b, \tag{C.39}$$

is isotropic nearest neighbour exchange, and

$$H_{\rm pd} = -\mathcal{J}_{\rm pd} \sum_{<i,j;a,b>} (\mathbf{J}_i^a \cdot \mathbf{J}_j^b - 3(\mathbf{J}_i^a \cdot \hat{\mathbf{R}}_{ij}^{ab})(\mathbf{J}_j^b \cdot \hat{\mathbf{R}}_{ij}^{ab})), \tag{C.40}$$

is pseudo-dipolar exchange. This interaction is physically unrelated to the long-range magnetic dipolar interaction, but has the same mathematical form.

$$H_{\rm DM} = -\mathcal{J}_{\rm DM} \sum_{<i,j;a,b>} \mathbf{\Omega}_{\rm DM}^{a,b} \cdot \left(\mathbf{J}_i^a \times \mathbf{J}_j^b\right), \tag{C.41}$$

is the Dzyaloshinskii-Moriya (DM) interaction on the pyrochlore lattice [51]. In all of these terms, a and b are the tetrahedral sublattice sites of the pyrochlore lattice, while i and j are FCC lattice sites. The vectors $\hat{\mathbf{z}}^a$ and $\hat{\mathbf{z}}^b$ are the local $\langle 111 \rangle$ directions at the a and b sublattice sites defined in Table 1.3. $\hat{\mathbf{R}}_{ij}^{ab}$ are unit vectors in the directions $\mathbf{R}_{ij}^{ab}$, the vectors joining the a^{th} sublattice site of i^{th} FCC lattice site with the b^{th} sublattice site of the j^{th} FCC lattice site. The vector $\mathbf{\Omega}_{\rm DM}^{a,b}$ is the DM vector for the pyrochlore lattice [51], which is specified for the two pyrochlore lattice sites i, a and j, b by the five Moriya rules [68], which are:

1. When a centre of inversion is present at the midpoint (C) of a straight line joining two lattice sites i, a and j, b (AB), then $\mathbf{\Omega}_{\rm DM}^{a,b} = 0$,
2. When a mirror plane perpendicular to AB passes through the midpoint of AB, $\mathbf{\Omega}_{\rm DM}^{a,b}$ will be parallel to the mirror plane,
3. When there is a mirror plane that includes the lattice sites i, a and j, b, $\mathbf{\Omega}_{\rm DM}^{a,b}$ will be perpendicular to the mirror plane,
4. When a two-fold rotation axis perpendicular to AB passes through C, $\mathbf{\Omega}_{\rm DM}^{a,b}$ will be perpendicular to the two-fold rotation axis,
5. When there is an n-fold rotation axis along AB, $\mathbf{\Omega}_{\rm DM}^{a,b}$ will be parallel to AB.

The application of all of these rules yields the $\mathbf{\Omega}_{\rm DM}^{a,b}$ vectors shown in Fig. C.1 and defined in Table C.3. Note that we have chosen the indirect form of the DM vectors, which differs from the direct form only in the overall sign of the interaction, and that they are not normalized. This has been done for ease of use, as this form of the DM vectors gives $H_{\rm DM} \equiv \mathcal{J}_4 \mathcal{X}_4$.

Table C.3: The indirect Dzyaloshinskii-Moriya vectors for the pyrochlore lattice.

$\mathbf{\Omega}_{\mathrm{DM}}^{1,2}$	$(1,-1,0)$
$\mathbf{\Omega}_{\mathrm{DM}}^{1,3}$	$(-1,0,1)$
$\mathbf{\Omega}_{\mathrm{DM}}^{1,4}$	$(0,1,-1)$
$\mathbf{\Omega}_{\mathrm{DM}}^{2,3}$	$(0,-1,-1)$
$\mathbf{\Omega}_{\mathrm{DM}}^{2,4}$	$(1,0,-1)$
$\mathbf{\Omega}_{\mathrm{DM}}^{3,4}$	$(-1,-1,0)$

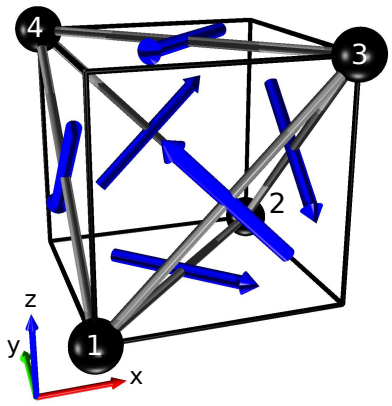

Figure C.1: The indirect Dzyaloshinskii-Moriya vectors for the pyrochlore lattice [21].

If we recast Eqn. (C.37) in the form

$$H_{\rm ex} = -\mathcal{J}_{\rm Ising}\mathcal{X}_{\rm Ising} - \mathcal{J}_{\rm iso}\mathcal{X}_{\rm iso} - \mathcal{J}_{\rm pd}\mathcal{X}_{\rm pd} - \mathcal{J}_{\rm DM}\mathcal{X}_{\rm pd}, \tag{C.42}$$

where $\mathcal{X}_{\rm Ising} = \frac{H_{\rm Ising}}{-\mathcal{J}_{\rm Ising}}$, $\mathcal{X}_{\rm iso} = \frac{H_{\rm iso}}{-\mathcal{J}_{\rm iso}}$, $\mathcal{X}_{\rm pd} = \frac{H_{\rm pd}}{-\mathcal{J}_{\rm pd}}$, and $\mathcal{X}_{\rm DM} = \frac{H_{\rm DM}}{-\mathcal{J}_{\rm DM}}$, then we can cast it in vector form as $H_{\rm ex} = -\overline{\mathcal{J}}^{T}{}_{e}\ \overline{\mathcal{X}}_{e}$. In this notation

$$\overline{\mathcal{J}_e} = \begin{pmatrix} \mathcal{J}_{\rm Ising} \\ \mathcal{J}_{\rm iso} \\ \mathcal{J}_{\rm pd} \\ \mathcal{J}_{\rm DM} \end{pmatrix}, \tag{C.43}$$

and

$$\overline{\mathcal{X}_e} = \begin{pmatrix} \mathcal{X}_{\rm Ising} \\ \mathcal{X}_{\rm iso} \\ \mathcal{X}_{\rm pd} \\ \mathcal{X}_{\rm DM} \end{pmatrix}. \tag{C.44}$$

The relationship between $\overline{\mathcal{X}}_e$ and $\overline{\mathcal{X}}$ is given by the matrix

$$\overline{\overline{U}} = \begin{pmatrix} -\frac{1}{3} & \frac{1}{3} & -\frac{1}{3} & \frac{1}{3} \\ 1 & 1 & 0 & 0 \\ \frac{-1}{2} & 1 & \frac{-3}{2} & 0 \\ 0 & 0 & 0 & 1 \end{pmatrix}, \tag{C.45}$$

and the equation

$$\overline{\mathcal{X}}_e = \overline{\overline{U}}\ \overline{\mathcal{X}}. \tag{C.46}$$

This means the the coupling energies $\{\mathcal{J}_e\}$ and $\{\mathcal{J}_n\}$ are related by the matrix equation

$$\overline{\mathcal{J}}^{T} = \overline{\mathcal{J}}_{e}^{T}\ \overline{\overline{U}}. \tag{C.47}$$

This relationship will be very important when presenting the results of this work. All of the computations of the magnetic interactions in $Yb_2Ti_2O_7$ were performed using the $\mathcal{X}_n$ representation of the symmetry allowed nearest neighbour interactions because they allow for the use of Eq. 2.4. The final Hamiltonian on the other hand is presented in the $\mathcal{X}_e$ representation because it allows for easier interpretation.

Appendix D

Actions of the Symmetry Operations of the Point Group O_h on the elements of the representation Γ of the Nearest Neighbour Exchange Interactions on the Pyrochlore Lattice

This appendix tabulates how the various symmetry operations of the the O_h point group act of the elements of the representation Γ defined in Appendix C. The actions of the symmetry operations in the first five columns of Table C.1 are given in Table D.1, while the the actions of the rest of the symmetry operations in O_h are given in Table D.2. These actions are described by the transformation of each of the four sub-lattice sites of the pyrochlore lattice in to one of the other sub-lattice sites, and the transformation of the global cartesian components under the symmetry operation. The actions of all of the symmetry operations are key to determining the character of a given symmetry operation in the representation Γ, and for finding the symmetry allowed exchange interactions on the pyrochlore lattice via the symmetry coordinates of the representation.

Table D.1: Actions of the symmetry operations of the point group O_h on the elements of the reducible representation Γ.

Symmetry Operation	Actions of the Members of This Class of Symmetry Operation (Column 1 gives the sub-lattice mappings, Column 2 gives the co-ordinate mappings)											
E	$1 \to 1$	$\hat{x} \to \hat{x}$										
	$2 \to 2$	$\hat{y} \to \hat{y}$										
	$3 \to 3$	$\hat{z} \to \hat{z}$										
	$4 \to 4$											
C_3	$1 \to 1$	$\hat{x} \to \hat{z}$	$1 \to 1$	$\hat{x} \to \hat{y}$	$1 \to 3$	$\hat{x} \to \hat{y}$	$1 \to 4$	$\hat{z} \to -\hat{y}$	$1 \to 2$	$\hat{x} \to \hat{z}$	$1 \to 4$	$\hat{x} \to -\hat{y}$
	$2 \to 3$	$\hat{z} \to \hat{y}$	$2 \to 4$	$\hat{y} \to \hat{z}$	$2 \to 2$	$\hat{y} \to -\hat{z}$	$4 \to 3$	$\hat{y} \to \hat{x}$	$2 \to 4$	$\hat{y} \to -\hat{x}$	$2 \to 1$	$\hat{y} \to -\hat{z}$
	$3 \to 4$	$\hat{y} \to \hat{x}$	$4 \to 3$	$\hat{z} \to \hat{x}$	$3 \to 4$	$\hat{z} \to -\hat{x}$	$3 \to 1$	$\hat{x} \to -\hat{z}$	$3 \to 3$	$\hat{z} \to -\hat{y}$	$3 \to 3$	$\hat{z} \to \hat{x}$
	$4 \to 2$		$3 \to 2$		$4 \to 1$		$2 \to 2$		$4 \to 1$		$4 \to 2$	
	$1 \to 2$	$\hat{x} \to -\hat{y}$	$1 \to 3$	$\hat{x} \to -\hat{z}$								
	$2 \to 3$	$\hat{y} \to \hat{z}$	$3 \to 2$	$\hat{y} \to -\hat{x}$								
	$3 \to 1$	$\hat{z} \to -\hat{x}$	$2 \to 1$	$\hat{z} \to \hat{y}$								
	$4 \to 4$		$4 \to 4$									
C_2'	$1 \to 1$	$\hat{x} \to -\hat{y}$	$1 \to 1$	$\hat{x} \to -\hat{x}$	$1 \to 1$	$\hat{x} \to -\hat{z}$	$1 \to 2$	$\hat{x} \to \hat{y}$	$1 \to 3$	$\hat{x} \to \hat{z}$	$1 \to 4$	$\hat{x} \to -\hat{x}$
	$2 \to 2$	$\hat{y} \to -\hat{x}$	$2 \to 3$	$\hat{y} \to -\hat{z}$	$2 \to 4$	$\hat{y} \to -\hat{y}$	$2 \to 1$	$\hat{y} \to \hat{x}$	$2 \to 2$	$\hat{y} \to -\hat{y}$	$2 \to 2$	$\hat{y} \to \hat{z}$
	$3 \to 4$	$\hat{z} \to -\hat{z}$	$3 \to 2$	$\hat{z} \to -\hat{y}$	$4 \to 2$	$\hat{z} \to -\hat{x}$	$3 \to 3$	$\hat{z} \to -\hat{z}$	$3 \to 1$	$\hat{z} \to \hat{x}$	$3 \to 3$	$\hat{z} \to \hat{y}$
	$4 \to 3$		$4 \to 4$		$3 \to 3$		$4 \to 4$		$4 \to 4$		$4 \to 1$	
C_4	$1 \to 3$	$\hat{x} \to -\hat{y}$	$1 \to 4$	$\hat{x} \to \hat{y}$	$1 \to 4$	$\hat{x} \to \hat{z}$	$1 \to 2$	$\hat{x} \to -\hat{z}$	$1 \to 3$	$\hat{x} \to \hat{x}$	$1 \to 2$	$\hat{x} \to \hat{x}$
	$3 \to 2$	$\hat{y} \to \hat{x}$	$4 \to 2$	$\hat{y} \to -\hat{x}$	$4 \to 3$	$\hat{y} \to \hat{y}$	$2 \to 3$	$\hat{y} \to \hat{y}$	$3 \to 4$	$\hat{y} \to \hat{z}$	$2 \to 4$	$\hat{y} \to -\hat{z}$
	$2 \to 4$	$\hat{z} \to \hat{z}$	$2 \to 3$	$\hat{z} \to \hat{z}$	$3 \to 2$	$\hat{z} \to -\hat{x}$	$3 \to 4$	$\hat{z} \to \hat{x}$	$4 \to 2$	$\hat{z} \to -\hat{y}$	$4 \to 3$	$\hat{z} \to \hat{y}$
	$4 \to 1$		$3 \to 1$		$2 \to 1$		$4 \to 1$		$2 \to 1$		$3 \to 1$	
C_2	$1 \to 2$	$\hat{x} \to -\hat{x}$	$1 \to 3$	$\hat{x} \to -\hat{x}$	$2 \to 3$	$\hat{x} \to \hat{x}$						
	$2 \to 1$	$\hat{y} \to -\hat{y}$	$3 \to 1$	$\hat{y} \to \hat{y}$	$3 \to 2$	$\hat{y} \to -\hat{y}$						
	$3 \to 4$	$\hat{z} \to \hat{z}$	$2 \to 4$	$\hat{z} \to -\hat{z}$	$1 \to 4$	$\hat{z} \to -\hat{z}$						
	$4 \to 3$		$4 \to 2$		$4 \to 1$							

Table D.2: Actions of the symmetry operations of the point group O_h on the elements of the reducible representation Γ continued.

Symmetry Operation	Actions of the Members of This Class of Symmetry Operation (Column 1 gives the sub-lattice mappings, Column 2 gives the co-ordinate mappings)											
i	$1 \to 1$	$\hat{x} \to -\hat{x}$										
	$2 \to 2$	$\hat{y} \to -\hat{y}$										
	$3 \to 3$	$\hat{z} \to -\hat{z}$										
	$4 \to 4$											
S_4	$1 \to 3$	$\hat{x} \to \hat{y}$	$1 \to 4$	$\hat{x} \to -\hat{y}$	$1 \to 4$	$\hat{x} \to -\hat{z}$	$1 \to 2$	$\hat{x} \to \hat{z}$	$1 \to 3$	$\hat{x} \to -\hat{x}$	$1 \to 2$	$\hat{x} \to -\hat{x}$
	$3 \to 2$	$\hat{y} \to -\hat{x}$	$4 \to 2$	$\hat{y} \to \hat{x}$	$4 \to 3$	$\hat{y} \to -\hat{y}$	$2 \to 3$	$\hat{y} \to -\hat{y}$	$3 \to 4$	$\hat{y} \to -\hat{z}$	$2 \to 4$	$\hat{y} \to \hat{z}$
	$2 \to 4$	$\hat{z} \to -\hat{z}$	$2 \to 3$	$\hat{z} \to -\hat{z}$	$3 \to 2$	$\hat{z} \to \hat{x}$	$3 \to 4$	$\hat{z} \to -\hat{x}$	$4 \to 2$	$\hat{z} \to \hat{y}$	$4 \to 3$	$\hat{z} \to -\hat{y}$
	$4 \to 1$		$3 \to 1$		$2 \to 1$		$4 \to 1$		$2 \to 1$		$3 \to 1$	
S_6	$1 \to 1$	$\hat{x} \to -\hat{z}$	$1 \to 1$	$\hat{x} \to -\hat{y}$	$1 \to 3$	$\hat{x} \to -\hat{y}$	$1 \to 4$	$\hat{z} \to \hat{y}$	$1 \to 2$	$\hat{x} \to -\hat{z}$	$1 \to 4$	$\hat{x} \to \hat{y}$
	$2 \to 3$	$\hat{z} \to -\hat{y}$	$2 \to 4$	$\hat{y} \to -\hat{z}$	$2 \to 2$	$\hat{y} \to \hat{z}$	$4 \to 3$	$\hat{y} \to -\hat{x}$	$2 \to 4$	$\hat{y} \to \hat{x}$	$2 \to 1$	$\hat{y} \to \hat{z}$
	$3 \to 4$	$\hat{y} \to -\hat{x}$	$4 \to 3$	$\hat{z} \to -\hat{x}$	$3 \to 4$	$\hat{z} \to \hat{x}$	$3 \to 1$	$\hat{x} \to \hat{z}$	$3 \to 3$	$\hat{z} \to \hat{y}$	$3 \to 3$	$\hat{x} \to -\hat{x}$
	$4 \to 2$		$3 \to 2$		$4 \to 1$		$2 \to 2$		$4 \to 1$		$4 \to 1$	
	$1 \to 2$	$\hat{x} \to \hat{y}$	$1 \to 3$	$\hat{x} \to \hat{z}$								
	$2 \to 3$	$\hat{y} \to -\hat{z}$	$3 \to 2$	$\hat{y} \to \hat{x}$								
	$3 \to 1$	$\hat{z} \to \hat{x}$	$2 \to 1$	$\hat{z} \to -\hat{y}$								
	$4 \to 1$		$4 \to 4$									
σ_h	$1 \to 2$	$\hat{x} \to \hat{x}$	$1 \to 3$	$\hat{x} \to \hat{x}$	$2 \to 3$	$\hat{x} \to -\hat{x}$						
	$2 \to 1$	$\hat{y} \to \hat{y}$	$3 \to 1$	$\hat{y} \to -\hat{y}$	$3 \to 2$	$\hat{y} \to \hat{y}$						
	$3 \to 4$	$\hat{z} \to -\hat{z}$	$2 \to 4$	$\hat{z} \to \hat{z}$	$1 \to 4$	$\hat{z} \to \hat{z}$						
	$4 \to 3$		$4 \to 2$		$4 \to 1$							
σ_d	$1 \to 1$	$\hat{x} \to \hat{y}$	$1 \to 1$	$\hat{x} \to \hat{x}$	$1 \to 1$	$\hat{x} \to \hat{z}$	$1 \to 2$	$\hat{x} \to -\hat{y}$	$1 \to 3$	$\hat{x} \to -\hat{z}$	$1 \to 4$	$\hat{x} \to \hat{x}$
	$2 \to 2$	$\hat{y} \to \hat{x}$	$2 \to 3$	$\hat{y} \to \hat{z}$	$2 \to 4$	$\hat{y} \to \hat{y}$	$2 \to 1$	$\hat{y} \to -\hat{x}$	$2 \to 2$	$\hat{y} \to \hat{y}$	$2 \to 2$	$\hat{y} \to -\hat{z}$
	$3 \to 4$	$\hat{z} \to \hat{z}$	$3 \to 2$	$\hat{z} \to \hat{y}$	$3 \to 3$	$\hat{z} \to \hat{x}$	$3 \to 3$	$\hat{z} \to \hat{z}$	$3 \to 1$	$\hat{z} \to -\hat{x}$	$3 \to 3$	$\hat{z} \to -\hat{y}$
	$4 \to 3$		$4 \to 4$		$4 \to 2$		$4 \to 4$		$4 \to 4$		$4 \to 1$	

Appendix E

Long Range Dipolar Interactions

In this Appendix, we discuss the long-range magnetic dipolar interaction term of the magnetic Hamiltonian for $Yb_2Ti_2O_7$. Magnetic dipolar interactions are the interactions that arise between magnetic moments due to the interaction of one magnetic dipole moment with the magnetic field generated by another magnetic dipole moment. When this interaction is summed over all of the magnetic moments in a system it takes the form of Eqn. (2.12). Computing the long-range dipolar contributions to the magnetic interactions in this work is done using the Ewald summation technique. This technique is useful, as the dipolar interaction is infinite ranged, so the sum over $i > j; a, b$ involves all of the spins in the system. This sum converges very slowly, and choosing different cut-off distances for the infinite sum corresponds to different sample configurations and macroscopic magnetic fields [54, 60]. To avoid these convergence issues we desire a way to approximate the infinite lattice sum and the Ewald summation technique provides just such an approximation. This summary is based heavily on Refs. [54, 60] and is provided here in the interests of creating a self-contained thesis. We also include some comments that correct problems discovered with the presentation and results of Ref. [60]. The goal of the Ewald summation is to split the real space sum, which is highly dependent on boundary conditions, into two absolutely convergent sums; one in real space and one in reciprocal space [54]. One important aspect of the form of the Ewald summation discussed here is that it yields the Fourier transform of the long-range dipolar interaction matrix, $\mathcal{D}^{a,b}_{u,v}(\mathbf{q})$, not the real space interaction matrix. Some of the methods discussed in this study do require the use of real space Ewald sums, such as the mean field calculations of χ_a in Chapter 6 and the Monte Carlo methods of Chapter 7, and these are discussed in Refs. [46, 47].

The first step in the Ewald summation method is to define the long-range magnetic dipolar interactions as a matrix of the same form as the matrix $\overline{\overline{\mathcal{J}}}(i, j)$ used to describe

the nearest-neighbour bilinear exchange interactions in Appendix C.1. Using this form of the interactions we can write

$$H_{\text{dip}} = \sum_{\langle i,a;j,b\rangle} \left(\mathbf{J}_i^a\right)^T \ \overline{\overline{\mathcal{D}}}^{a,b}\left(i,j\right) \ \mathbf{J}_j^b, \tag{E.1}$$

where $\mathbf{J}_i^a$ and $\mathbf{J}_j^b$ are the same angular momentum vectors as in Eqn. (2.4), and $\overline{\overline{\mathcal{D}}}^{a,b}\left(i,j\right)$ is a 3×3 sub-matrix of the 12×12 matrix $\overline{\overline{\mathcal{D}}}\left(i,j\right)$, with same relationship between the two as between $\overline{\overline{\mathcal{J}}}^{a,b}\left(i,j\right)$ and Eqn. (2.5).

Now, we may proceed with presenting the Ewald summation method explained in Refs. [54, 60] in the notation of this work. To do this we start by defining the elements of the matrix $\overline{\overline{\mathcal{D}}}\left(i,j\right)$:

$$\mathcal{D}_{u,v}^{a,b}\left(i,j\right) = \frac{\hat{n}^u\cdot\hat{n}^v}{|\mathbf{R}_{ij}^{ab}|^3} - 3\frac{\left(\hat{n}^u\cdot\mathbf{R}_{ij}^{ab}\right)\left(\hat{n}^v\cdot\mathbf{R}_{ij}^{ab}\right)}{|\mathbf{R}_{ij}^{ab}|^5}, \tag{E.2}$$

where $\mathbf{R}_{ij}^{ab}$ is the vector joining the i,a and j,b pyrochlore lattice sites, as defined in Chapter 1.2, and $\hat{n}^u$ and $\hat{n}^v$ are the global cartesian unit vectors $\hat{x}$, $\hat{y}$, and $\hat{z}$. This form of $\overline{\overline{\mathcal{D}}}\left(i,j\right)$ can be recast as

$$\mathcal{D}_{u,v}^{a,b}\left(i,j\right) = -\left(\hat{n}^u\cdot\nabla_x\right)\left(\hat{n}^v\cdot\nabla_x\right)\left\{\frac{1}{\mathbf{R}_{ij}^{ab}-\mathbf{x}}\right\}\Bigg|_{\mathbf{x}=0}. \tag{E.3}$$

The Fourier transform of $\overline{\overline{\mathcal{D}}}\left(i,j\right)$, $\overline{\overline{\mathcal{D}}}\left(\mathbf{q}\right)$, can be defined in terms of its components by:

$$\mathcal{D}_{u,v}^{a,b}\left(\mathbf{q}\right) = -\left(\hat{n}^u\cdot\nabla_x\right)\left(\hat{n}^v\cdot\nabla_x\right)\left\{\sum_i{}' \frac{e^{-i\mathbf{q}\cdot\mathbf{R}_{ij}^{ab}}}{\mathbf{R}_{ij}^{ab}-\mathbf{x}}\right\}\Bigg|_{\mathbf{x}=0}, \tag{E.4}$$

where $\mathbf{q}$ is a wave-vector inside the first Brillouin zone, and the prime on the sum indicates a sum over $\mathbf{R}_{ij}^{ab}$ that does not include the term where $\mathbf{R}_{ij}^{ab}=0$. The next step is to rewrite Eqn. (E.4) with a sum over all $\mathbf{R}_{ij}^{ab}$:

$$\mathcal{D}_{u,v}^{a,b}\left(\mathbf{q}\right) = -(\hat{n}^u\cdot\nabla_x)\left(\hat{n}^v\cdot\nabla_x\right)\left\{\sum_i\frac{e^{-i\mathbf{q}\cdot\mathbf{R}_{ij}^{ab}}}{\mathbf{R}_{ij}^{ab}-\mathbf{x}}\right\}\Bigg|_{\mathbf{x}=0} + \delta_{a,b}\left(\hat{n}^u\cdot\nabla_x\right)\left(\hat{n}^v\cdot\nabla_x\right)\left\{\frac{1}{|\mathbf{x}|}\right\}\Bigg|_{\mathbf{x}=0}. \tag{E.5}$$

Next, we recall the definition of a Gaussian integral [54, 60, 69]

$$\frac{1}{|\mathbf{R}|} = \frac{2}{\sqrt{\pi}}\int_0^\infty e^{-t^2R^2}dt. \tag{E.6}$$

This result can be used to rewrite Eqn. (E.5) as

$$\mathcal{D}^{a,b}_{u,v}(\mathbf{q}) = -(\hat{n}^u\cdot\nabla_x)(\hat{n}^v\cdot\nabla_x)\int_0^\infty dt\frac{2}{\sqrt{\pi}}e^{-i\mathbf{q}\cdot\mathbf{x}}\left\{\sum_i e^{-t^2|\mathbf{R}^{ab}_{ij}-\mathbf{x}|^2-i\mathbf{q}\cdot\left(\mathbf{R}^{ab}_{ij}-\mathbf{x}\right)}\right\}\Bigg|_{\mathbf{x}=0} + \delta_{a,b}(\hat{n}^u\cdot\nabla_x)(\hat{n}^v\cdot\nabla_x)\left\{\frac{1}{|\mathbf{x}|}\right\}\Bigg|_{\mathbf{x}=0}. \quad \text{(E.7)}$$

We next split the integral in Eqn. (E.7) into two regions $[0,\alpha]$, and $[\alpha,\infty)$ [54]. This division of the integral leads to the real space and reciprocal space sums mentioned earlier. The integral over the range $[0,\alpha]$ contributes to the real space sum, and the integral over the range $[\alpha,\infty)$ contributes to the reciprocal space sum. It is important to note that the integral over the range $[\alpha,\infty)$ has a divergence at $\mathbf{R}^{ab}_{ij}=0$, so a careful treatment of this term is required [54]. The two ranges of integration are controlled by α, a convergence parameter with units of inverse distance.

Our next step is to write Eqn. (E.7) explicitly as three separate terms, which we can then split up and consider individually:

$$\mathcal{D}^{a,b}_{u,v}(\mathbf{q}) = A^{a,b}_{u,v}(\mathbf{q}) + B^{a,b}_{u,v}(\mathbf{q}) + C^{a,b}_{u,v}(\mathbf{q}), \quad \text{(E.8)}$$

where

$$A^{a,b}_{u,v}(\mathbf{q}) = -(\hat{n}^u\cdot\nabla_x)(\hat{n}^v\cdot\nabla_x)\int_0^\alpha dt\frac{2}{\sqrt{\pi}}e^{-i\mathbf{q}\cdot\mathbf{x}}\left\{\sum_i e^{-t^2|\mathbf{R}^{ab}_{ij}-\mathbf{x}|^2-i\mathbf{q}\cdot\left(\mathbf{R}^{ab}_{ij}-\mathbf{x}\right)}\right\}\Bigg|_{\mathbf{x}=0}, \quad \text{(E.9)}$$

$$B^{a,b}_{u,v}(\mathbf{q}) = -(\hat{n}^u\cdot\nabla_x)(\hat{n}^v\cdot\nabla_x)\int_\alpha^\infty dt\frac{2}{\sqrt{\pi}}e^{-i\mathbf{q}\cdot\mathbf{x}}\left\{\sum_i{}' e^{-t^2|\mathbf{R}^{ab}_{ij}-\mathbf{x}|^2-i\mathbf{q}\cdot\left(\mathbf{R}^{ab}_{ij}-\mathbf{x}\right)}\right\}\Bigg|_{\mathbf{x}=0}, \quad \text{(E.10)}$$

$$C^{a,b}_{u,v}(\mathbf{q}) = \delta_{a,b}(\hat{n}^u\cdot\nabla_x)(\hat{n}^v\cdot\nabla_x)\left\{\frac{1}{|\mathbf{x}|}-\int_\alpha^\infty dt\frac{2}{\sqrt{\pi}}e^{-t^2|\mathbf{x}|^2}\right\}\Bigg|_{\mathbf{x}=0}. \quad \text{(E.11)}$$

Now we can deal with the three terms, $A^{a,b}_{u,v}(\mathbf{q})$, $B^{a,b}_{u,v}(\mathbf{q})$, and $C^{a,b}_{u,v}(\mathbf{q})$, starting with $A^{a,b}_{u,v}(\mathbf{q})$. To deal with this term, we note that the term in $\{\}$ brackets is a periodic function of $\mathbf{x}$. Using this feature of the equation, we can rewrite it as a Fourier series following Ref. [54],

$$f(x) = \sum_i e^{-t^2|\mathbf{R}^{ab}_{ij}-\mathbf{x}|^2-i\mathbf{q}\cdot\left(\mathbf{R}^{ab}_{ij}-\mathbf{x}\right)} = \sum_{\mathbf{k}} g_{\mathbf{k}}e^{i\mathbf{k}\cdot\mathbf{x}}. \quad \text{(E.12)}$$

Solving for $g_{\mathbf{k}}$ yields

$$g_{\mathbf{k}=G} = \frac{4\pi}{v}\frac{e^{-i\mathbf{G}\cdot(\mathbf{r}_a-\mathbf{r}_b)}}{|\mathbf{q}-\mathbf{G}|^3}F(z), \quad \text{(E.13)}$$

where $\mathbf{G}$ is one of the reciprocal lattice vectors of the pyrochlore lattice, defined in Chapter 1.2, v is the volume of the unit cell, and (Eqn. C13, Ref. [54])

$$F(z) = \int_0^\infty y \sin(y)\, e^{-z^2 y^2} dy = \frac{\sqrt{\pi}}{4z^3} e^{-1/4z^2}, \tag{E.14}$$

where $z = t/|\mathbf{q} - \mathbf{G}|$. Combining Eqn. (E.12) with Eqn. (E.13) yields the result

$$f(x) = \frac{4\pi}{v} \sum_{\mathbf{G}} \frac{e^{-i\mathbf{G}\cdot(\mathbf{r}_b - \mathbf{r}_a - \mathbf{x})}}{|\mathbf{q} - \mathbf{G}|^3} F(z). \tag{E.15}$$

Substituting Eqn. (E.15) into Eqn. (E.9), taking the differentials, and imposing the limits with respect to $\mathbf{x}$, we obtain the result

$$A_{u,v}^{a,b}(\mathbf{q}) = \frac{4\pi}{v} \sum_{\mathbf{G}} \frac{[\hat{n}^u \cdot (\mathbf{q} - \mathbf{G})]\,[\hat{n}^v \cdot (\mathbf{q} - \mathbf{G})]}{|\mathbf{q} - \mathbf{G}|^2} e^{-i\mathbf{G}\cdot\mathbf{r}^{ab}} \frac{2}{\sqrt{\pi}} \int_0^\alpha dt\ F(t/|\mathbf{q} - \mathbf{G}|). \tag{E.16}$$

Performing the integral over the range $[0, \alpha]$ using Eqn. (E.14), we obtain

$$A_{u,v}^{a,b}(\mathbf{q}) = \frac{4\pi}{v} \sum_{\mathbf{G}} \frac{[\hat{n}^u \cdot (\mathbf{q} - \mathbf{G})]\,[\hat{n}^v \cdot (\mathbf{q} - \mathbf{G})]}{|\mathbf{q} - \mathbf{G}|^2} e^{-|\mathbf{q}-\mathbf{G}|^2/4\alpha^2 - i\mathbf{G}\cdot\mathbf{r}^{ab}}, \tag{E.17}$$

where the sum is over all of the reciprocal lattice vectors $\mathbf{G}$.

The $\mathbf{G} = 0$ term in this sum becomes non-analytic when $\mathbf{q} = 0$. The $\mathbf{G} = 0$ term is

$$\frac{4\pi}{v} \frac{[\hat{n}^u \cdot (\mathbf{q})]\,[\hat{n}^v \cdot (\mathbf{q})]}{|\mathbf{q}|^2} e^{-|\mathbf{q}|^2/4\alpha^2}. \tag{E.18}$$

In previous works this term in its entirety has been treated as the macroscopic magnetic field due to the sample geometry, and has been set equal to zero because it is poorly behaved [54, 60]. Ref. [70] explains that this is not actually the correct way to treat this term. Instead, we add and subtract one from the exponential, to yield

$$\frac{4\pi}{v} \frac{[\hat{n}^u \cdot (\mathbf{q})]\,[\hat{n}^v \cdot (\mathbf{q})]}{|\mathbf{q}|^2} + \frac{4\pi}{v} \frac{[\hat{n}^u \cdot (\mathbf{q})]\,[\hat{n}^v \cdot (\mathbf{q})]}{|\mathbf{q}|^2} \left(e^{-|\mathbf{q}|^2/4\alpha^2} - 1\right) \tag{E.19}$$

According to Ref. [70], only the first term of this expansion is the macroscopic field, which can be set equal to zero. The second term is well behaved at $\mathbf{q} = 0$ because $\left(e^{-|\mathbf{q}|^2/4\alpha^2} - 1\right)$ behaves as $|\mathbf{q}|^2$ for small $\mathbf{q}$ and cancels out the $1/|\mathbf{q}|^2$ in $\frac{[\hat{n}^u \cdot (\mathbf{q})][\hat{n}^v \cdot (\mathbf{q})]}{|\mathbf{q}|^2}$. This well behaved

component of the $\mathbf{q}=0$, $\mathbf{G}=0$ term should be kept in $A^{a,b}_{u,v}(\mathbf{q})$ in order to avoid problems at $\mathbf{q}=0$ [71].

We are now finished with the term $A^{a,b}_{u,v}(\mathbf{q})$, and we may move on to the other terms in $\mathcal{D}^{a,b}_{u,v}(\mathbf{q})$. The next term we consider is $B^{a,b}_{u,v}(\mathbf{q})$. The first step in treating this term is to rearrange Eqn. (E.10) into a known integral form. By reversing the sum and integral we obtain

$$B^{a,b}_{u,v}(\mathbf{q}) = -\left(\hat{n}^u\cdot\nabla_x\right)\left(\hat{n}^v\cdot\nabla_x\right)\sum_i{}' e^{-i\mathbf{q}\cdot\mathbf{R}^{ab}_{ij}}\frac{2}{\sqrt{\pi}}\int_\alpha^\infty dt\ \left\{e^{-t^2|\mathbf{R}^{ab}_{ij}-\mathbf{x}|^2}\right\}\Big|_{\mathbf{x}=0}. \tag{E.20}$$

The integral in this equation can be written as a complementary error function

$$\mathrm{erfc}(z) = \frac{2}{\sqrt{\pi}}\int_z^\infty e^{-x^2}dx. \tag{E.21}$$

The final form of $B^{a,b}_{u,v}(\mathbf{q})$ is obtained by applying the differential operators of Eqn. (E.20), taking the limit $\mathbf{x}\to 0$, and performing the integral over t, yielding the final form of $B^{a,b}_{u,v}(\mathbf{q})$,

$$B^{a,b}_{u,v}(\mathbf{q}) = \sum_i{}'\left[S1^{a,b}_{u,v}\left(\mathbf{R}^{ab}_{ij}\right) - S2^{a,b}_{u,v}\left(\mathbf{R}^{ab}_{ij}\right)\right]e^{-i\mathbf{q}\cdot\mathbf{R}^{ab}_{ij}}. \tag{E.22}$$

The two terms in this equation are given by:

$$S1^{a,b}_{u,v}\left(\mathbf{R}^{ab}_{ij}\right) = \left(\hat{n}^u\cdot\hat{n}^v\right)\left\{\frac{2\alpha}{\sqrt{\pi}}\frac{e^{-\alpha^2|\mathbf{R}^{ab}_{ij}|^2}}{|\mathbf{R}^{ab}_{ij}|^2} + \frac{\mathrm{erfc}\left(\alpha|\mathbf{R}^{ab}_{ij}|\right)}{|\mathbf{R}^{ab}_{ij}|^3}\right\}, \tag{E.23}$$

and

$$S2^{a,b}_{u,v}\left(\mathbf{R}^{ab}_{ij}\right) = \left(\hat{n}^u\cdot\mathbf{R}^{ab}_{ij}\right)\left(\hat{n}^v\cdot\mathbf{R}^{ab}_{ij}\right)\left\{\left[\frac{4\alpha^3}{\sqrt{\pi}|\mathbf{R}^{ab}_{ij}|^2} + \frac{6\alpha}{\sqrt{\pi}|\mathbf{R}^{ab}_{ij}|^4}\right]e^{-\alpha^2|\mathbf{R}^{ab}_{ij}|^2} + \frac{3\mathrm{erfc}\left(\alpha|\mathbf{R}^{ab}_{ij}|\right)}{|\mathbf{R}^{ab}_{ij}|^5}\right\}. \tag{E.24}$$

Equations E.22-E.24 form the real space sum discussed earlier. It is useful to note that the $\sum_i{}'$ means the the term $\mathbf{R}^{ab}_{ij}=0$ is not included, making the real space sum analytic [54].

Now we may deal with the final term of Eqn. (E.8), $C^{a,b}_{u,v}(\mathbf{q})$, which contains the $\mathbf{R}^{ab}_{ij}=0$ singularity. Following Ref. [54] and applying the differential operators in Eqn. (E.11), we obtain the result

$$C^{a,b}_{u,v}(\mathbf{q}) = \lim_{x\to 0}\delta_{a,b}\left\{-\frac{\left(\hat{n}^u\cdot\hat{n}^v\right)}{|\mathbf{x}|^3} + \frac{3\left(\hat{n}^u\cdot\mathbf{x}\right)\left(\hat{n}^v\cdot\mathbf{x}\right)}{|\mathbf{x}|^5} + \left(S1^{a,b}_{u,v}(\mathbf{x}) - S2^{a,b}_{u,v}(\mathbf{x})\right)\right\}, \tag{E.25}$$

where $S1^{a,b}_{u,v}(\mathbf{x})$ and $S2^{a,b}_{u,v}(\mathbf{x})$ are the same functions as are defined in Eqns. (E.23),(E.24), with $\mathbf{x}$ replacing $\mathbf{R}^{ab}_{ij}$. The limit in Eqn. (E.25) is evaluated by taking series expansions of the exponentials to $O(x^2)$ and the complementary error function to $O(x^3)$. The final result is a constant:

$$C^{a,b}_{u,v}(\mathbf{q}) = -\frac{4\alpha^3}{3\sqrt{\pi}}\left(\hat{n}^u \cdot \hat{n}^v\right)\delta_{a,b}. \tag{E.26}$$

This result gives us all of the terms in Eqn. (E.8), and thus the final form of $\mathcal{D}^{a,b}_{u,v}(\mathbf{q})$ is:

$$\begin{aligned}\mathcal{D}^{a,b}_{u,v}(\mathbf{q}) = &-\frac{4\alpha^3}{3\sqrt{\pi}}\left(\hat{n}^u \cdot \hat{n}^v\right)\delta_{a,b} \\ &+ \frac{4\pi}{v}\sum_{\mathbf{G}}\frac{\left[\hat{n}^u \cdot (\mathbf{q}-\mathbf{G})\right]\left[\hat{n}^v \cdot (\mathbf{q}-\mathbf{G})\right]}{|\mathbf{q}-\mathbf{G}|^2}e^{-|\mathbf{q}-\mathbf{G}|^2/4\alpha^2 - i\mathbf{G}\cdot\mathbf{r}^{ab}} \\ &+ \sum_i{}' \left[S1^{a,b}_{u,v}\left(\mathbf{R}^{ab}_{ij}\right) - S2^{a,b}_{u,v}\left(\mathbf{R}^{ab}_{ij}\right)\right]e^{-i\mathbf{q}\cdot\mathbf{R}^{ab}_{ij}}.\end{aligned} \tag{E.27}$$

Appendix F

The Magnetic Form Factor of Yb^{3+}

The magnetic form factor for Yb^{3+} is taken from Ref. [72]. We take the form factor $F(\mathbf{Q})$ to have the form

$$F(s) = \langle j_0(s)\rangle + \left(\frac{2}{g_J} - 1\right)\langle j_2(s)\rangle, \tag{F.1}$$

where $g_J = 8/7$ is landé factor for Yb^{3+}, $s = \frac{|\mathbf{Q}|}{4\pi r_c}$, where $r_c = 10.026$ Å is the cubic unit cell dimension [6], and $\langle j_0(s)\rangle$ and $\langle j_2(s)\rangle$ are given by

$$\langle j_0(s)\rangle = A_0 \exp\left(-a_0 s^2\right) + B_0 \exp\left(-b_0 s^2\right) + C_0 \exp\left(-c_0 s^2\right) + D_0 \tag{F.2}$$

$$\langle j_2(s)\rangle = s^2\left(A_2 \exp\left(-a_2 s^2\right) + B_2 \exp\left(-b_2 s^2\right) + C_2 \exp\left(-c_2 s^2\right) + D_2\right). \tag{F.3}$$

The coefficients A_0, a_0, B_0, b_0, C_0, c_0, D_0, A_2, a_2, B_2, b_2, C_2, c_2, and D_2 are given in Table F.1 and Table F.2.

Table F.1: The $\langle j_0(s)\rangle$ magnetic form factor coefficients for Yb^{3+}, reproduced from Ref. [72], Table 4.4.5.3

Ion	A_0	a_0	B_0	b_0	C_0	c_0	D_0
Yb^{3+}	0.0416	16.095	0.2849	7.834	0.696	2.672	−0.0229

Table F.2: The $\langle j_2(s)\rangle$ magnetic form factor coefficients for Yb^{3+}, reproduced from Ref. [72], Table 4.4.5.7

Ion	A_2	a_2	B_2	b_2	C_2	c_2	D_2
Yb^{3+}	0.1570	18.555	0.8484	6.540	0.8880	2.037	0.0318

Appendix G

Fourier Transform of Nearest Neighbour Interactions on the Pyrochlore Lattice

This appendix provides the Fourier transform of the nearest neighbour exchange interaction matrix $\overline{\overline{\mathcal{J}}}$, $\overline{\overline{\mathcal{J}}}(\mathbf{q})$. To obtain this result we start from the expanded form of $\overline{\overline{\mathcal{J}}}$, given by Eqn. (2.5)

$$\overline{\overline{\mathcal{J}}} = \begin{pmatrix} \overline{\overline{0}} & \overline{\overline{\mathcal{J}}}^{1,2} & \overline{\overline{\mathcal{J}}}^{1,3} & \overline{\overline{\mathcal{J}}}^{1,4} \\ \overline{\overline{\mathcal{J}}}^{2,1} & \overline{\overline{0}} & \overline{\overline{\mathcal{J}}}^{2,3} & \overline{\overline{\mathcal{J}}}^{2,4} \\ \overline{\overline{\mathcal{J}}}^{3,1} & \overline{\overline{\mathcal{J}}}^{3,2} & \overline{\overline{0}} & \overline{\overline{\mathcal{J}}}^{3,4} \\ \overline{\overline{\mathcal{J}}}^{4,1} & \overline{\overline{\mathcal{J}}}^{4,2} & \overline{\overline{\mathcal{J}}}^{4,3} & \overline{\overline{0}} \end{pmatrix}. \tag{G.1}$$

We then note that each component matrix $\overline{\overline{\mathcal{J}}}^{a,b}$ will have a different Fourier transform form, given by

$$\overline{\overline{\mathcal{J}}}^{a,b}(\mathbf{q}) = 2\,\overline{\overline{\mathcal{J}}}^{a,b}(1-\delta_{ab})\cos\left(\mathbf{q}\cdot(\mathbf{r}_b-\mathbf{r}_a)\right), \tag{G.2}$$

where $\mathbf{r}_a$ are the sublattice vectors defined in Table 1.1. Applying this to all of the component matrices of $\overline{\overline{\mathcal{J}}}$ yields Eqn. (G.3).

$$\overline{\overline{\mathcal{J}}}(\mathbf{q}) = \begin{pmatrix} \overline{\overline{0}} & 2 \cdot \overline{\overline{\mathcal{J}}}^{1,2} \cdot \cos\left(\mathbf{q} \cdot (\mathbf{r}_1 - \mathbf{r}_2)\right) & 2 \cdot \overline{\overline{\mathcal{J}}}^{1,3} \cdot \cos\left(\mathbf{q} \cdot (\mathbf{r}_1 - \mathbf{r}_3)\right) & 2 \cdot \overline{\overline{\mathcal{J}}}^{1,4} \cdot \cos\left(\mathbf{q} \cdot (\mathbf{r}_1 - \mathbf{r}_4)\right) \\ 2 \cdot \overline{\overline{\mathcal{J}}}^{2,1} \cdot \cos\left(\mathbf{q} \cdot (\mathbf{r}_2 - \mathbf{r}_1)\right) & \overline{\overline{0}} & 2 \cdot \overline{\overline{\mathcal{J}}}^{2,3} \cdot \cos\left(\mathbf{q} \cdot (\mathbf{r}_2 - \mathbf{r}_3)\right) & 2 \cdot \overline{\overline{\mathcal{J}}}^{2,4} \cdot \cos\left(\mathbf{q} \cdot (\mathbf{r}_2 - \mathbf{r}_4)\right) \\ 2 \cdot \overline{\overline{\mathcal{J}}}^{3,1} \cdot \cos\left(\mathbf{q} \cdot (\mathbf{r}_3 - \mathbf{r}_1)\right) & 2 \cdot \overline{\overline{\mathcal{J}}}^{3,2} \cdot \cos\left(\mathbf{q} \cdot (\mathbf{r}_3 - \mathbf{r}_2)\right) & \overline{\overline{0}} & 2 \cdot \overline{\overline{\mathcal{J}}}^{3,4} \cdot \cos\left(\mathbf{q} \cdot (\mathbf{r}_3 - \mathbf{r}_4)\right) \\ 2 \cdot \overline{\overline{\mathcal{J}}}^{4,1} \cdot \cos\left(\mathbf{q} \cdot (\mathbf{r}_4 - \mathbf{r}_1)\right) & 2 \cdot \overline{\overline{\mathcal{J}}}^{4,2} \cdot \cos\left(\mathbf{q} \cdot (\mathbf{r}_4 - \mathbf{r}_2)\right) & 2 \cdot \overline{\overline{\mathcal{J}}}^{4,3} \cdot \cos\left(\mathbf{q} \cdot (\mathbf{r}_4 - \mathbf{r}_3)\right) & \overline{\overline{0}} \end{pmatrix}. \tag{G.3}$$

Appendix H

Effective Spin-1/2 Hamiltonians

As discussed in Chapter 2 our model for $Yb_2Ti_2O_7$ is closely related to an effective spin-1/2 model and in this Appendix we provide more detail on this relationship. We also perform a direct comparison to the work of Onoda on effective spin-1/2 model of $Yb_2Ti_2O_7$ [52], which shows that our findings of abnormally large Dzyaloshinskii-Moriya (DM) interactions in $Yb_2Ti_2O_7$ may in fact be consistent with other models of this material. This is a reproduction of the supplemental material of Ref. [31].

In Chapter 2, and Appendix A, we discussed the $\mathbf{g}$ tensor description of the ground state doublet of the CEF, which reflects the anisotropic nature of the ground state when written in terms of an effective spin-1/2. The exact relationship between $\mathbf{J}$ and $\vec{\sigma}$ is given by

$$\mathbf{J} = \frac{1}{2g_J}\mathbf{g}\ \vec{\sigma}, \tag{H.1}$$

where the $\mathbf{g}$ tensor defined in Appendix A. Using this relationship, we may convert the nearest-neighbour bilinear exchange Hamiltonian, $H_{\rm int} = H_{\rm Ising} + H_{\rm iso} + H_{\rm pd} + H_{\rm DM}$, defined in Chapter 4.2 into an effective spin-1/2 Hamiltonian $H'_{\rm int} = H'_{\rm Ising} + H'_{\rm iso} + H'_{\rm pd} + H'_{\rm DM}$ [31].

In this form of the Hamiltonian (Eqns. 5-7 in Ref. [31]):

$$H'_{\text{Ising}} = -\frac{\mathcal{J}_{\text{Ising}}}{4g_J^2} \sum_{<i,a;j,b>} \left(\mathbf{g}_i^a \vec{\sigma}_i^a \cdot \hat{\mathbf{z}}^a\right) \left(\mathbf{g}_j^b \vec{\sigma}_j^b \cdot \hat{\mathbf{z}}^b\right), \tag{H.2}$$

$$H'_{\text{iso}} = -\frac{\mathcal{J}_{\text{iso}}}{4g_J^2} \sum_{<i,a;j,b>} \mathbf{g}_i^a \vec{\sigma}_i^a \cdot \mathbf{g}_j^b \vec{\sigma}_j^b, \tag{H.3}$$

$$H'_{\text{pd}} = -\frac{\mathcal{J}_{\text{pd}}}{4g_J^2} \sum_{<i,a;j,b>} (\mathbf{g}_i^a \vec{\sigma}_i^a \cdot \mathbf{g}_j^b \vec{\sigma}_j^b - 3(\mathbf{g}_i^a \vec{\sigma}_i^a \cdot \hat{\mathbf{R}}_{ij}^{ab})(\mathbf{g}_j^b \vec{\sigma}_j^b \cdot \hat{\mathbf{R}}_{ij}^{ab})), \tag{H.4}$$

$$H'_{\text{DM}} = -\frac{\mathcal{J}_{\text{DM}}}{4g_J^2} \sum_{<i,a;j,b>} \mathbf{\Omega}_{\text{DM}}^{a,b} \cdot \left(\mathbf{g}_i^a \vec{\sigma}_i^a \times \mathbf{g}_j^b \vec{\sigma}_j^b\right). \tag{H.5}$$

$\mathbf{g}_i^a$ is the $\mathbf{g}$ tensor defined in the local quantization coordinates for FCC lattice site i and sublattice site a. $\mathbf{g}_i^a$ satisfies $\mathbf{J}_i^a = \frac{1}{2g_J}\mathbf{g}_\mathbf{i}^\mathbf{a}\vec{\sigma}_i^a$, where $\mathbf{J}_i^a$ and $\vec{\sigma}_i^a$ are written in the same local quantization coordinates. This gives us an effective spin-1/2 equivalent of our anisotropic exchange model that will be very useful for mean field and classical Monte Carlo simulations.

H'_{int} is not the only way to express the effective spin-1/2 Hamiltonian. In a similar manner to Appendix C.2, it is possible to create an effective spin-1/2 Hamiltonian out of any linear combination of terms in H'_{int}. One such possibility comes from Ref. [52] (Eqn. 8 in Ref. [31]):

$$\begin{aligned} H_{\text{O}} = -J_{\text{nn}} \sum_{\langle \boldsymbol{r},\boldsymbol{r}'\rangle}^{\text{nn}} \Big[& g^{\parallel} \hat{\sigma}_{\boldsymbol{r}}^z \hat{\sigma}_{\boldsymbol{r}'}^z + g^{\perp} \left(\hat{\sigma}_{\boldsymbol{r}}^x \hat{\sigma}_{\boldsymbol{r}'}^x + \hat{\sigma}_{\boldsymbol{r}}^y \hat{\sigma}_{\boldsymbol{r}'}^y\right) \\ & + g^q \left(\left(\hat{\vec{\sigma}}_{\boldsymbol{r}} \cdot \vec{n}_{\boldsymbol{r},\boldsymbol{r}'}\right)\left(\hat{\vec{\sigma}}_{\boldsymbol{r}'} \cdot \vec{n}_{\boldsymbol{r},\boldsymbol{r}'}\right) - \left(\hat{\vec{\sigma}}_{\boldsymbol{r}} \cdot \vec{n}'_{\boldsymbol{r},\boldsymbol{r}'}\right)\left(\hat{\vec{\sigma}}_{\boldsymbol{r}'} \cdot \vec{n}'_{\boldsymbol{r},\boldsymbol{r}'}\right)\right) \\ & + g^K \left(\hat{\sigma}_{\boldsymbol{r}}^z \left(\hat{\vec{\sigma}}_{\boldsymbol{r}'} \cdot \vec{n}_{\boldsymbol{r},\boldsymbol{r}'}\right) + \left(\hat{\vec{\sigma}}_{\boldsymbol{r}} \cdot \vec{n}_{\boldsymbol{r},\boldsymbol{r}'}\right)\hat{\sigma}_{\boldsymbol{r}'}^z\right)\Big]. \end{aligned} \tag{H.6}$$

In this representation x, y, and z refer to the local coordinates at each sublattice site and $\phi_{\boldsymbol{r},\boldsymbol{r}'} = 0, 2\pi/3, -2\pi/3$ [52]. The two-vectors $\hat{\vec{\sigma}}_{\boldsymbol{r}}$, $\vec{n}_{\boldsymbol{r},\boldsymbol{r}'}$, and $\vec{n}'_{\boldsymbol{r},\boldsymbol{r}'}$ are defined as [52]:

$$\hat{\vec{\sigma}}_{\boldsymbol{r}} = \left(\hat{\sigma}_{\boldsymbol{r}}^x, \hat{\sigma}_{\boldsymbol{r}}^y\right), \tag{H.7}$$

$$\vec{n}_{\boldsymbol{r},\boldsymbol{r}'} = \left(\cos\phi_{\boldsymbol{r},\boldsymbol{r}'}, -\sin\phi_{\boldsymbol{r},\boldsymbol{r}'}\right), \tag{H.8}$$

and

$$\vec{n}'_{\boldsymbol{r},\boldsymbol{r}'} = \left(\sin\phi_{\boldsymbol{r},\boldsymbol{r}'}, \cos\phi_{\boldsymbol{r},\boldsymbol{r}'}\right). \tag{H.9}$$

The various g^α terms are defined as [52]:

$$g^{\parallel} = 1 - 8\sqrt{6}x - \frac{9}{2}x^2 - 3\sqrt{6}x^3 + \frac{63}{16}x^4, \tag{H.10}$$

$$g^{\perp} = 1 + 4\sqrt{6}x + \frac{45}{2}x^2 - 3\sqrt{6}x^3 + \frac{9}{16}x^4, \tag{H.11}$$

$$g^{q} = -2\left(1 - 2\sqrt{6}x + 9x^2 - 3\sqrt{6}x^3 + \frac{9}{4}x^4\right), \tag{H.12}$$

$$g^{K} = 2\sqrt{2}\left(1 + \sqrt{6}x - \frac{45}{4}x^2 + \frac{15}{4}\sqrt{6}x^3 - \frac{9}{8}x^4\right). \tag{H.13}$$

$x = V_{pf\pi}/V_{pf\sigma}$ is the ratio of two Slater-Koster parameters, representing transfer integrals between p_x/p_y and $f_{x(5z^2-r^2)}/f_{y(5z^2-r^2)}$ orbitals and p_z and $f_{(5z^2-3r^2)z}$ orbitals respectively [52]. The relationship between the terms in $H_{\rm O}$ and H'_{int} are given by (Eqns. 13-16 in Ref. [31]):

$$-J_{\rm nn}g^{\parallel} = -\frac{g_{\parallel}^2}{12g_J^2}\left(-3\mathcal{J}_{\rm Ising} + \mathcal{J}_{\rm iso} - 5\mathcal{J}_{\rm pd} - 4\mathcal{J}_{\rm DM}\right), \tag{H.14}$$

$$-J_{\rm nn}g^{\perp} = -\frac{g_{\perp}^2}{48g_J^2}\left(\mathcal{J}_{\rm iso} - \frac{1}{2}\mathcal{J}_{\rm pd} + \frac{1}{2}\mathcal{J}_{\rm DM}\right), \tag{H.15}$$

$$-J_{\rm nn}g^{q} = \frac{g_{\perp}^2}{24g_J^2}\left(\mathcal{J}_{\rm iso} + \frac{7}{4}\mathcal{J}_{\rm pd} - \mathcal{J}_{\rm DM}\right), \tag{H.16}$$

$$-J_{\rm nn}g^{K} = -\frac{\sqrt{2}g_{\parallel}g_{\perp}}{12g_J^2}\left(\mathcal{J}_{\rm iso} - \frac{1}{2}\mathcal{J}_{\rm pd} + 2\mathcal{J}_{\rm DM}\right). \tag{H.17}$$

By inverting these equations it is possible to express the couplings $\{\mathcal{J}_e\}$ in terms of $\{\mathcal{J}_{\rm O}\} = \{-J_{\rm nn}, g^{\parallel}, g^{\perp}, g^{q}, g^{K}\}$ with one free parameter that we choose to be the overall magnitude of the interactions, $-J_{\rm nn}$. Because of this extra degree of freedom we can only compute the ratios of the terms in $\{\mathcal{J}_e\}$, $\frac{\mathcal{J}_{\rm iso}}{\mathcal{J}_{\rm Ising}}$, $\frac{\mathcal{J}_{\rm pd}}{\mathcal{J}_{\rm Ising}}$, and $\frac{\mathcal{J}_{\rm DM}}{\mathcal{J}_{\rm Ising}}$ from the model of [52] for comparison to our results in Chapter 4.2. Expressing these ratios in terms of x and plotting them yields the results shown in Fig. H.1. The ratios of $\frac{\mathcal{J}_{\rm iso}}{\mathcal{J}_{\rm Ising}}$, $\frac{\mathcal{J}_{\rm pd}}{\mathcal{J}_{\rm Ising}}$, and $\frac{\mathcal{J}_{\rm DM}}{\mathcal{J}_{\rm Ising}}$ for the two anisotropic exchange models determined in this study are shown in Table H.1. Comparing the ratios in Table H.1 to those computed using the results of Ref. [52] in Fig. H.1, we can see that for $x \approx [-\infty, -0.5]$ and $x \approx [20, \infty]$, there is fair agreement in terms of sign and magnitude between our models and that of Ref. [52]. The best agreement occurs at $x \sim -1.5$. In the range $x \approx [-0.5, 10]$, the ratios $\frac{\mathcal{J}_{\rm iso}}{\mathcal{J}_{\rm Ising}}$, $\frac{\mathcal{J}_{\rm pd}}{\mathcal{J}_{\rm Ising}}$, and $\frac{\mathcal{J}_{\rm DM}}{\mathcal{J}_{\rm Ising}}$ diverge as $\mathcal{J}_{\rm Ising} \to 0$, which happens at multiple points, as seen in Fig. H.2, making any comparison almost impossible [31].

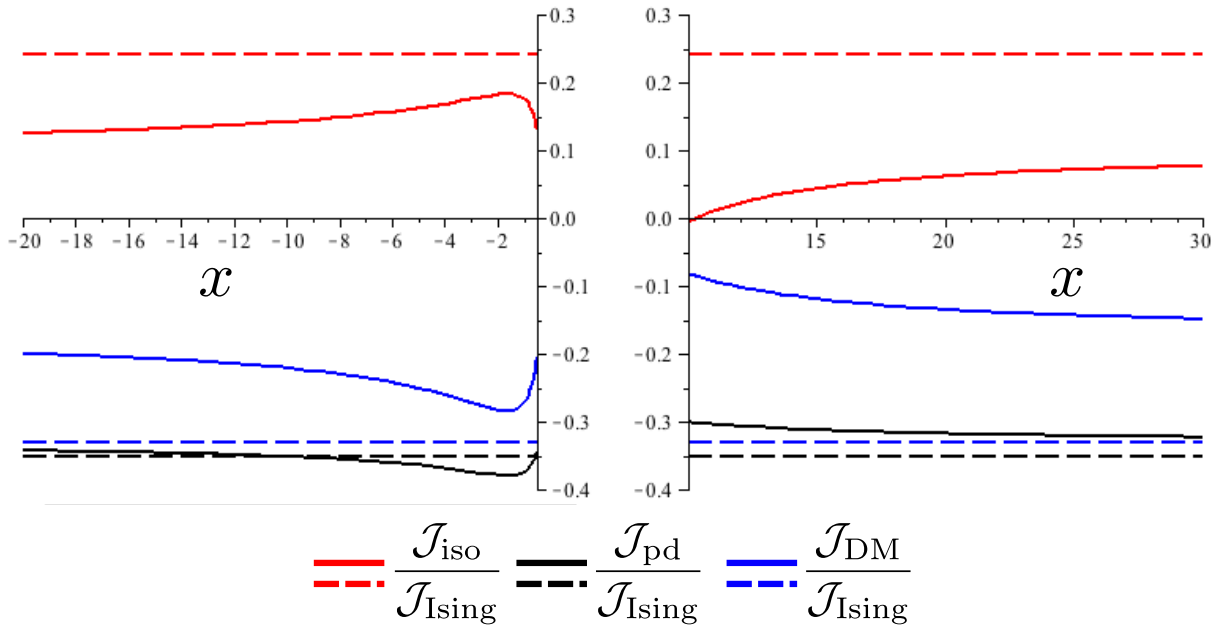

Figure H.1: Plots of the ratios $\frac{\mathcal{J}_{\rm iso}}{\mathcal{J}_{\rm Ising}}$, $\frac{\mathcal{J}_{\rm pd}}{\mathcal{J}_{\rm Ising}}$, and $\frac{\mathcal{J}_{\rm DM}}{\mathcal{J}_{\rm Ising}}$ as a function of x, the ratio of two Slater-Koster parameters, computed from the work of Ref. [52] (solid lines) and from the exchange couplings of Table 4.1 as shown in Table H.1, for the CEF parameterization of Cao *et al.* (dashed lines). The two plots span the ranges $x \approx [-20, -0.5]$ and $x \approx [10, 30]$.

Table H.1: $\frac{\mathcal{J}_{\rm iso}}{\mathcal{J}_{\rm Ising}}$, $\frac{\mathcal{J}_{\rm pd}}{\mathcal{J}_{\rm Ising}}$, and $\frac{\mathcal{J}_{\rm DM}}{\mathcal{J}_{\rm Ising}}$ computed from the exchange couplings in Table 4.1.

CEF Parameterization	$\frac{\mathcal{J}_{\rm iso}}{\mathcal{J}_{\rm Ising}}$	$\frac{\mathcal{J}_{\rm pd}}{\mathcal{J}_{\rm Ising}}$	$\frac{\mathcal{J}_{\rm DM}}{\mathcal{J}_{\rm Ising}}$
Hodges *et al.* [20]	0.279 ± 0.008	-0.36 ± 0.01	-0.33 ± 0.01
Cao *et al.* [19]	0.241 ± 0.007	-0.35 ± 0.01	-0.33 ± 0.01

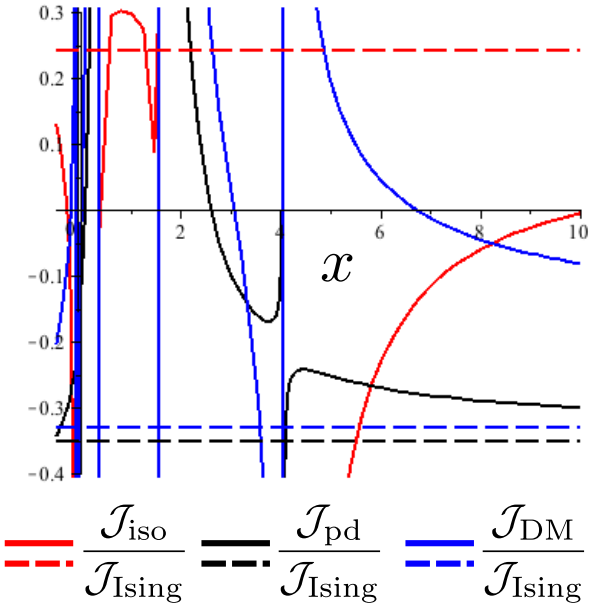

Figure H.2: Plot of the ratios $\frac{\mathcal{J}_{\rm iso}}{\mathcal{J}_{\rm Ising}}$, $\frac{\mathcal{J}_{\rm pd}}{\mathcal{J}_{\rm Ising}}$, and $\frac{\mathcal{J}_{\rm DM}}{\mathcal{J}_{\rm Ising}}$ as a function of x, the ratio of two Slater-Koster parameters, computed from the work of Ref. [52] (solid lines) and from the exchange couplings of Table 4.1 as shown in Table H.1, for the CEF parameterization of Cao *et al.* (dashed lines). The plot spans the range $x \approx [-0.5, 10]$.

In summary, if we express our nearest-neighbour bilinear exchange models for $Yb_2Ti_2O_7$ in terms of the recent work of Onoda *et al.* [52, 53], we find good agreement between our models and the work of Ref. [52]. This is particularly interesting as it perhaps provides an independent confirmation of a large DM exchange in $Yb_2Ti_2O_7$, which might otherwise be thought of as a flaw in our model.

Appendix I

Units of the Magnetic Susceptibility

This appendix provides a very brief explanation of the relationship between the units of the local susceptibility in Ref. [19], the bulk susceptibility in Ref. [34], and the RPA susceptibility of Chapter 6. Ref. [19] reports the local susceptibility in SI/MKS units of Bohr magnetons per Tesla, $\mu_{\mathrm{B}}\mathrm{T}^{-1}$. Ref. [34] reports the bulk susceptibility in CGS-EMU units of emu per mole of ytterbium, emu(mol.Yb)$^{-1}$. The RPA susceptibility is computed in natural units of inverse temperature, K^{-1}. This is equivalent to units of $\mu_{\mathrm{B}}\mathrm{K}^{-1}$ because $\mu_{\mathrm{B}} = 1$ is used in the calculations. In order to compare the results of calculations based on our anisotropic exchange model to experiment, we desire a way to convert the RPA susceptibility into the appropriate experimental units.

As explained, Ref. [19] reports the local susceptibility in SI/MKS units of $\mu_{\mathrm{B}}\mathrm{T}^{-1}$. To relate these units to those of the RPA susceptibility (K^{-1}) we define the constant $C_{\mathrm{SI/MKS}}$, such that $\chi_{\mathrm{SI/MKS}} = C_{\mathrm{SI/MKS}} \cdot \chi_{\mathrm{RPA}}$. $C_{\mathrm{SI/MKS}}$ is given by:

$$C_{\mathrm{SI/MKS}} = \frac{g_J^2 \mu_{\mathrm{B}}}{k_{\mathrm{B}}}, \tag{I.1}$$

where g_J is the Landé g factor for $Yb_2Ti_2O_7$, μ_{B} is the Bohr magneton, and k_{B} is the Boltzmann constant. In SI/MKS units $\mu_{\mathrm{B}} = 9.274 \times 10^{-24}$ JT^{-1} and $k_{\mathrm{B}} = 1.3806504 \times 10^{-23}$ JK^{-1}. g_J for $Yb_2Ti_2O_7$ is 8/7. Inserting these values into Eqn. (I.1) gives the result $C_{\mathrm{SI/MKS}} = 0.87734$ $\mu_{\mathrm{B}}\mathrm{KT}^{-1}$. Multiplying the RPA susceptibility in units of $\mu_{\mathrm{B}}\mathrm{K}^{-1}$ by $C_{\mathrm{SI/MKS}}$ gives the susceptibility in the desired units of $\mu_{\mathrm{B}}/\mathrm{T}$.

Ref. [34] reports the bulk susceptibility in CGS-EMU units of emu(mol.Yb)$^{-1}$, where emu stands for the CGS-EMU units of magnetic susceptibility. In order to compare our

calculations of the bulk susceptibility to the experimental results of Ref. [34] we define the constant $C_{\mathrm{CGS-EMU}}$, such that $\chi_{\mathrm{CGS-EMU}} = C_{\mathrm{CGS-EMU}} \cdot \chi_{\mathrm{RPA}}$. $C_{\mathrm{CGS-EMU}}$ is given by:

$$C_{\mathrm{CGS-EMU}} = \frac{g_J^2 \mu_{\mathrm{B}}^2 N_{\mathrm{A}}}{k_{\mathrm{B}}}, \tag{I.2}$$

where once again g_J is the Landé g factor, μ_{B} is the Bohr magneton, k_{B} is the Boltzmann constant, and N_{A} is Avogadro's number. $C_{\mathrm{CGS-EMU}}$ includes an extra factor of μ_{B} compared to $C_{\mathrm{SI/MKS}}$ because we are switching unit systems, so this extra μ_{B} is essentially $\mu_{\mathrm{B,EMU-CGS}}/\mu_{\mathrm{B,SI/MKS}}$ where $\mu_{\mathrm{B,SI/MKS}}$ is set to one. Because we desire the magnetic susceptibility in EMU-CGS units, we must compute $C_{\mathrm{CGS-EMU}}$ in CGS-EMU units, where $\mu_{\mathrm{B}} = 9.274 \times 10^{-21}$ ergG^{-1}, $N_{\mathrm{A}} = 6.022 \times 10^{23}$, and $k_{\mathrm{B}} = 1.38 \times 10^{-16}$ ergK^{-1}. Inserting these values into Eqn. (I.2) gives $C_2 = 0.48999$ KergG^{-2}mol.$^{-1}$. Multiplying the RPA susceptibility by this value gives the desired units μ_{B}G^{-1}mol.$^{-1}$, the CGS-EMU units of susceptibility per mole.

References

[1] S. T. Bramwell and M. J. P. Gingras. Spin ice state in frustrated magnetic pyrochlore materials. *Science (New York, N.Y.)*, 294(5546):1495–501, November 2001. 1, 6, 92

[2] T. Fennell, P. P. Deen, A. R. Wildes, K. Schmalzl, D. Prabhakaran, A. T. Boothroyd, R. J. Aldus, D. F. McMorrow, and S. T. Bramwell. Magnetic Coulomb phase in the spin ice $Ho_2Ti_2O_7$. *Science (New York, N.Y.)*, 326(5951):415–7, October 2009. 1

[3] D. J. P. Morris, D. A. Tennant, S. A. Grigera, B. Klemke, C. Castelnovo, R. Moessner, C. Czternasty, M. Meissner, K. C. Rule, J.-U. Hoffmann, K. Kiefer, S. Gerischer, D. Slobinsky, and R. S. Perry. Dirac strings and magnetic monopoles in the spin ice $Dy_2Ti_2O_7$. *Science (New York, N.Y.)*, 326(5951):411–4, October 2009. 1

[4] R. Moessner and J. T. Chalker. Properties of a Classical Spin Liquid: The Heisenberg Pyrochlore Antiferromagnet. *Physical Review Letters*, 80(13):2929–2932, March 1998. 4

[5] B. Canals and C. Lacroix. Pyrochlore Antiferromagnet: A Three-Dimensional Quantum Spin Liquid. *Physical Review Letters*, 80(13):2933–2936, March 1998. 4

[6] J. S. Gardner, G. Ehlers, N. Rosov, R. W. Erwin, and C. Petrovic. Spin-spin correlations in $Yb_2Ti_2O_7$: A polarized neutron scattering study. *Physical Review B*, 70(18):180404, November 2004. 4, 5, 6, 15, 16, 88, 92, 127

[7] S. Curnoe. Quantum spin configurations in $Tb_2Ti_2O_7$. *Physical Review B*, 75(21):212404, June 2007. 5, 104

[8] Figure generated using CrystalMaker. http://www.crystalmaker.com/. 5

[9] J. S. Gardner, S. R. Dunsiger, B. D. Gaulin, M. J. P. Gingras, J. E. Greedan, R. F. Kiefl, M. D. Lumsden, W. A. MacFarlane, N. P. Raju, J. E. Sonier, I. Swainson,

and Z. Tun. Cooperative Paramagnetism in the Geometrically Frustrated Pyrochlore Antiferromagnet $Tb_2Ti_2O_7$. *Physical Review Letters*, 82(5):1012–1015, February 1999. 6, 92

[10] Jason S. Gardner, Michel J. P. Gingras, and John E. Greedan. Magnetic pyrochlore oxides. *Reviews of Modern Physics*, 82(1):53–107, January 2010. 6

[11] M. Gingras, C. Stager, N. Raju, B. Gaulin, and J. Greedan. Static Critical Behavior of the Spin-Freezing Transition in the Geometrically Frustrated Pyrochlore Antiferromagnet $Y_2Mo_2O_7$. *Physical Review Letters*, 78(5):947–950, February 1997. 6

[12] Y. Chapuis, P. Dalmas de Réotier, C. Marin, A. Yaouanc, A. Forget, A. Amato, and C. Baines. Probing the ground state of $Gd_2Sn_2O_7$ through μSR measurements. *Physica B: Condensed Matter*, 404(5-7):686–688, April 2009. 6

[13] J. Lago, T. Lancaster, S. J. Blundell, S. T. Bramwell, F. L. Pratt, M. Shirai, and C. Baines. Magnetic ordering and dynamics in the XY pyrochlore antiferromagnet: a muon-spin relaxation study of $Er_2Ti_2O_7$ and $Er_2Sn_2O_7$. *Journal of Physics: Condensed Matter*, 17(6):979–988, February 2005. 6

[14] J. A. Hodges, P. Bonville, A. Forget, and G. André. First-order transition in frustrated $Yb_2Ti_2O_7$ without long-range order. *Canadian Journal of Physics*, 79:1373–1380, 2001. 6, 10, 11, 12, 13

[15] J. A. Hodges, P. Bonville, A. Forget, A. Yaouanc, P. Dalmas De Réotier, G. André, M. Rams, K. Królas, C. Ritter, P. C. M. Gubbens, C. T. Kaiser, P. J. C. King, and C. Baines. First-Order Transition in the Spin Dynamics of Geometrically Frustrated $Yb_2Ti_2O_7$. *Physical Review Letters*, 88(7):077204, February 2002. 6, 10, 12, 13, 14, 18, 88, 92

[16] W. J. Huiskamp, H. W. J. Blote, and R. F. Wielinga. Heat-Capacity Measurements on Rare-Earth Double Oxides $R_2M_2O_7$. *Physica*, 43:549–568, 1969. 6, 8, 9, 12, 13, 14, 19, 20, 21, 25, 47, 60, 84, 92

[17] P. Dalmas de Réotier, V. Glazkov, C. Marin, A. Yaouanc, P. C. M. Gubbens, P. Sakarya, P. Bonville, A. Amato, C. Baines, and P. J. C. King. Studies of $R_2Ti_2O_7$ (R=Gd and Yb); new results. *Physica B: Condensed*, 374-375:145, 2006. 6, 13

[18] S. T. Bramwell, M. N. Field, M. J. Harris, and I. P. Parkin. Bulk magnetization of the heavy rare earth titanate pyrochlores-a series of model frustrated magnets. *Journal of Physics:*, 12:483–495, 2000. 6, 10, 28, 47, 60, 98

[19] H. B. Cao, A. Gukasov, I. Mirebeau, P. Bonville, C. Decorse, and G. Dhalenne. Ising versus XY Anisotropy in Frustrated $R_2Ti_2O_7$ Compounds as Seen by Polarized Neutrons. *Physical Review Letters*, 103:056402, July 2009. 6, 9, 16, 17, 18, 25, 28, 47, 56, 57, 58, 59, 60, 61, 72, 75, 76, 77, 78, 79, 80, 82, 92, 94, 97, 98, 100, 101, 134, 136

[20] J. A. Hodges, P. Bonville, A. Forget, M. Rams, K. Krolas, and G. Dhalenne. The crystal field and exchange interactions in $Yb_2Ti_2O_7$. *J. Phys. Cond. Matt.*, 13:9301–9310, 2001. 6, 9, 10, 11, 12, 15, 16, 17, 18, 25, 27, 28, 47, 51, 53, 54, 55, 56, 57, 58, 59, 60, 61, 70, 77, 78, 79, 82, 92, 94, 97, 98, 99, 100, 134

[21] Figure generated using POV-Ray. http://www.povray.org/. 7, 24, 116

[22] M. G. Townsend and W. A. Crossley. Magnetic susceptibility of rare-earth compounds with the pyrochlore structure. *Journal of Physics and Chemistry of Solids*, 29(4):593–598, April 1968. 8, 9, 11, 27, 28

[23] B. D. Dunlap, G. K. Shenoy, J. M. Friedt, M. Meyer, and G. J. McCarthy. Crystal Field Properties of $Yb_2Ti_2O_7$ using ^{170}Yb Mossbauer Spectroscopy. *Phys. Rev. B.*, 18(4):1936–1942, 1978. 8, 9, 11, 27, 28

[24] B. G. Wybourne. *Spectroscopic Properties of Rare Earths.* Interscience Publishers, New York, 1965. 9, 100

[25] A. Sengupta. Crystal field studies on magnetic and nuclear properties of $Yb_2Ti_2O_7$. *Journal of Physics and Chemistry of Solids*, 60(3):331–336, March 1999. 9, 11, 28

[26] B. Malkin, A. Zakirov, M. Popova, S. Klimin, E. Chukalina, E. Antic-Fidancev, Ph. Goldner, P. Aschehoug, and G. Dhalenne. Optical spectroscopy of $Yb_2Ti_2O_7$ and $Y_2Ti_2O_7$:Yb^{3+} and crystal-field parameters in rare-earth titanate pyrochlores. *Physical Review B*, 70(7):075112, August 2004. 9, 16

[27] R. Siddharthan, B. Shastry, A. Ramirez, A. Hayashi, R. Cava, and S. Rosenkranz. Ising Pyrochlore Magnets: Low-Temperature Properties, Ice Rules, and Beyond. *Physical Review Letters*, 83(9):1854–1857, August 1999. 9, 10

[28] S. Rosenkranz, A. P. Ramirez, A. Hayashi, R. J. Cava, R. Siddharthan, and B. S. Shastry. Crystal-field interaction in the pyrochlore magnet $Ho_2Ti_2O_7$. *Journal of Applied Physics*, 87(9):5914, 2000. 10

[29] J. E. Greedan. *Oxides with trirutile and pyrochlore stucture*, chapter 6.2, pages 87–123. Springer, Berlin, 1992. 11

[30] P. Bonville, J. A. Hodges, J.-Ph. Bouchard, E. Bertin, M. Ocio, P. Dalmas de Réotier, P. Regnault, J. P. Sanchez, S. Sosin, A. Yaouanc, M. Rams, K. Krolas, and H. M. Rønnow. Transition and Spin Dynamics at very low temperature in the pyrochlore $Yb_2Ti_2O_7$ and $Gd_2Sn_2O_7$. *Zakopane School of Physics*, (1):1–20, 2003. 13, 21, 22, 23, 25

[31] J. Thompson, P. A. McClarty, H. Rønnow, L.-P. Regnault, A. Sorge, and M. J. P. Gingras. Rods of Neutron Scattering Intensity in $Yb_2Ti_2O_7$: Compelling Evidence for Significant Anisotropic Exchange in a Magnetic Pyrochlore Oxide. *Physical Review Letters*, 106(18):187202, May 2011. 14, 20, 25, 28, 29, 30, 47, 49, 55, 58, 59, 60, 62, 69, 131, 132, 133

[32] P. Bonville, J. A. Hodges, E. Bertin, J.-Ph. Bouchaud, P. Dalmas De Réotier, L.-P. Regnault, H. M. Rønnow, J.-P. Sanchez, S. Sosin, and A. Yaouanc. Transitions and Spin Dynamics at Very Low Temperature in the Pyrochlores $Yb_2Ti_2O_7$ and $Gd_2Sn_2O_7$. *Hyperfine Interactions*, 156/157(1-4):103–111, December 2004. 14

[33] Y. Yasui, M. Soda, S. Iikubo, M. Sato, N. Hamaguchi, T. Matsushita, N. Wada, T. Takeuchi, N. Aso, and K. Kakurai. Ferromagnetic Transition of Pyrochlore Compound $Yb_2Ti_2O_7$. *Journal of the Physics Society Japan*, 72(11):3014–3015, November 2003. 14, 15, 16, 17, 19, 25

[34] H. B. Cao, A. Gukasov, I. Mirebeau, and P. Bonville. Anisotropic exchange in frustrated pyrochlore $Yb_2Ti_2O_7$. *Journal of Physics: Condensed Matter*, 21(49):492202, December 2009. 16, 17, 25, 72, 79, 81, 82, 94, 136, 137

[35] A. Gukasov and P. J. Brown. Determination of atomic site susceptibility tensors from polarized neutron diffraction data. *Journal of Physics: Condensed Matter*, 14(38):8831, 2002. 16, 73, 74

[36] M. J. P. Gingras. *Spin Ice*, pages 293–329. Springer, Berlin, Heidelberg, 1st edition, 2011. 18

[37] B. Z. Malkin, T. T. A. Lummen, P. H. M. van Loosdrecht, G. Dhalenne, and A. R. Zakirov. Static magnetic susceptibility, crystal field and exchange interactions in rare earth titanate pyrochlores. *Journal of Physics: Condensed Matter*, 22(27):276003, 2010. 18, 19, 25, 72

[38] J. D. Thompson, P. A. McClarty, and M. J. P. Gingras. Local susceptibility of the $Yb_2Ti_2O_7$ rare earth pyrochlore computed from a Hamiltonian with anisotropic ex-

change. *Journal of physics. Condensed matter*, 23(16):164219, April 2011. 19, 76, 77

[39] J. A. Quilliam. *Disorder, Geometric Frustration and the Dipolar Interaction in Rare Earth Magnets*. Ph.d., University of Waterloo, 2010. 19, 20

[40] K. A. Ross, J. P. C. Ruff, C. P. Adams, J. S. Gardner, H. A. Dabkowska, Y. Qiu, J. R. D. Copley, and B. D. Gaulin. Two Dimensional Kagome Correlations and Field Induced Order in the Ferromagnetic XY Pyrochlore $Yb_2Ti_2O_7$. *Physical Review Letters*, 103:227202, February 2009. 19, 20, 21, 22, 23, 24, 25, 64, 70, 94

[41] J. Jensen and A. R. Mackintosh. *Rare Earth Magnetism*. Clarendon Press, Oxford, 1991. 21, 33, 34, 35, 36, 37, 38, 39, 40, 41, 45, 46, 47

[42] Y.-J. Kao, M. Enjalran, A. Del Maestro, H. Molavian, and M. J. P. Gingras. Understanding paramagnetic spin correlations in the spin-liquid pyrochlore $Tb_2Ti_2O_7$. *Physical Review B*, 68(17):172407, November 2003. 29, 44

[43] S. W. Lovesey. *Theory of Neutron Scattering from Condensed Matter*. Clarendon Press, Oxford, 1984. 42, 43

[44] V. M. Nield and D. A. Keen. *Diffuse Neutron Scattering from Crystalline Materials*. Clarendon Press, Oxford, 2001. 43

[45] D. Hohlwein and R. Schneider. Magnetic interaction parameters from paramagnetic diffuse neutron scattering in MnO. *Physical Review B*, 68(14):140408, 2003. 44

[46] Z. Wang and C. Holm. Estimate of the cutoff errors in the Ewald summation for dipolar systems. *The Journal of Chemical Physics*, 115(14):6351, 2001. 45, 121

[47] M. P. Allen and D. J. Tildesley. *Computer Simulation of Liquids*, volume 18 of *Oxford science publications*. Oxford University Press, 1989. 45, 121

[48] W. H. Press, S. A. Teukolsky, W. T. Vetterling, and B. P. Flannery. *Numerical Recipes: The Art of Scientific Computing*. Cambridge University Press, Cambridge, 3rd edition, 2007. 50, 51, 53

[49] N. Metropolis, A. W. Rosenbluth, M. N. Rosenbluth, A. H. Teller, and E. Teller. Equation of State Calculations by Fast Computing Machines. *The Journal of Chemical Physics*, 21(6):1087, December 1953. 50

[50] T. Yavorskii, T. Fennell, M. J. P. Gingras, and S. T. Bramwell. $Dy_2Ti_2O_7$ Spin Ice: A Test Case for Emergent Clusters in a Frustrated Magnet. *Physical Review Letters*, 101(3):037204, July 2008. 51

[51] M. Elhajal, B. Canals, R. Sunyer, and C. Lacroix. Ordering in the pyrochlore antiferromagnet due to Dzyaloshinsky-Moriya interactions. *Physical Review B*, 71(9):094420, March 2005. 56, 115

[52] S. Onoda. Effective quantum pseudospin-1/2 model for Yb pyrochlore oxides. *arXiv:1101.1230*, January 2011. 56, 93, 98, 131, 132, 133, 134, 135

[53] S. Onoda and Y. Tanaka. Quantum fluctuations in the effective pseudospin-1/2 model for magnetic pyrochlore oxides. *Physical Review B*, 83(9):094411, March 2011. 56, 135

[54] M. Enjalran and M. J. P. Gingras. Theory of paramagnetic scattering in highly frustrated magnets with long-range dipole-dipole interactions: The case of the $Tb_2Ti_2O_7$ pyrochlore antiferromagnet. *Physical Review B*, 70(17):174426, November 2004. 62, 89, 121, 122, 123, 124, 125

[55] J. Reimers, A. Berlinsky, and A.-C. Shi. Mean-field approach to magnetic ordering in highly frustrated pyrochlores. *Physical Review B*, 43(1):865–878, January 1991. 62, 89

[56] P. Stasiak. *Theoretical studies of frustrated magnets with dipolar interactions*. PhD thesis, University of Waterloo, 2009. 83

[57] O. Cépas, A. Young, and B. Shastry. Degeneracy and strong fluctuation-induced first-order phase transition in the dipolar pyrochlore antiferromagnet. *Physical Review B*, 72(18), November 2005. 84

[58] A. Poole, A. S. Wills, and E. Lelièvre-Berna. Magnetic ordering in the XY pyrochlore antiferromagnet $Er_2Ti_2O_7$: a spherical neutron polarimetry study. *Journal of Physics: Condensed Matter*, 19(45):452201, November 2007. 86

[59] J. T. Chalker. *Geometrically Frustrated Antiferromagnets: Statistical Mechanics and Dynamics*, pages 3–21. Springer, Berlin, Heidelberg, 1st edition, 2011. 86

[60] A. G. Del Maestro. *Quantum Spin Fluctuations in the Heisenberg-Like Pyrochlore Antiferromagnet Gadolinium Titanate*. M.Sc., University of Waterloo, 2003. 88, 121, 122, 124

[61] A. Sorge. An Effective Spin Approach to Paramagnetic Scattering in Frustrated Magnets. Technical report, University of Canterbury, Christchurch, New Zealand, 2008. 89, 97

[62] H. Xiang, E. Kan, M.-H. Whangbo, C. Lee, S.-H. Wei, and X. Gong. Single-ion anisotropy, Dzyaloshinskii-Moriya interaction, and negative magnetoresistance of the spin-1/2 pyrochlore $R_2V_2O_7$. *Physical Review B*, 83(17):174402, May 2011. 90

[63] P. A. McClarty. Thanks to Dr. P. A. Mcclarty for performing these calculations., 2010. 97

[64] A. Abragam and B. Bleaney. *Electron Paramagnetic Resonance of Transition Ions*. Clarendon Press, Oxford, 1970. 100, 102, 103

[65] A. S. Nowick. *Crystal Properties via Group Theory*. Cambridge University Press, Cambridge, 1995. 104, 105, 106, 107, 108

[66] P. A. McClarty, S. H. Curnoe, and M. J. P. Gingras. Energetic selection of ordered states in a model of the $Er_2Ti_2O_7$ frustrated pyrochlore XY antiferromagnet. *Journal of Physics: Conference Series*, 145:012032, January 2009. 109, 111, 112

[67] P. A. McClarty. Discussion with Dr. P. A. Mcclarty regarding conversion between various representation of the symmetry allowed nearest neighbour interactions on the pyrochlore lattice., 2010. 112

[68] T. Moriya. Anisotropic superexchange interaction and weak ferromagnetism. *Physical Review*, 120(1):91–98, October 1960. 115

[69] G. B. Arfken and H. J. Weber. *Mathematical Methods for Physicists*. Elsevier Academic Press, New York, 6 edition, 2005. 122

[70] M. Born and K. Huang. *Dynamical Theory of Crystal Lattices*. Oxford University Press, Toronto, 4th edition, 1966. 124

[71] A. Wong. Thanks to Anson Wong for useful discussions on the treatment of the $\mathbf{q} = 0$, $\mathbf{G} = 0$ term of the Ewald summation., 2010. 125

[72] P. J. Brown. *International Tables for Crystallography: Volume C*. Kluwer Academic Publishers, Dordrecht, 3rd edition, 2006. 127, 128